Author:
Cascarini, Fred J J

Title:
Experimental and Computational Investigation of Molecular Photodissociation and Scattering Dynamics

Experimental and Computational Investigation of Molecular Photodissociation and Scattering Dynamics

Frederick Cascarini

A dissertation submitted to the University of Bristol in accordance with the requirements for award of the degree of Doctor of Philosophy in the School of Chemistry, Faculty of Science

October 2020

34,623 Words

Abstract

This thesis reports new research performed during the development and characterisation of an improved scattering chamber in an existing velocity map imaging (VMI) apparatus. These studies consist of an investigation into the photodissociation of 2,4-dibromofluorobenzene (DBFB), inelastic scattering of NO with methane, and progress towards reactive scattering. Quasi-classical trajectory (QCT) studies have also been performed on the reaction of chlorine atoms with propene.

The QCT studies of the reaction of chlorine atoms with propene investigated the effect of collision energy variation. The characteristics of the reaction were determined at collision energies of 7, 14 and 28 kJ mol^{-1}, in terms of the product HCl rotational and vibrational population distributions, opacity functions, differential cross sections, and the trajectory durations. The pathways taken by the trajectories across the reactive potential energy surface were analysed at each collision energy, identifying the relative importance of different mechanisms.

Studies of DBFB characterised the production of bromine atoms through photodissociation in the region 260 – 285 nm. This work utilised Resonance Enhanced Multi-Photon Ionisation (REMPI) of the bromine product, followed by either photofragment excitation spectroscopy or VMI. Assignment of the dissociative pathways was assisted by quantum chemical computations and by comparison with simpler bromofluorobenzenes.

The inelastic scattering of NO with methane was studied at a mean collision energy of 700 cm^{-1}. State-selective differential cross sections of scattered NO were determined using REMPI followed by VMI detection. The mechanistic implications of these cross sections are discussed, with reference to rotational rainbow theory and the observation of anticorrelated rotational energy levels for the scattered collision partners.

Finally, progress towards reactive scattering using the improved apparatus is reported. This includes the reliable production of cyanogen radicals, in preparation for an anticipated study on the reactive scattering of cyanogen radicals with methane.

To Ms Purba, who started me on this path

&

To anyone who continues this work

Acknowledgements

First and foremost, I want to thank my supervisor, Professor Andrew Orr-Ewing. I count myself extremely lucky to have a supervisor who is not only a world expert in the field, but also so unwaveringly supportive, patient, and understanding. I have grown so much under Andrew's mentorship, and I am very grateful that the mentorship was unchanged when it was clear I was not staying in academia.

Secondly, I want to thank all the PhD students and Postdocs of the Bristol Laser Group as a whole. It has been a lovely culture to be a part of, one where everyone looked out for, and was willing to offer advice to, everyone else. A culture certainly demonstrated by the Friday trips to the White Bear!

Whilst everyone in the group deserves thanks, I would like to give special mention to Dr Balázs Hornung, Dr Mitch Quinn, and Dr Patrick Robertson. Not only have I been lucky to have a wonderfully supportive supervisor, but also wonderfully supportive postdocs to work with. And three in a row at that. All have not only been good colleagues, but good friends too, and they have helped me through so much in my time at Bristol.

I have also benefited enormously from the assistance of Dr James Smith, whose technical knowledge has solved countless problems, and the workshop staff, for making mounts, guides, and tools which have either enabled the work, or made it so much easier.

I would also like to thank EPSRC for both the DTP funds to support me during this research, and for the group grant that has funded the experimental work.

I would like to then thank my friends outside of the group too. There are too many to mention here, but special mention goes to Robert Arbon. An exceptional friend, and it has also been particularly useful to have a friend going through the same experience!

Last, but by no means least, I want to thank my family. Their support and encouragement has naturally played no small part in getting me here. My Dad deserves particular mention, for looking after me (and putting up with me) whilst I wrote this thesis.

Author’s Declaration

I declare that the work in this dissertation was carried out in accordance with the requirements of the University's Regulations and Code of Practice for Research Degree Programmes and that it has not been submitted for any other academic award. Except where indicated by specific reference in the text, the work is the candidate's own work. Work done in collaboration with, or with the assistance of, others, is indicated as such. Any views expressed in the dissertation are those of the author.

SIGNED: Frederick Joseph Jasper Cascarini

DATE: 17/08/20

Table of Contents

List of Figures

List of Tables

1. Introduction

This thesis reports the development of a crossed molecular beam scattering apparatus, and its sequential use in studies of unimolecular photodissociation (Chapter 4), inelastic scattering (Chapter 5), and finally progress towards reactive scattering (Chapter 6). Alongside this experimental work, computational investigations have been performed into the reaction of chlorine atoms with propene, and these investigations are discussed in Chapter 3.

The reported work involves aspects of almost every field of gas-phase molecular dynamics, with the sole exception of elastic scattering. The field of molecular dynamics, in studying processes involving the physical movement of atoms and molecules, underpins the majority of chemistry. In this introduction I will discuss the principles and theory underlying this field, to support the discussions and conclusions presented in the remainder of this work.

1.1. Molecular Dynamics Processes

The field of molecular dynamics covers four key processes. These processes are unimolecular photodissociation, and the three forms of scattering: elastic scattering, inelastic scattering, and reactive scattering. The scattering processes are distinguished by the degree of change that occurs between the initial and final states of the scattering molecules or atoms.

During an elastic collision only the kinetic energies and linear momenta of the two colliding species change during the interaction. A typical example is the collision between two ground state noble gas atoms, from which information can be derived about the interatomic potential.[1-4] Elastic collisions are the simplest bimolecular interactions, and only conservation of total kinetic energy, and linear and angular momentum need to be considered. Inelastic scattering increases the complexity by involving changes in the internal energy of one or both species over the course of the interaction. An example of an extensively studied inelastic collision is the scattering of nitric oxide with argon,[5-9] which has now been expanded into the scattering of NO with methane,[10] as discussed in Chapter 5. Reactive scattering involves a chemical change of the species during the interaction. An example of a reactive collision system, which has been well-studied in molecular dynamics terms, is the interaction of Methane with either Fluorine[11, 12] or Chlorine[13, 14] atoms to form the methyl radical and either HF or HCl.

While the significance of reactive collisions is clear, as they underpin numerous fields including synthetic, atmospheric, combustion, plasma and astrochemistry, inelastic collisions also have a significant impact on wider chemical processes. This significance is due to the importance of internal energy states on the progress of a reaction, as illustrated by the Polanyi rules, which relate the location of the barrier to reaction with the impact of vibrational excitation on the reaction.[15, 16] Inelastic collisions also bring energetic processes to thermal equilibrium, are responsible for chemical activation to reach transition states for reactions, and are utilised in supersonic expansions (discussed in Section 1.5.1) to reduce the rotational or vibrational energy levels of a species of interest.[17] This relaxation results in a higher proportion of ground state molecules, allowing collision-induced changes of the internal energy of the species to be more accurately determined (as is demonstrated in Chapter 5).

1.2. Characterising Collisions

The physical properties of an individual collision are characterised by the impact parameter and scattering angle, along with parameters defining the velocity and relative orientation of the two species. Opacity functions and differential cross sections define the variation in the probability of an inelastic or reactive process as a function of these physical properties. These properties can either be defined relative to the arbitrary geometry in which an experiment is performed (the "laboratory", or Lab, frame of reference) or by a frame of reference defined by the species themselves (the "Centre of Mass", or CoM, frame of reference). This section introduces the properties in the context of the Laboratory frame, and the subsequent section 1.2.1 discusses the conversion to the CoM frame.

The impact parameter, b, can be defined as the distance of closest approach in the absence of an interaction between the two species.[18] In the case of two spheres, the impact parameter is simply the distance between the spheres' centres, as shown in Figure 1. In the absence of attractive potentials between the two species (the "hard sphere model") the maximum impact parameter that could result in an inelastic or reactive process (b_{max}) is the sum of the spheres' radii, again as per Figure 1.

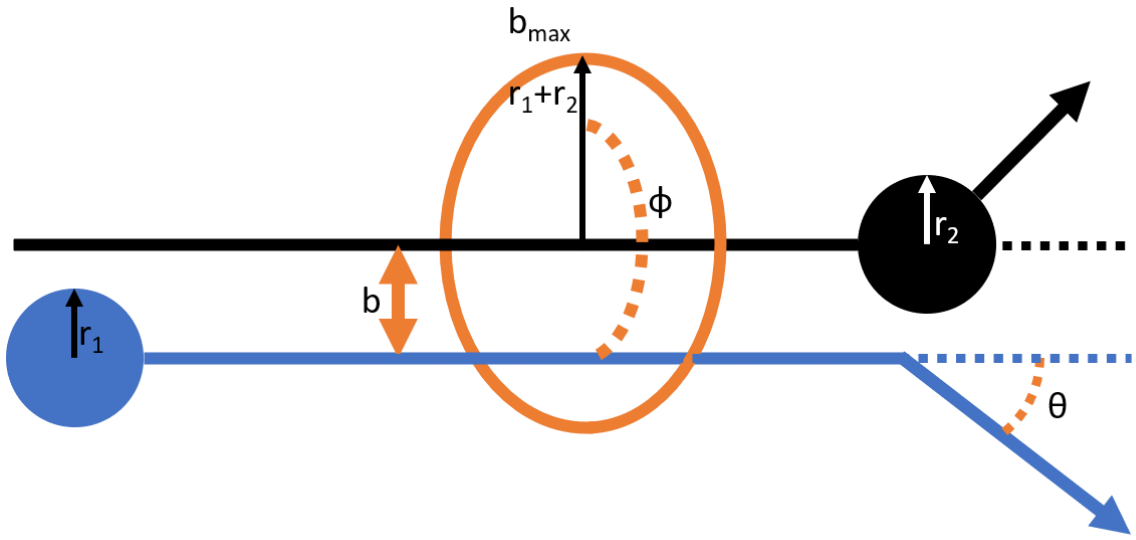

Figure 1: A diagram showing the impact parameter (b) and scattering angle (θ) for a collision in the hard sphere model, along with the maximum impact parameter (b_{max}) in terms of the two spheres' radii.

The probability of an inelastic or reactive process happening as a function of impact parameter is the Opacity Function (P(b)). This function can be integrated to obtain the collisional cross section σ by:

$$\sigma = \int_0^{2\pi} \int_0^{b_{max}} P(b) b \, \mathrm{d}b \, \mathrm{d}\phi$$

Equation 1

Where ϕ is the azimuthal angle, describing the relative orientation of the two species' trajectories, again shown in Figure 1. In the hard sphere model P(b) is not dependent on ϕ, allowing ϕ to be integrated out, and has the value 1 for $|b| \leq b_{max}$ and 0 otherwise. Therefore $\sigma_{hard\ sphere} = \pi b_{max}^2$, the area of a circle with radius b_{max}.

The scattering angle (θ) is defined as the difference in a species' velocity vector (or relative velocity, in the CoM frame) before and after the interaction, again depicted in Figure 1. The probability of a collision resulting in scattering into a solid angle of size $\mathrm{d}\omega = \sin\theta \, \mathrm{d}\theta \, \mathrm{d}\phi$ is described by:

$$P(\theta, \phi) = \frac{1}{\sigma} \frac{\mathrm{d}\sigma}{\mathrm{d}\omega}$$

Equation 2

Here $\frac{d\sigma}{d\omega}$ is the differential cross section (DCS), a measure of the area dσ that results in scattering into a specific solid angle dω.

It is often possible to infer details about an interaction from the shape of the DCS. For example, DCS functions that peak at small scattering angles are typical of reactions that proceed via large impact parameter, glancing collisions. Meanwhile functions with a peak nearer 180° are typically those that require a more head-on, low impact parameter approach to proceed. Isotropic DCS functions are characteristic of long-lived processes, where the species remain paired for an extended period leading to the final velocities being uncorrelated to the initial velocities.

1.2.1. The Centre of Mass frame

It is common to describe the parameters introduced in section 1.2 in terms of the CoM frame of reference. This frame has the advantages of generalising the details of the collision, so that the values are not specific to a certain experimental set up, and it removes a conserved value (the velocity of the centre of mass) from consideration.

The CoM frame considers all positions and vectors relative to the centre of mass of the system. An example is depicted in Figure 2, which shows how a perpendicular collision in the Lab frame can be considered a head-on collision in the CoM frame.

The velocities in the centre of mass frame (**u**) are the result of subtracting the velocity of the centre of mass in the lab frame ($\mathbf{v}_{com}$) from the velocities of the various species in the lab frame (**v**). The value of v_{com} is calculated from the momentum of the centre of mass (using the total mass of the particles, $M = m_1 + m_2$) being equivalent to the sum of the momenta of the particles in the lab frame, i.e., the CoM frame is defined by the following three equations:

$$\boldsymbol{u}_1 = \boldsymbol{v}_1 - \boldsymbol{v}_{com}$$
$$\boldsymbol{u}_2 = \boldsymbol{v}_2 - \boldsymbol{v}_{com}$$
$$\boldsymbol{v}_{com} = \frac{m_1\boldsymbol{v}_1 + m_2\boldsymbol{v}_2}{M}$$

Equation 3

The kinetic energy associated with the centre of mass, $E_{com} = \frac{1}{2}M\boldsymbol{v}_{com}^2$, is conserved in a collision and therefore unable to influence the processes (reactive or inelastic) involved in the

collision. Subtracting this kinetic energy from the total kinetic energy of the system results in the kinetic energy that can be modified by the collision, termed the collision energy:

$$E_{coll} = \frac{1}{2}\mu v_{rel}^2$$
$$\mu = \frac{m_1 m_2}{m_1 + m_2}$$
$$v_{rel} = \boldsymbol{v}_2 - \boldsymbol{v}_1$$

Equation 4

With μ being the reduced mass of the system.

An important result of the conservation of E_{com} is that the relative orientation of the two beams in the lab frame leads to modifications of the collision energy. In particular, the collision energy of a perpendicular set up of two molecular beams in the lab frame (such as that shown in Figure 2) has a higher collision energy than a parallel set up (such as that shown

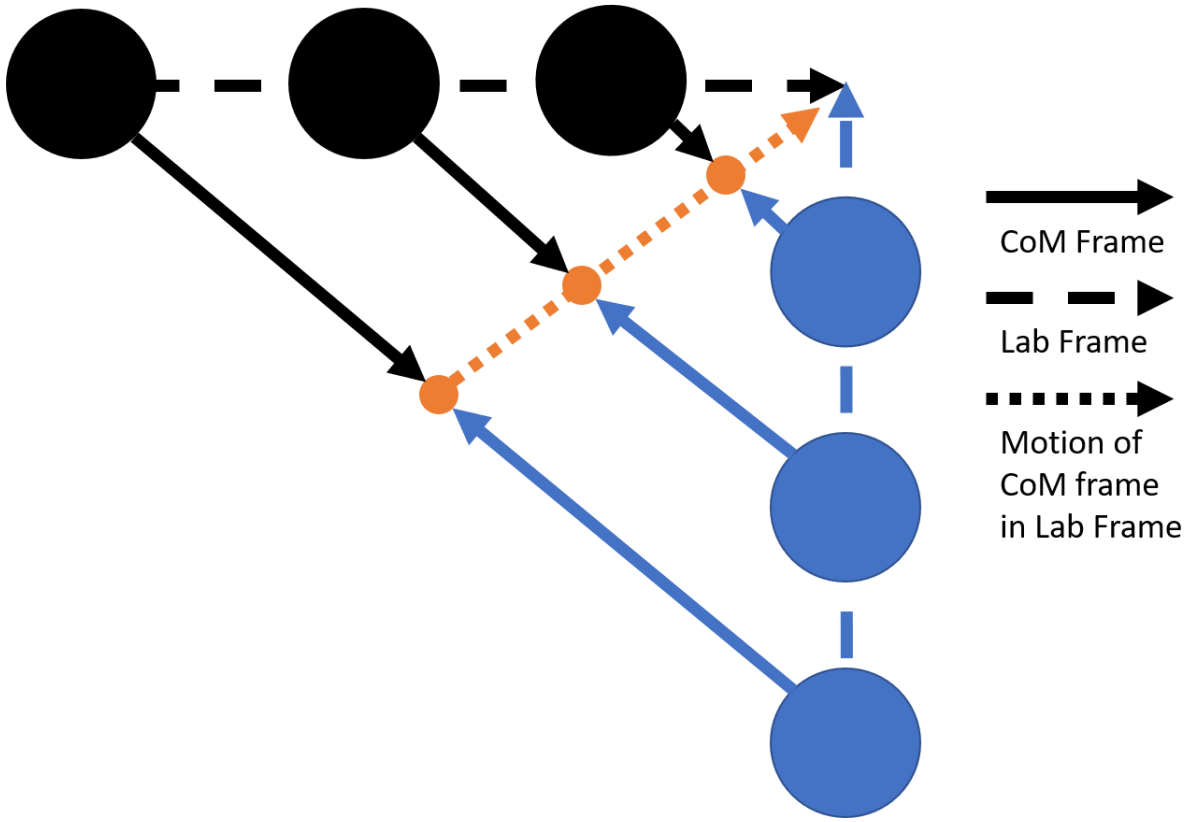

Figure 2: The relationship between the Laboratory (Lab) frame and the Centre of Mass (CoM) frame. A perpendicular collision in the lab frame is shown, with the velocities in this frame shown by dashed arrows. The CoM of each step is shown by an orange dot, which moves along the dotted arrow. The solid arrows show the velocity of each species relative to the CoM at each step.

in Figure 1). The largest collision energy is produced by an antiparallel set up, where the lab frame velocities of the two species oppose each other, and v_{rel} has a magnitude equal to the sum of the two species' speeds. The adaptation of the lab frame collision angle in this manner allows collisions to be investigated at different collision energies, without requiring a change in the total velocity of the species.[19-22]

1.2.2. Rainbow Scattering

The collision between two hard spheres can only produce one scattering angle for each impact parameter, ranging from 0° beyond b_{max}, to 180° at an impact parameter of zero. However the inclusion of attractive forces allows multiple impact parameters to produce the same scattering angle. This effect is demonstrated in Figure 3. At large impact parameters no deflection occurs (inset 1), with a gradual attractive deflection as the impact parameter reduces. This attractive deflection reaches a maximum at the "rainbow angle" θ_r (inset 2), beyond which the repulsive forces lead to the scattering angle reducing. As the impact parameter decreases further, the scattering angle passes through 0° again in a process known as "glory scattering" (inset 3) when the attractive and repulsive forces cancel out. Impact parameters less than the glory scattering value produces scattering dominated by repulsive forces (inset 4). The overall change in scattering angle by impact parameter is shown by the blue plot on the graph in Figure 3. Due to cylindrical symmetry in experimental conditions, only $|\theta|$can be determined (i.e. in the insets of Figure 3 it could not be determined if the blue species is coming from above or below the orange species, with each case inverting the deflection angles observed). The result is that the negative part of the scattering angle instead is observed as if it followed the red plot. From this plot it can be easily observed that all scattering angles $|\theta| < \theta_r$ are produced by three impact parameters, and are therefore observed with enhanced intensity in the collision's differential cross section. Since the θ_r of this system is based on the maximum angle that can be produced by the attractive potential between the two species, it can be predicted based on the strength of the attractive and repulsive fields and the collision energy of the system.[10, 22-24]

If one or both species are not spherical the scattering angle is again not unique to each impact parameter. In this case, the distribution results from geometric features of the collision between the two species. As such, the rainbow angle depends instead on the shape of the

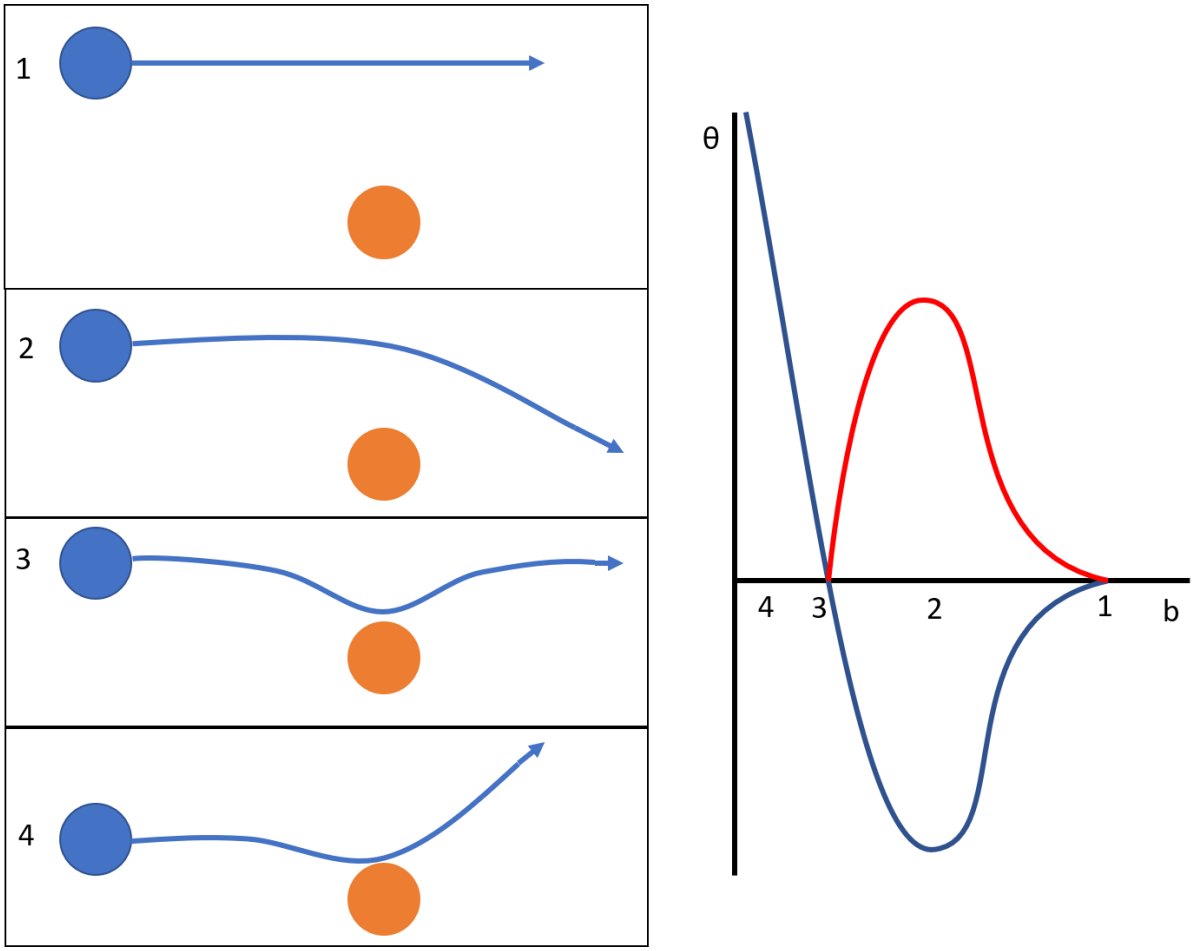

Figure 3: Variation in scattering angle (θ) by impact parameter (b) for the collision of two spheres where attractive potentials are considered. The scattering angle for a particular collision varies with impact parameter as per the blue line on the plot on the right, however the cylindrical symmetry of the process means only $|\theta|$can be determined, with the impact of this restriction shown by the red line between points 1 and 3. Insets 1 through 4 depict exemplar schematics for four key points, as discussed in the main text.

species, and varies with changes in rotational energy of the scattered species. The significance of change in rotational energy comes from the fact that only a subset of collision geometries results in sufficient torque to produce a particular rotational excitation, so the rainbow angle needs to be calculated based on this subset. An example of this form of rainbow scattering is that of a sphere and an ellipse, which is well-characterised by the work of Bosanac and Buck[25] and can be used to describe collisions such as that of rare gases with NO.[26] This system can be defined in terms of the vectors and angles shown in Figure 4, and considered as a point mass, following the trajectory shown in orange, colliding with an ellipse. In this system

momentum of the point mass along the tangent to the ellipse surface is conserved, so rotational excitation of the ellipse is based on the impulse created by the component of the point mass momentum along the normal $\hat{n}$. This momentum is equivalent to $p \cos \theta_i$, where p is the overall momentum of the particle. The resultant change in (classical) rotational angular momentum Δj is:

$$\frac{\Delta j}{p} = \frac{2b_n \cos \theta_i}{1 + \frac{\mu}{I} b_n^2}$$

Equation 5

Where I is the moment of inertia of the ellipse. Refactoring in terms of the scattering angle gives:

$$\sin \frac{\theta}{2} \approx \frac{\Delta j / p}{2b_n}$$

Equation 6

With the approximation being valid for small values of $\frac{\Delta j}{p}$. b_n has maximal values at:[25]

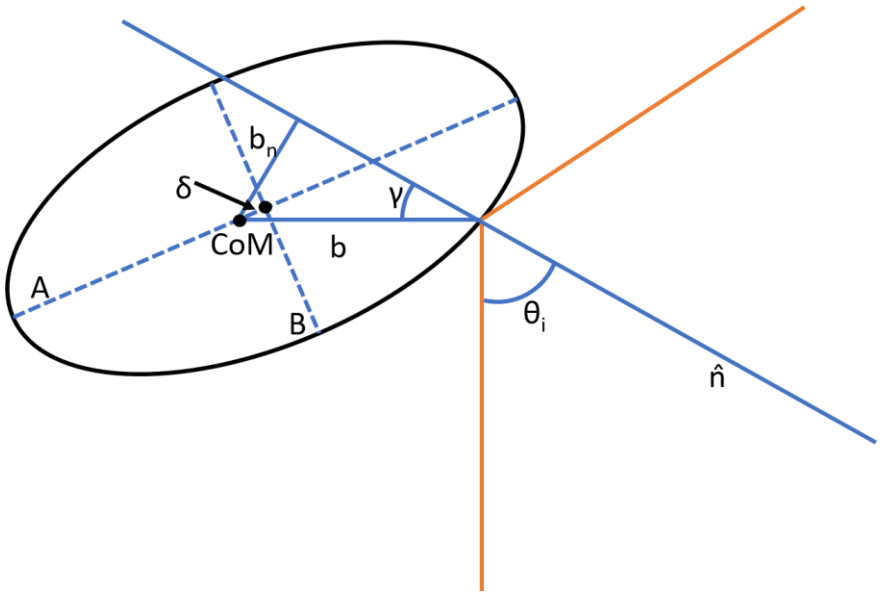

Figure 4: Schematic diagram of the collision of a spherical object (orange trajectory) with an ellipse with major and minor semiaxes A and B and a centre of mass displaced from the ellipse centre by a distance δ along axis A (representing a homonuclear diatomic if δ = 0 and a heteronuclear diatomic otherwise). $\hat{n}$ is the normal to the ellipse at the point of collision, with an impact angle θ_i. The impact parameter is b, with the normal taking an impact parameter b_n at angle γ relative to b.

$$b_{n,max} = (A - B) \pm \delta \sqrt{\frac{A}{A + B}}$$

Equation 7

These equations produce two classical rainbow angles for scattering of a heteronuclear diatomic molecule, from substituting the two values of Equation 7 into Equation 6, or one for a homonuclear diatomic ($\delta = 0$).

These predicted rainbow angles, from either method, can be used to calculate the properties of the system (such as the strength of an attractive interaction or the value of $A - B$) from experimental DCSs. Alternatively, computed values of these properties can be checked via predicting rainbow angles and comparing the predictions with the experimental results. Analysis of rainbow angles is used in Chapter 5, to discuss the applicability of attractive and hard ellipse rotational rainbows to the inelastic scattering of NO with methane.

1.3. Potential Energy Surfaces

In quantum mechanics, any system is described a wavefunction, Ψ. The action of an operator on the wavefunction produces an eigenvalue related to an observable. For example the time independent Schrödinger equation (TISE), Equation 8, uses the Hamiltonian operator ($\widehat{H}$) to determine the energy (E) of a system at a static point in time.

$$\widehat{H}\Psi = E\Psi$$

Equation 8

In the context of molecular dynamics, the wavefunction can be parametrised based on the nuclear coordinates, **R**, and the electronic coordinates, **r**. Under most conditions the electronic coordinates respond to a change in the nuclear co-ordinates at a rate far faster than the movement of the nuclei, leading to the two being separable (the Born-Oppenheimer approximation). As a result, the overall wavefunction can be expressed as a product of a nuclear-only wavefunction ($\chi_n(\boldsymbol{R})$) and an electronic wavefunction that depends on both the electronic coordinates, and parameterised by the current nuclear coordinates ($\psi_e(\boldsymbol{r}, \boldsymbol{R})$), i.e.

$$\Psi(\boldsymbol{r}, \boldsymbol{R}) = \chi_n(\boldsymbol{R})\psi_e(\boldsymbol{r}, \boldsymbol{R})$$

Equation 9

For each nuclear configuration of a system, the electronic energy levels can be determined by application of the TISE to the electronic wavefunction. A Potential Energy Surface (PES) is then

the potential energy of a specific electronic energy level, mapped as a function of nuclear coordinates. A PES that has been created utilising the Born-Oppenheimer approximation is described as an adiabatic PES. The term adiabatic contrasts with diabatic PESs, which typically describe surfaces with consistent electronic configurations rather than electronic energy level, and non-adiabatic processes which describe transitions between adiabatic levels (see Section 1.4.1).

1.3.1. Computational Calculations of Electronic Energies

The Schrödinger equation cannot be solved exactly for any species more complex than the hydrogen atom (or one-electron atomic ions). As such, approximate methods are required to calculate potential energy surfaces for systems. These methods typically start with a simple interpretation of the system, and then add complexity. This complexity can be in the form of either perturbations to the Hamiltonian, or direct improvements of the model Hamiltonian used. Two common methods that illustrate these methods are the Hartree-Fock (HF) method, along with those based on HF such as the second order Møller-Plesset method (MP2), and Density Functional Theory (DFT).[27]

HF theory assumes that each electron can be modelled individually, in an averaged electric field of the other electrons. This assumption simplifies the calculation of energies, however it removes any Coulombic correlation between pairs of electrons, which limits the precision. Furthermore, only one orbital occupancy regime (described by a Slater determinant) is considered. The inability to consider mixing between orbitals and mixed occupancy means the HF method fails when multiple orbitals become close in energy, such as in bond breaking, and renders it incapable of determining excited states.[28]

Due to these shortcomings, alternative methods are typically used. Many of these alternatives are based on Hartree-Fock theory but with further modifications. The simplest of these modifications, used in techniques such as MP2, simply considers electron correlation effects as a perturbation on top of the results produced by HF. This addition increases the accuracy of the calculation, with only a small increase in computational cost.[29, 30] Other methods expand HF to include more Slater determinants, such as in Coupled Cluster theory[31] or Complete Active Space[32] methods.

The most common alternative method to HF-based approaches is DFT. Instead of solving for a set of individual electrons, DFT models the electronic parts of the wavefunction as regions of varying electron density.[33, 34] This model has the benefit of low computational cost, however some properties of these density functions are not known exactly. To model these properties, either further approximations are needed, or semi-empirical methods are used where these properties are approximated based on experimentally determined values. Hybrid functionals, such as the widespread "B3LYP" functional,[35] merge some aspects of HF theory (specifically that relating to the exchange energy of the electrons) into DFT to increase the accuracy. Perturbation of DFT-based density calculations with a time-dependent excitation process (time dependent DFT, or TD-DFT) can also allow energies and other properties of excited states to be calculated.[36, 37]

All the methods in this section require a set of orbitals to operate on, which is known as the "basis set". Electronic orbitals have a radial decay based on an e^{-r} functional form, which can be well-approximated by Slater Type Orbitals (STOs) which have such a radial term.[38] However practical mathematical and computational considerations make Gaussian Type Orbitals (GTOs), with an e^{-r^2} dependence, preferable.[39] Due to this preference, STOs are typically approximated through a fixed linear combination of GTOs - termed a contracted GTO or CGTO. Basis sets are then made up of multiple CGTOs, with larger numbers of CGTOs both increasing the accuracy of a model whilst increasing computational cost.

1.3.2. Computational Potential Energy Surfaces

Despite the approximations that routinely occur in the computational calculation of energy levels, as detailed in the previous section, it remains prohibitively expensive to calculate an entire PES for reactions of polyatomic molecules from computed, *ab initio* values because the dimensionality of the PES scales as 3N-6 where N is the number of atoms involved. Typically, if the dynamics of a system are to be calculated at an *ab initio* level the potential energy will be determined 'on the fly'. This method only calculates *ab initio* potentials for a specific geometry if that geometry occurs in a simulation.[40] More commonly, a potential energy surface is created through the calculation of a set of *ab initio* points that span any region of interest, followed by either fitting continuous functions to these points[41-44] or interpolation between the points.[45-47]

The interpolation method attempts to deduce the energy of any arbitrary point on the PES by considering the values of the existing *ab initio* points defining the surface and weighting them according to their distance from the arbitrary point. For example, the modified Shepherd method considers the potential energy surface in the neighbourhood of a computed point to be a Taylor series in reciprocal distance from the computed point. This Taylor series is parameterised by the energy at that point, along with the first and second derivatives of the energy with respect to the nuclear coordinates.[48] Neural networks have also been designed to deduce interpolated PESs.[49]

The function fitting method is a semi-empirical method, which utilises chemical knowledge to choose a set of functions that are expected to represent the PES well along various coordinates describing molecular motions, and fit the PES to this set of functions. For example, movement along a bond extension coordinate may be fitted to a Morse potential that has been parameterised to fit all the computed points along this coordinate while fixing all other degrees of freedom.

Incorporating semi-empirical methods can also reduce the regions of the PES for which ab initio energy points need to be calculated. For example, the Empirical Valence Bond (EVB) method (used in Chapter 3 of this thesis) starts by using chemical knowledge to identify a series of chemically significant forms the system can be in. In the original work these forms were covalent and ionic resonances in the interaction of an ion with an enzyme,[50] however these forms can be generalised to include, for example, a series of intermediates in a complex reaction,[51] or a variety of products that can result from an abstraction process.[52] Each of these forms has a Hamiltonian of the PES produced by the function fitting method. Further functions are then designed, either through further fitting processes or simply through chemical knowledge, to describe the coupling between these forms. These functions are then compiled into a matrix by:

$$\widehat{H}_{EVB} = \begin{bmatrix} H_{11} & V_{12} & V_{13} \\ V_{21} & H_{22} + E_{22} & V_{23} \\ V_{31} & V_{32} & H_{33} + E_{33} \end{bmatrix}$$

Equation 10

Where H_{ii} is the Hamiltonian describing form i (and is a function of the nuclear coordinates), V_{ij} is the coupling between forms i and j (and also depends on nuclear coordinates), and E_{ii} is

a modifier to account for differences in energy between the computed PESs and their true positions on the overall PES relative to H_{11}. This matrix can be extended to as many forms as are required to model the system. The overall PES is then produced by solving $\widehat{H}_{EVB}\underline{c} = E\underline{c}$ where $\underline{c}$ is the eigenvector of the equation with the lowest eigenvalue.

After the creation of a PES, simulations of collisions describing the changes in nuclear coordinates can be run as classical trajectories or quantum mechanical scattering on the PES. This process involves calculating the effect of the potential energy surface on the species (given that the force experienced by the nuclei along a specific coordinate is given by the gradient of the PES along that same coordinate) across a time interval of specified length, and using numerical integration methods to propagate the state of the system (i.e. to compute changes to the nuclear coordinates) appropriately. This integration cycle is then repeated, either until a certain time length has been considered or some other terminating condition is reached.[53]

Whilst Newtonian mechanics can be used to calculate the effect of the PES on the molecules in classical dynamics simulations, Lagrangian mechanics are normally favoured. This preference is due to Lagrangian mechanics having the advantage of being generalisable to any coordinate system, and that the Lagrangian equations deal with energies directly rather than forces. A system in Lagrangian mechanics is defined by the solution of a set of differential equations, one for each degree of freedom of the system. Each of these equations is in the form of Equation 11a.

$$\frac{d}{dt}\frac{\partial \mathcal{L}}{\partial \dot{\boldsymbol{q}}_i} = \frac{\partial \mathcal{L}}{\partial \boldsymbol{q}_i} \quad \text{a}$$

$$\mathcal{L}(\boldsymbol{q}, \dot{\boldsymbol{q}}, t) \equiv T - V \quad \text{b}$$

Equation 11

In these equations, $\boldsymbol{q}$ is the set of positions of the particles, $\dot{\boldsymbol{q}}$ is the differential of **q** with respect to time, and T and V are the kinetic and potential energies of the system.

A significant shortcoming of these classical mechanics methods, when applied to chemical systems, is the lack of quantization of properties such as vibrational and rotational energy levels. This omission of quantization can be accounted for before and after the simulations

are run, through initialising the reactants in quantized levels and through filtering[54-56] or binning[12] the outcomes into quantized levels. These processes are incorporated into so-called quasi-classical trajectory (QCT) methods.[13, 52, 57, 58] Maintaining quantization throughout the trajectory requires alternative methods, which are based on solving the Time Dependent Schrödinger equation (giving quantum wavepacket dynamics).[59-61]

1.4. Transfer Between Potential Energy Surfaces

Transfer of molecules between PESs can happen either through the absorption or emission of light, or through a non-radiative transfer process. Absorption of light can excite a species from a low-lying electronic state to a higher-lying electronic state, typically of the same total spin. This excitation can occur simultaneously with a change in vibrational state, in a vibronic transition. The electronic excitation is fast, relative to nuclear motion, leading to the Franck-Condon principle, which can be described either classically or quantum mechanically.

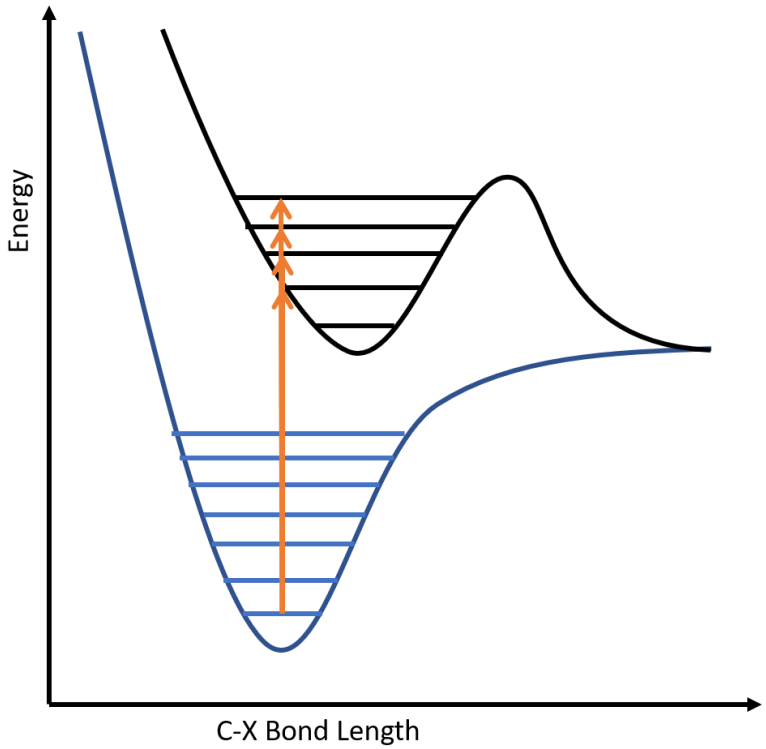

Figure 5: Demonstration of the Franck Condon Principle for excitation from the ground vibrational state of the initial electronic energy level, to excited vibrational states of the excited electronic energy level. The orange arrows show possible excitation pathways, with the specific pathway dependent on the excitation wavelength.

Classically, this principle can be considered to constrain electronic excitations to vertical movements on a PES (as shown in Figure 5), to account for the slow nuclear motion. As such, it is often required to excite into a vibrationally excited form of the upper electronic state, depending on the shape of the potential energy surfaces. Quantum mechanically, the transition probability is related to the overlap of the upper and lower state nuclear wavefunctions. The greater the overlap within the nuclear coordinate boundaries of the potential energy levels, the greater the transition probability.[62]

Following excitation, the species can either dissociate directly (if excited to a dissociative state, or a bound state above the barrier), isomerize, radiatively decay back down to a lower electronic state (via either stimulated or spontaneous emission), or transfer to another electronic surface. Such a transfer occurs via a coupling between the two surfaces, mediated by non-adiabatic dynamics (discussed in section 1.4.1), through the involvement of vibrational (i.e. vibronic coupling) or rotational (i.e. Coriolis coupling) modes, or via spin-orbit coupling.

Spin-orbit coupling is particularly prominent in species containing heavy atoms, such as 2,4-dibromofluorobenzene (which is investigated in Chapter 4). Relativistic effects in the heavy atoms lead to the electronic eigenstates of the molecule being poorly defined by either the individual electronic spin angular momentum (**S**) or the electronic orbital angular momentum (**L**), but well defined by the total electronic angular momentum (**J** = **L** + **S**). This significance of **J** leads to mixing between electronic states of different **S** values but the same overall angular momentum. This mixing allows transfers between, for example, singlet and triplet states that would otherwise not be possible.[63-65]

1.4.1. Non-adiabatic Processes

In some regions of an adiabatic PES, the Born-Oppenheimer approximation can fail to properly describe the properties of the surface. This failure occurs when the nuclear motion and electronic energy levels become strongly coupled, allowing the nuclear motion to take the species from one adiabatic energy level to another. The degree of coupling between adiabatic electronic states i and j, denoted as $\widehat{\Lambda}_{ji}$, is described by:

$$\widehat{\Lambda}_{ji} = \delta_{ji}\widehat{T}_N - \langle j|\widehat{T}_N|i\rangle$$

$$\widehat{T}_N = -\frac{\hbar}{2M}\nabla^2$$

Equation 12

Where $\widehat{T}_N$ is the nuclear kinetic energy operator, M is the reduced mass of the system, and δ is the Kronecker delta. If $i \neq j$, $\delta_{ji} = 0$ and the coupling term can then be simplified to a function of two terms $\mathbf{F}_{ji}$ and G_{ji}:[66]

$$\widehat{\Lambda}_{ji} = \frac{\hbar}{2M}\left(2\boldsymbol{F}_{ji}\cdot\underline{\nabla} + G_{ji}\right)$$

$$\boldsymbol{F}_{ji} = \frac{\langle j|\underline{\nabla}\widehat{H}_e|i\rangle}{U_i - U_j}$$

$$G_{ji} = \langle j|\nabla^2|i\rangle$$

Equation 13

Where U_i is the energy of state i, and $\widehat{H}_e$ is the electronic energy Hamiltonian operator. G_{ji} is normally negligible, so $\mathbf{F}_{ji}$ is the dominant term for non-adiabatic interactions. Equation 13 therefore demonstrates that coupling is high where the two adiabatic energy levels are close in energy (U_i-U_j is small) or the rate of change of electronic energy with respect to the nuclear coordinates, $\langle j|\underline{\nabla}\widehat{H}_e|i\rangle$, is large.

In this coupling process the species can travel along a pathway that conserves electronic configuration as the nuclei move, i.e. along a diabatic surface, as opposed to one where the electrons rearrange faster than nuclear motion (an adiabatic surface). As such, the identification and nature of points where the PE surfaces cross can also be calculated in terms of these diabatic surfaces. The coupling between any given pair of these diabatic states ϕ_1 and ϕ_2 to produce the adiabatic state $\phi = c_1\phi_1 + c_2\phi_2$ comes from a perturbative operator added to the diabatic Hamiltonian, i.e. $\widehat{H}_e = \widehat{H}_{e,diabatic} + \hat{V}$. The energetics of such a system are described by Equation 14a, where $H_{ij} = \langle i|\widehat{H}_e|j\rangle$, with roots according to Equation 14b.

$$c_1(H_{11} - E) + c_2 H_{12} = 0$$
$$c_1 H_{21} + c_2(H_{22} - E) = 0$$

a

$$E_{\pm} = \frac{1}{2}\left[(H_{11} + H_{22}) \pm \sqrt{(H_{11} - H_{22})^2 + 4|H_{12}|^2}\right]$$

b

Equation 14

From Equation 14b, for two adiabatic states to cross the difference in energy between the constituent diabatic states must be zero, and the coupling between them must also be zero. This requirement generally needs two degrees of freedom to satisfy - one to modify $H_{11} - H_{22}$ independent of H_{12}, termed the "tuning coordinate", and another to modify H_{12} independent of $H_{11} - H_{22}$, termed the "coupling coordinate". Diatomic molecules only have one degree of freedom, so they cannot satisfy both conditions simultaneously. As such, the minimum energy difference between two adiabatic states is $2|H_{12}|$. All polyatomic molecules have at least 3 degrees of freedom, so can satisfy both conditions simultaneously, and therefore adiabatic states of polyatomic molecules can cross at specific points. These crossings are termed 'conical intersections', due to their biconical shape around the crossing point, as is shown in Figure 6. Near a conical intersection, molecules can either "skirt" the conical intersection, remaining on the same adiabatic surface, or pass through the coupled geometry to transfer from one adiabatic state to the other. These two options are shown in Figure 6 by the blue and orange pathways respectively.[67-69]

1.5. Molecular Beams

Experimental investigations of gas-phase molecular dynamics typically use molecular beams as the source of the species of interest.[70] These molecular beams provide a controlled source of molecules suitable for injection into an otherwise high-vacuum environment. This high vacuum substantially reduces the level of unwanted collisions, allowing the collision of interest to be investigated with minimal interference. A bath or "carrier" gas can also be mixed with the species of interest in the molecular beam to relax the rotational or vibrational energy levels (depending on the species used) to the ground state. Alternatively, further equipment using processes such as the Stark or Zeeman effects can be used to slow the particles or select specific quantum states.[71-73]

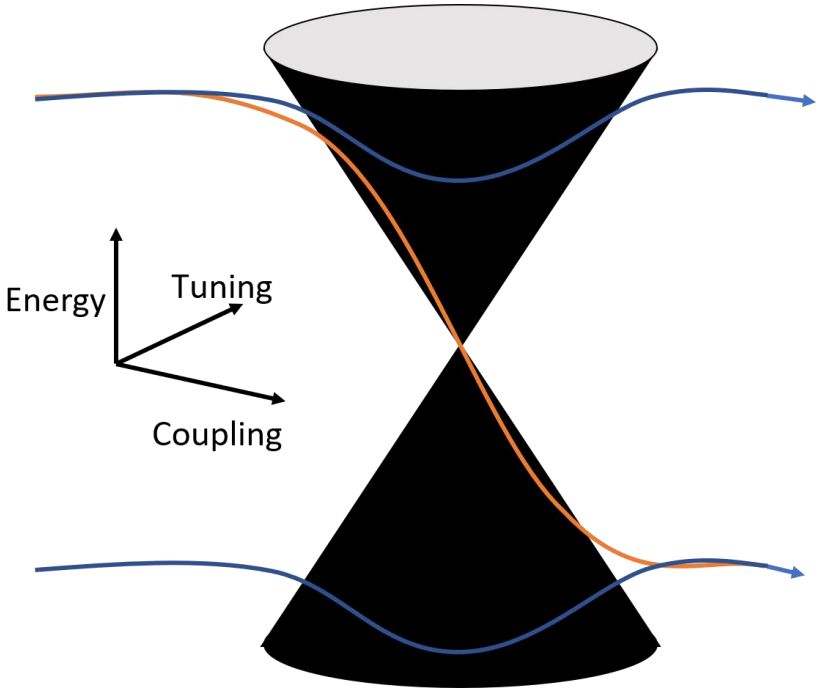

Figure 6: Depiction of a conical intersection of two adiabatic PESs, representing the energy as a function of the tuning and coupling coordinates. Blue arrows show pathways along the two adiabatic states, while the orange pathway follows the non-adiabatic route between the states.

The following section summarises the physics of supersonic expansions, as it relates to the molecular beams utilised in the present work. This summary is based on the thorough treatment in "Atomic and Molecular Beam Methods", edited by Giacinto Scoles and published by Oxford University Press in 1988.

1.5.1. Supersonic Expansions

A supersonic expansion occurs when a molecular source expands from a region of high pressure (the "stagnation chamber"), to a region of significantly lower pressure. The difference in pressure needs to be at least a factor of 2.1 for a supersonic expansion to occur, although in molecular dynamics experiments a typical pressure differential around 10 orders of magnitude is used.

Supersonic expansions can either be pulsed or continuous, however in terms of the physics involved a pulsed source with an expansion length of comparable or greater length than the distance between the source and the interaction region can simply be considered a gated continuous source. Considering a typical molecular beam velocity of 10^3 ms^{-1}, and typical opening time of the nozzles used in this work of 200 µs, the distance to the interaction region

would need to be on the order of metres for pulsed physics to be applicable. Since the distance in the experiments discussed in this work is on the order of centimetres, pulsed physics can be safely disregarded, and the discussion here focuses on the properties of a continuous supersonic expansion.

Figure 7 depicts the key regions and properties of such an expansion. Many regions can be defined based on the velocity as a ratio of the local speed of sound (the Mach number, denoted 'M'), with a series of boundaries between areas of distinct behaviour. The main supersonic expansion is surrounded by a barrel shock boundary, and a terminal Mach disk at the front of the expansion. The barrel shock boundary denotes the limit that disruptions from the outer, jet boundary can penetrate the molecular beam. This outer region exhibits more complex physics than the main supersonic region, so skimmers are typically used to narrow the beam and thin out this region.

The length of the supersonic region, X_M, in units of the nozzle diameter (d), is determined by Equation 15. Considering even a weak vacuum pressure of 10^{-4} mbar, along with typical nozzle diameters on the order of a millimetre, X_M takes values in excess of a metre. As such, under most experimental conditions, the significance of the Mach disk and the subsequent subsonic region can be safely ignored.

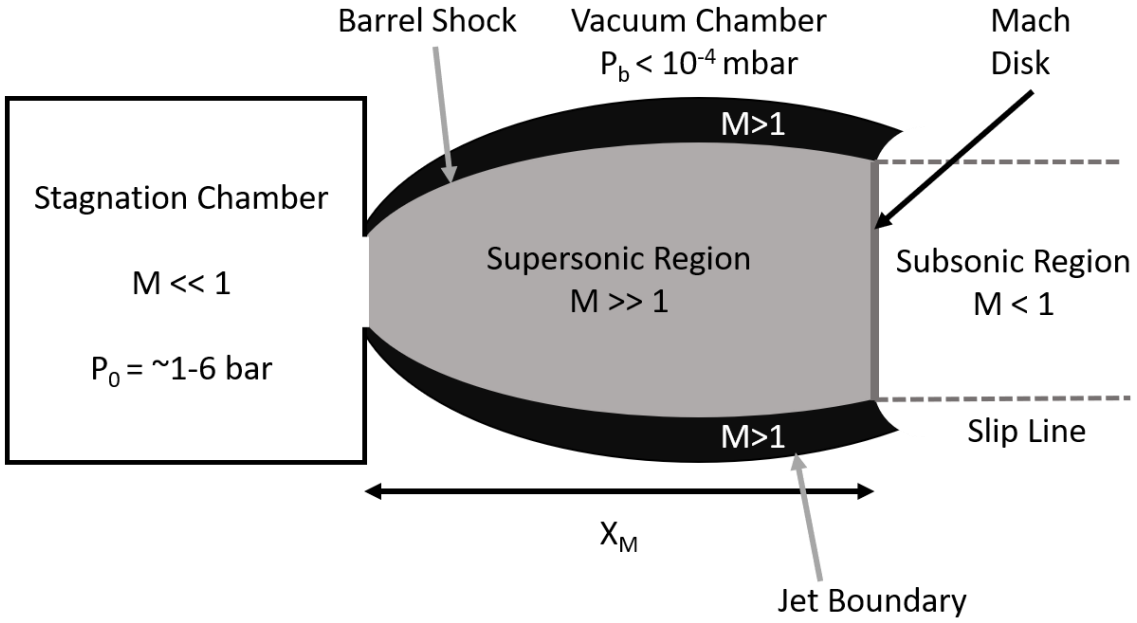

Figure 7: Diagrammatic representation of a continuous, supersonic molecular beam source. M refers to the Mach number, the velocity of the molecules divided by the local speed of sound.

$$\frac{X_M}{d} = \frac{2}{3} \cdot \left(\frac{P_0}{P_b}\right)^{1/2}$$

Equation 15

Within the supersonic region the properties of the beam are defined by the heat capacity of the beam. During the expansion, the temperature of the beam reduces through the enthalpy of the system being converted to velocity. The flow velocity, v, of the system within the supersonic region can therefore be defined based on this change in temperature, from an initial value T_0 to a final value T:

$$v^2 = 2\int_{\mathrm{T}}^{\mathrm{T_0}} \mathrm{c_P}\ \mathrm{dT} \approx 2\mathrm{c_P}(\mathrm{T_0} - T)$$

Equation 16

Where the second equivalency assumes ideal gas conditions. The limit of this velocity occurs when T becomes negligible with respect to T_0, (i.e. $(T_0 - T) \rightarrow T_0$), where the equation becomes:

$$v_{max} = \sqrt{2c_P T_0} = \sqrt{\frac{2R}{W}\frac{\gamma}{\gamma - 1}T_0}$$

Equation 17

Where $\gamma = \frac{c_P}{c_V}$, W is the molecular weight of the species, and using $C_{P,m} - C_{V.m} = R$ due to the ideal gas assumption. This velocity can then be contrasted with the equation for the speed of sound in an ideal gas under classical conditions, which is

$$v_{sound,ideal} = \sqrt{\frac{\gamma RT}{W}}$$

Equation 18

Equation 17 demonstrates that as T becomes negligible relative to T_0 the velocity increases by a small factor (e.g. up to $\sqrt{2.5}$ for a monatomic gas). Meanwhile Equation 18 shows that the speed of sound decreases drastically. It is this drastic decrease which produces the high Mach numbers observed in the supersonic region.

In a supersonic expansion a molecule will still undergo collisions, at a rate highest nearer the stagnation chamber. A typical molecule will undergo 100-1000 bimolecular collisions in the

duration of a supersonic expansion. Internal energy relaxation can occur through these inelastic collisions and can be encouraged by the introduction of a buffer gas. Heavy inert gases (particularly noble gases) are frequently used to cool the rotational energy distribution of a sample to predominantly the ground state, while diatomic gases such as N_2 can efficiently cool vibrational energy levels. The final velocity of such a molecular beam can be found using Equation 17, by substituting the weighted average of the properties of the species involved.

1.6. Velocity Map Imaging

Velocity Map Imaging is a refinement of the ion-imaging method introduced by Houston and Chandler[74] which enables mass-selective detection of particles along with the precise details of their distributions of initial velocity magnitudes and spatial anisotropy.[75-78] The technique uses a Repeller and Extractor pair to accelerate ions down a time of flight tube to a detector, typically consisting of a microchannel plate stack paired with a phosphor screen. Mass separation of the ions is achieved through the charges on the Repeller and Extractor imparting a kinetic energy on each ion that is only proportional to the charge on the ion.

The ratio of the voltages is then chosen such that all ions of a particular initial velocity map onto the same point on the detector. Further charged plates are typically added, which act as an Einzel lens to expand each set of ions into a third dimension. The result of the entire ion optics stack is ions of each mass forming a “Newton sphere”, of the form shown in Figure 8. This Newton sphere is characterised by the radius being proportional to the initial speed of the ion, and with anisotropic effects of the velocity distribution maintained. For example the Newton sphere shown in Figure 8 would come from a process with a mild preference for velocities aligned vertically in the plane of the figure. Detection can either use crushed imaging or DC sliced imaging,[77, 79] with the results of both methods shown in Figure 8. Crushed imaging detects the entire Newton sphere in 2 dimensions, resulting in an image similar to the left of Figure 8 and requiring further analysis to deconvolve.[80-82] DC sliced imaging instead detects only the central slice of the image, allowing the character of the Newton sphere to be immediately observable. More recently, high frame rate cameras such as the PImMS camera[83, 84] can take multiple slices of the same Newton sphere. This fast frame rate allows anisotropy in the time dimension to also be observed, as well as allowing multiple mass channels from the same laser pulse to be observed, allowing covariance analysis to be performed.[85-88]

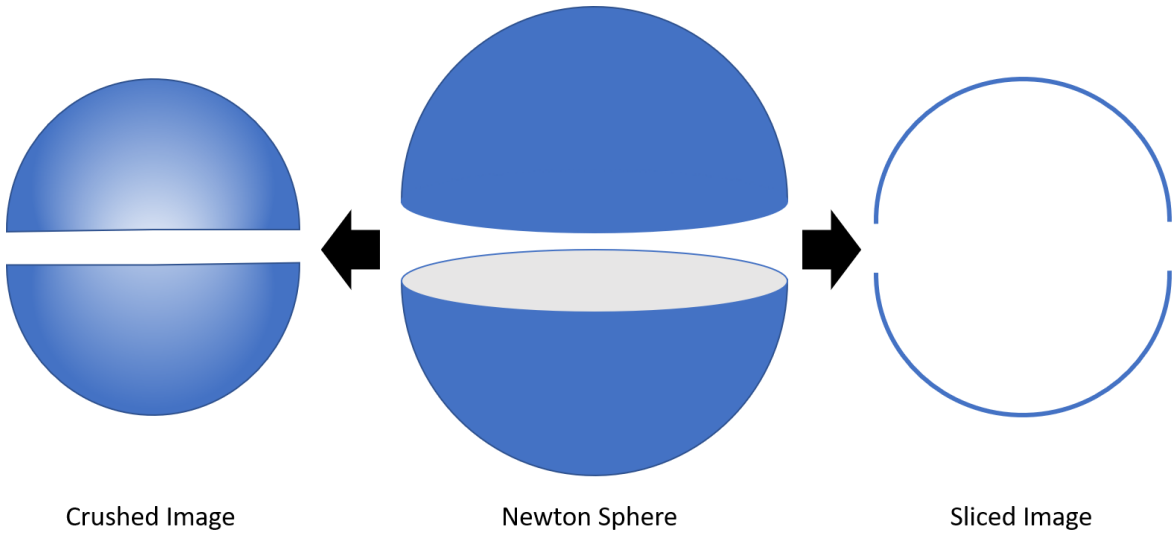

Figure 8: Depiction of a Newton sphere, along with the two possible 2D representations: a crushed image with all the ions along the third axis collected in the same point, or a sliced image where only the central slice of the Newton sphere is detected.

Scattering angles in the CoM frame can be determined by considering angles relative to the centre of the circle or arc of the signal, rather than relative to the centre of the detector. The shift between these two reference points is a consequence of the CM velocity vector. This determination of the CoM frame is illustrated in Figure 9, showing the inelastic scattering of NO and Argon (part of a data set discussed in Chapter 5). The arrows marked V_{NO} and V_{Ar} show the initial laboratory frame velocities of the NO and Argon, with the centre of mass velocity shown by V_{com}. The CoM frame relative velocity axis is then shown as the fourth line across the image, with the VMI image showing increased intensity in the NO forward-scattering direction (with scattering angle θ taking preferred values around 0^o) at the top of the image.

VMI images are normally produced from the result of a laser ionisation of the species of interest, often using a resonance enhanced multiphoton ionization (REMPI) scheme.[89] Since this ionisation is applied to a fixed volume (i.e., that of the laser passing through the interaction region), the ion count produced is a measure of the density of the detected product, rather than the flux. For example, a slow-moving product in the laboratory frame will have a higher density near to the area that it has been produced, and *vice versa* for a fast product. This density difference will lead to over-detection of the slow product and under-detection of the fast product.

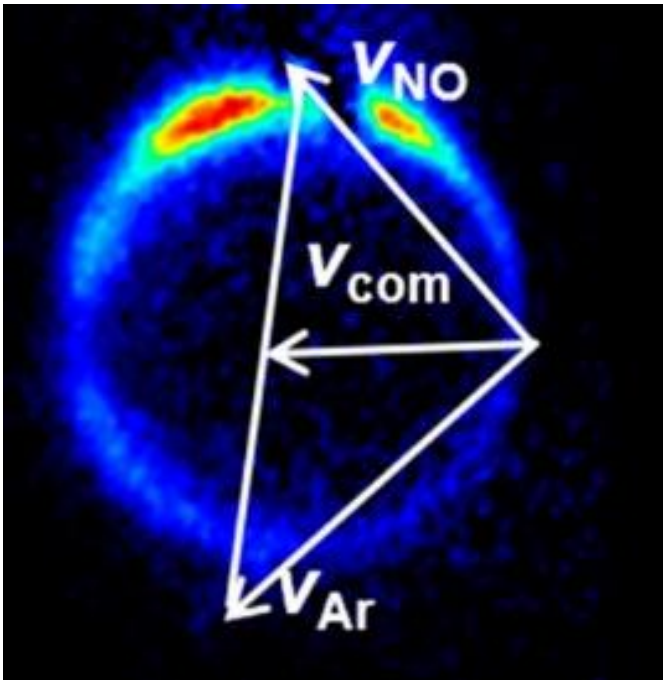

Figure 9: Velocity map image for the inelastic scattering of NO with Argon, detecting j'_{NO}=7.5, with a schematic Newton diagram overlaid.

As such, a density to flux correction is needed to provide an accurate determination of the rate of a process from a VMI image. Furthermore, in a scattering process the CoM frame angles are related to different laboratory frame velocities, so the density-to-flux correction influences the differential cross section observed too. A simple density-to-flux correction can be performed by dividing the signal at each point by the lab frame velocity, however more accurate corrections involve Monte Carlo simulations of the correction factor at multiple points in the lab frame, with an interpolation method used to create the correction function.[77, 90]

1.6.1. Anisotropy Parameter

In many photodissociation processes, the recoil velocities of the photofragments are distributed anisotropically in space, with preference for recoil either along or perpendicular to the direction of polarization of the photolysis light. This spatial anisotropy is a consequence of the interaction of the light with the dipole moments of the molecules. The probability of an absorption occurring between two electronic energy levels f and i is given by:[62]

$$I_{fi} \propto (P_i - P_f)\left|\langle \psi_f | \boldsymbol{\mu} \cdot \boldsymbol{\varepsilon} | \psi_i \rangle\right|^2$$

Equation 19

Where P_x and ψ_x are the population and wavefunction of state x respectively, $\boldsymbol{\mu}$ is the dipole moment operator and $\boldsymbol{\varepsilon}$ is the polarization vector of the incident light. The dot product means that the transition probability is dependent on the angle (θ) between the transition dipole moment, $\langle\psi_f|\boldsymbol{\mu}|\psi_i\rangle$, and the polarization of the light source, and follows a $\cos^2\theta$ distribution.

If the molecule subsequently dissociates along an axis at an angle γ to the transition dipole moment, the resulting distribution in a VMI image captured in a plane parallel to the laser polarisation axis follows:[91]

$$I \propto \frac{1}{2}\left(1 + 2P_2(\cos(\gamma))P_2(\cos(\theta))\right)$$

Equation 20

Where the angular dependencies have been re-expressed in the form of the 2nd order Legendre polynomial, $P_2(x) = \frac{1}{2}(3x^2 - 1)$. The value $2P_2(\cos(\gamma))$ is then defined as the anisotropy parameter, β, which can take values $-1 \leq \beta \leq 2$. A β value of 2 describes the situation where the transition dipole moment and dissociation axis are perfectly parallel, following the $\cos^2\theta$ distribution, while -1 describes when the two axes are perfectly perpendicular and the intensity follows a $\sin^2\theta$ distribution.

Intermediate values of β either result from values of γ between 0° and 90°, or from rotational averaging. Rotational averaging occurs when dissociation is delayed after the absorption, by a duration on the order of a rotational period. This delay reduces the correlation between the initial excitation and the resultant dissociation vectors. As a result the value of β is reduced to β_{eff}, by a factor based on the product of the average excited state lifetime $\langle\tau\rangle$ and the angular velocity of the species ω:[92]

$$\beta_{eff} = \beta\frac{1 + (\omega\langle\tau\rangle)^2}{1 + 4(\omega\langle\tau\rangle)^2}$$

Equation 21

1.7. Thesis Overview

Chapter 2 will introduce the computational and experimental techniques used in this thesis in a practical context, building on the theoretical treatments discussed in this chapter.

Following this, Chapter 3 presents computational investigations into the reactive scattering of chlorine atoms with propene. This investigation uses the QCT method, on a previously published PES,[51] to produce novel insights into the impact of varying the collision energy of the system and the pathways taken during the reaction.

The remainder of the thesis will then discuss experiments undertaken during the development of an experimental apparatus. Chapter 4 reports investigations into the photodissociation of 2,4-dibromofluorobenzene in the 260 – 285 nm region, extending earlier studies that described the absorption spectrum of the species.[93, 94] This work couples experimental investigations and low-level computational calculations to assign dissociative pathways on the excited PES, in comparison with simpler bromofluorobenzenes. Chapter 5 progresses on to studies of the inelastic scattering of methane and NO, where the state-to-state differential cross sections are presented. These cross sections are compared to those of the inelastic scattering of NO with argon, and result in suggestions of the pathways involved through analysis of the rainbow angles. Chapter 6 then records progress towards reactive scattering on the same apparatus. Although no reactive scattering has been observed prior to suspension of experimental work, significant progress has been made. In particular, this chapter reports the reliable production of cyanogen radicals, required for the intended future study of the reaction between cyanogen radicals and methane.

Finally, Chapter 7 summarises the results presented in this thesis, and discusses their significance along with the potential topics for related future investigations.

2. Experimental and Computational Methods

2.1. Experimental

Chapters 4 - 6 report the results of experimental studies utilising a VMI apparatus. This apparatus is the result of iterative developments across a number of researchers at Bristol, with a previous version being presented in the thesis of Dr Shubhrangshu Pandit.[95] Much of the theory behind the VMI technique is covered in Chapter 1. In this chapter I present details of the apparatus, including the modifications made from the previous version, as well as briefly covering the laser systems used alongside the apparatus.

The VMI technique originates from the work of Eppink and Parker. This work used ionisation of a single molecular beam, followed by acceleration using a Repeller and an Extractor plate. This technique mapped all ions with the same velocity onto the same spot on the detector, with time of flight separation by mass.[75] This approach has since been combined with the crossed molecular beam work first used by Herschbach[96] and developed further by Y. T. Lee.[97] This work by Herschbach and Lee led to them receiving the 1986 Nobel Prize in Chemistry, alongside IR chemiluminescence work by Polanyi.[98] The extended VMI optics design was developed first by Gebhardt *et al.*, who designed a pulsed optics system which expanded the Newton sphere relative to that of Eppink and Parker's apparatus. This enables sliced imaging at the detector, and can remove the need for reconstruction of the Newton sphere.[76] Kopin Liu *et al.* subsequently improved on this design, using a static ion optic system with lenses to have the same effect of expanding the Newton sphere whilst introducing the combination with crossed molecular beams.[77]

The method described here is an adaptation from that described in Liu's work, using an extended ion optics stack to elongate the Newton sphere. However fewer lenses are used than in Liu's work.

2.1.1. Vacuum Chamber Apparatus

The experimental apparatus used in this work consists of three segments: a source chamber, a time of flight (TOF) tube, and a detection chamber. The TOF and detection chambers remain unchanged from those used by Dr Pandit, consisting of two horizontal stainless-steel tubes of total length 85 cm, terminated with a 75 mm diameter microchannel plate (MCP) and

phosphor screen combination detector. In the experiments reported here, the middle and rear plates of the MCP detector were held at 600 V and 1200 V respectively, with the phosphor screen held at 4.5 kV. The front plate of the detector was pulsed from ground to -450 V with a pulse width of up to 100 ns, to provide DC slicing of the Newton sphere. This detector was then imaged externally by a CCD camera, in turn controlled via LabView scripts.

Both the TOF and detection chambers were evacuated by separate turbomolecular pumps (Oerlikon Turbovac Mag W 300 iP and Edwards nEXT 400D), which were in turn both backed by a rotary pump (Edwards RV8). An ion gauge was attached to the detection chamber to monitor the pressure. A gate valve was situated between the TOF and detection chambers, to keep the MCPs under vacuum when the rest of the chamber is vented. Pressures in both the TOF and detection chambers were typically on the order of $5x10^{-8}$ mbar with no gas load from the nozzles, rising to pressures around $5x10^{-7}$ mbar with the nozzles firing.

The significance of the high vacuum is to minimise further collisions occurring after interacting with the probe laser. The likelihood of further collisions can be inferred from the mean free path, which for an ideal gas is calculated as:

$$\bar{l} = \frac{k \cdot T}{\sqrt{2} \cdot \pi \cdot p \cdot d_m^2}$$

Equation 22

Where $\bar{l}$ is the mean free path, $d_m$the molecular kinetic diameter and p, T and k are the pressure, temperature, and Boltzmann constant, respectively. Using a molecular kinetic diameter for Argon of 340 pm,[99] the mean free path at 298 K and $5x10^{-7}$ mbar is 160 m, much larger than the ~1 m distance from the interaction region to the detector. As such, it is reasonable to expect that no further collisions occur in this region.

The source chamber has undergone significant development, originating from a new design created by Dr Mitchell Quinn and Dr James Smith, with subsequent iterative characterisation and development performed by the author of this thesis and Dr Mitchell Quinn, Dr Patrick Robertson and Dr Xu-Dong Wang.

The fundamental shape of this source chamber was of a six-way cross, with each flange perpendicular to four others and opposite one. This was oriented with two flanges along the time of flight axis, and the remaining flanges 45° above and below horizontal on each side.

This design allows reactions to be studied under either parallel beam conditions, with General Valve nozzles (Parker, Series 9, 0.8 mm straight cylinder orifices) pointed along the time of flight axis, or under perpendicular or antiparallel beam conditions. The latter two options used nozzles perpendicular to the time of flight axis, on a selection of the four side flanges. In parallel and perpendicular beam conditions, the chamber was evacuated by two turbomolecular pumps mounted on the two flanges below horizontal on each side, shown on the lower left and lower right of Figure 10a (Edwards nEXT 85H and Oerlikon Turbovac Mag 600 iP). These were each backed with rotary pumps (Leybold Trivac D8B and Edwards RV8). In the case of perpendicular beam conditions, a third turbomolecular pump, backed with a further rotary pump (Oerlikon Turbovac Mag W 600 P and Edwards RV8) replaced the in-axis nozzles, on the large flange shown partially transparent to the left of Figure 10a. The rig is yet to be used in an antiparallel configuration. Two further ports were present on either side of the vacuum chamber, along the horizontal axis, which were fitted with UV fused silica windows. This was the path used by any lasers interacting with the species within the ion optics region (see section 2.1.2 for details on the laser systems used).

The VMI optics consisted primarily of 3 circular metal plates, acting as the Repeller, Extractor and Lens, each able to be directly charged to a variable potential. Further stabilising plates have been added, with one between the Extractor and Lens held at 90% of the Extractor voltage, and 2 beyond the Lens at 2/3 and then 1/3 of the Lens voltage. These voltages were created by addition of megaohm resistors between the parent plate, the stabilising plate, and the ground. The configuration of the plates is shown in Figure 11. The lens and stabilising plates were used to reduce the electric field gradient between the Repeller and Extractor pair and the time of flight region, enabling the previously mentioned expansion of the Newton sphere to occur.

In the initial configuration, these ion optics were fully exposed to the source chamber, with rods used to hold in place nozzle guides and 0.5 mm skimmers. This arrangement is shown in Figure 10a. As such, this configuration did not utilise any form of differential pumping- a technique common in many other VMI configurations. Whilst this was workable for single molecular beam conditions, it proved unworkable for dual molecular beam conditions due to high levels of background gas.

a)

b)

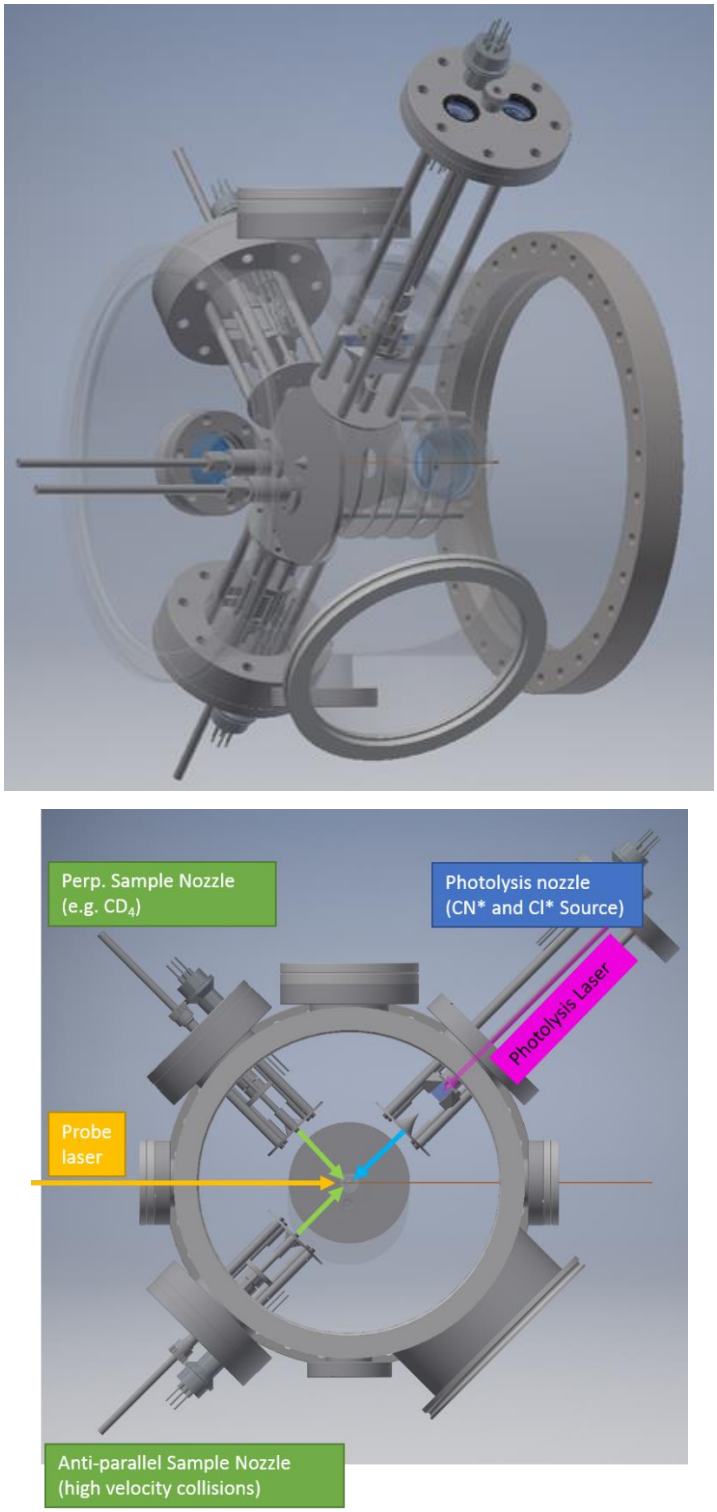

Figure 10: Perspective (a) and end-on (b) views of the original source chamber, showing the nozzle arrangements for parallel molecular beams (figure (a), to the left) and perpendicular ("Perp.") and antiparallel molecular beams, which both use the photolysis nozzle to the upper right and either the upper left or lower left nozzle respectively. The laser path is shown in (b), passing through the ports either side of the central VMI optics in both images. The photolysis laser is shown in the prism configuration. Images and CAD design were created by Dr Quinn.

a)

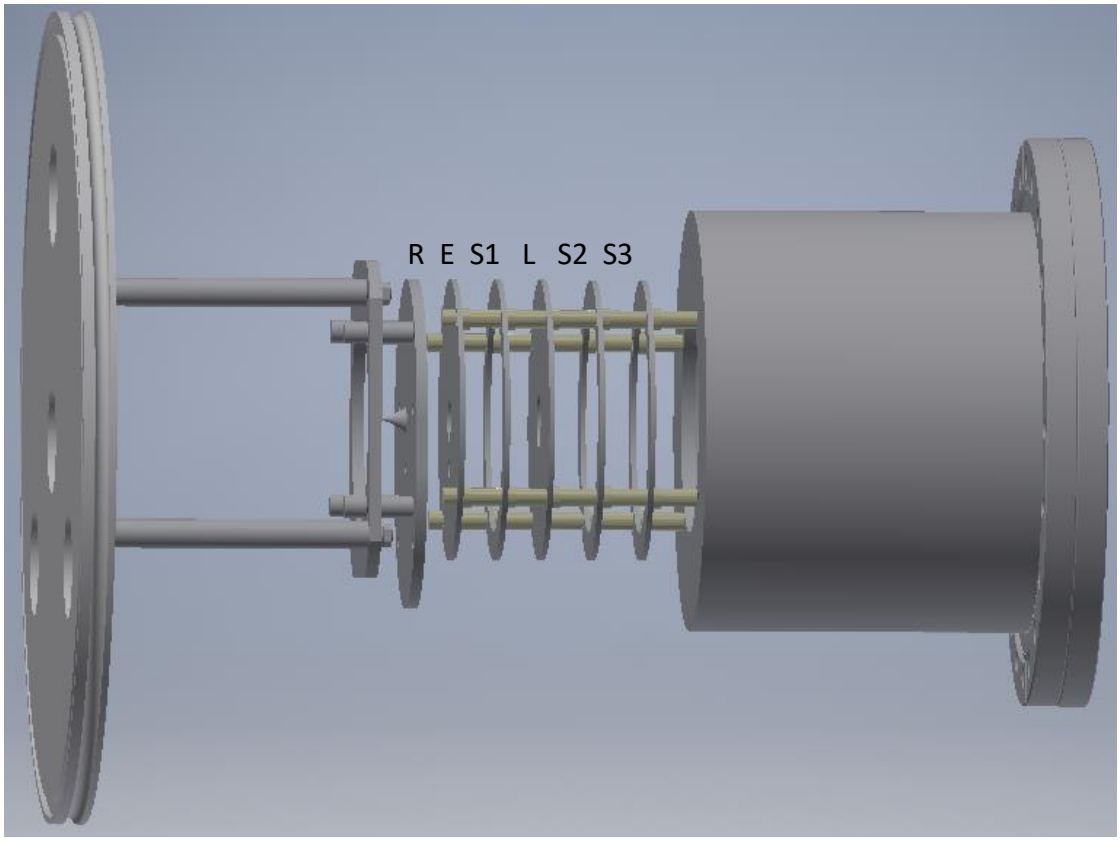

b)

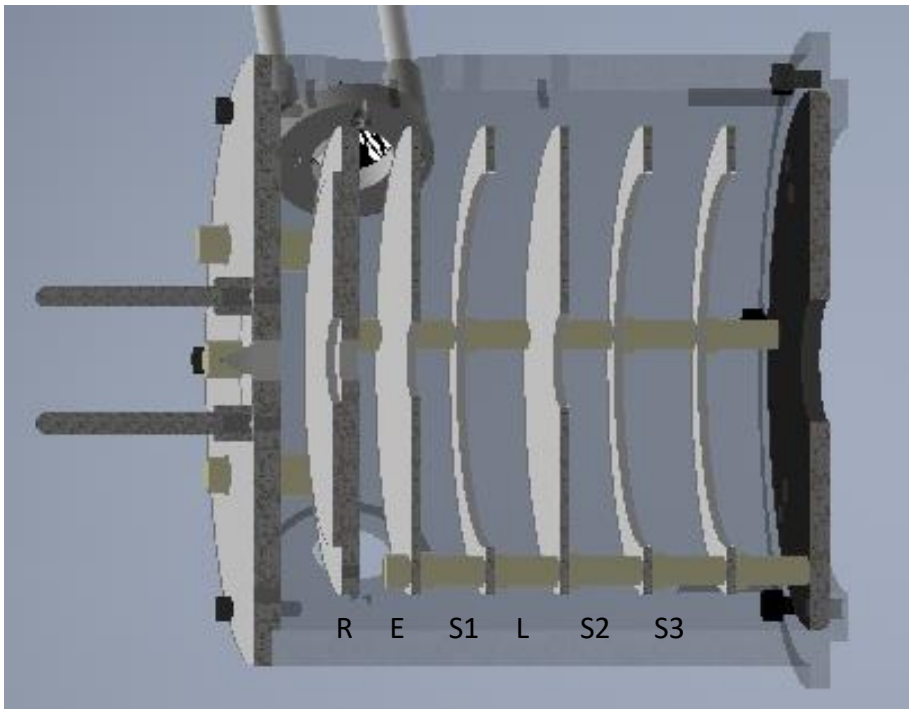

Figure 11: CAD images of the ion optics, with the Repeller, Extractor and Lens labelled “R”, “E” and “L” respectively and the three stabilising plates labelled S1 through S3. Image (a) shows the original design, which was open to the source chamber. Image (b) shows the updated design, with a sheath or “bucket” fitted around the ion optics. Images were made using CAD files created by Dr Quinn.

A sheath or “bucket” was therefore designed by Dr Quinn and added around the ion optics stack. This barrier was designed to reduce the amount of gas flow into the ion optics region from the remainder of the source chamber, and therefore approximated a differential pumping situation between the outer source chamber and the ion optics region. Holes were positioned in the bucket in the direction of each of the 4 main ports in the source chamber, which either hold a skimmer or are used to vent into the turbomolecular pumps. Two further, smaller holes enable a laser path through the bucket. A cut-through of this construction is shown around the ion optics in Figure 11b, and a partially transparent view is presented in Figure 12.

Since it was suspected that the unskimmed holes were admitting gas into the ion optics region, despite their proximity to the pumps, additional tubes were designed and fitted by Dr Wang reducing the distance between the open end of the vent and the entrance to the pump, which reduced background noise levels.

Unlike in a typical differential pumping arrangement, no pumps were used to directly evacuate the ion optics region. Instead the region was evacuated with the source chamber pumps, as described above, and through the hole between it and the time-of-flight region.

A further benefit of the bucket has been in fixing the relative angle of the nozzles. Prior to the addition of the bucket, one of the crossed molecular beam nozzles was attached to a bellows enabling adjustment of the angle of the nozzle. This was required due to the nozzle’s weight, and slight elasticity of the holding rods, meaning that two statically mounted nozzles in this configuration may not produce good molecular beam overlap. However, these bellows required frequent adjustment. The rigidly mounted bucket provided support within the chamber, with guide rods attachable at each port. This design fixed the molecular beam angle at 90° near the interaction region and removed the need for a bellows to optimise overlap. These nozzle guides are shown in Figure 12.

The photolysis laser system was developed during the work detailed in Chapter 6. This configuration consisted of two external ports on one arm of the source chamber, allowing a laser path into the chamber, through an arrangement of optics which directed the beam across the face of the nozzle, and then back out the chamber. This return path was intended to be used for alignment, to confirm the beam is passing across the nozzle face. The optical

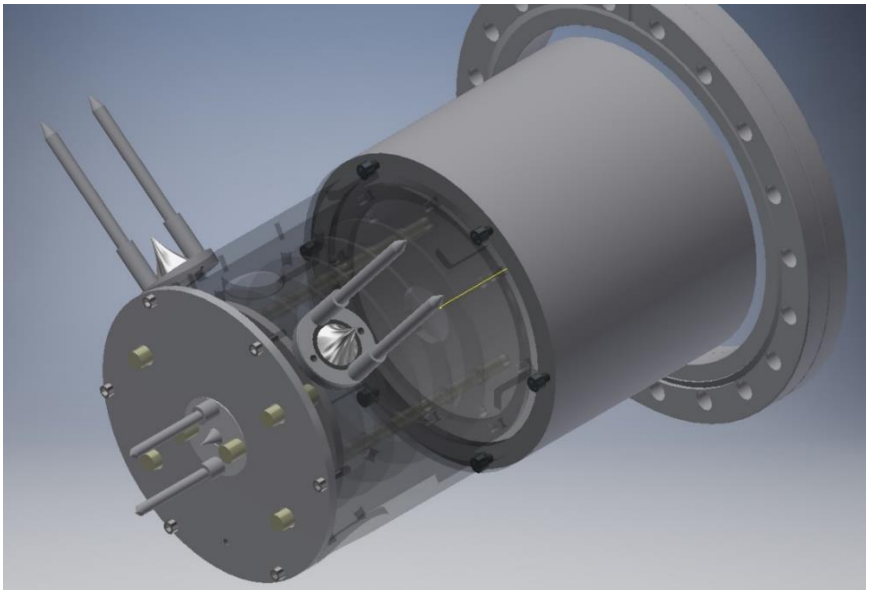

Figure 12: Partially transparent view of the “bucket” and ion optics mount, showing the mounting of the skimmers and nozzle guides on the sheath. Image were made using CAD files created by Dr Quinn.

a)

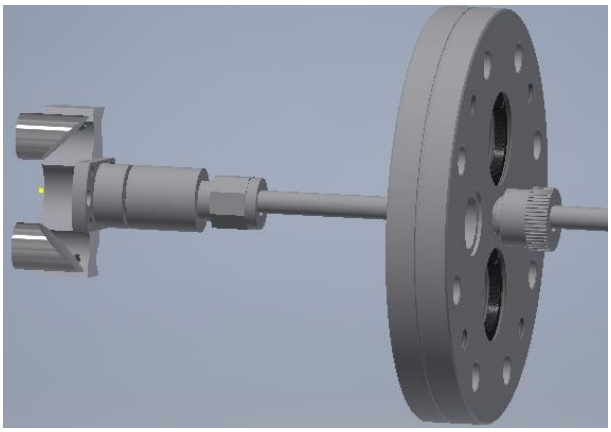

b)

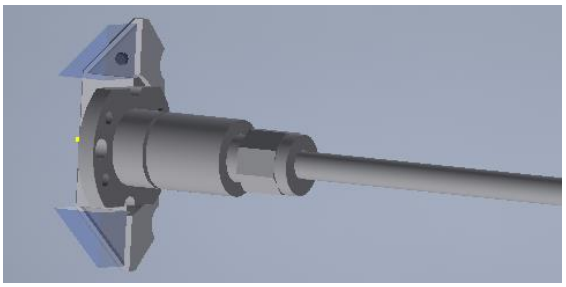

Figure 13: Partial cutaways showing the photolysis nozzle system. (a) shows the parabolic mirror model, with half of the holding bracket removed for visibility, along with the two laser ports on the outer flange to allow a laser path through the mirrors. (b) shows the alternate version, utilising two prisms, based on the design of Drs Tkáč and Greaves. Images were made from CAD files created by Dr Quinn.

design for this laser beam path originally used two right-angular parabolic mirrors, with focal lengths of 15 mm, 12 mm either side of the outlet of the nozzle. This design was ultimately unsuccessful, and was replaced by a pair of right-angled prisms in the same positions, in a design based on that of Dr Ondřej Tkáč and Dr Stuart Greaves.[100] These two designs are shown in Figure 13.

2.1.2. Laser System

The laser systems used consisted of three types: Nd:YAG lasers, ArF excimer/exciplex lasers, and Fluorescent dye lasers. The specific combinations of lasers used are described in the results chapters, with the key principles of each described here.

2.1.2.1. Nd:YAG lasers

Nd:YAG lasers utilise the 1064 nm emission in Nd^{3+} atoms, relaxing from the $^4F_{3/2}$ to the $^4I_{11/2}$ electronic state, when perturbed by the field of a $Y_3Al_5O_{12}$ (Yttrium-Aluminium-Garnet, YAG) crystal. The population inversion required for laser action is produced by Krypton flash lamps, with absorption by the Nd^{3+} occurring at either 730-760 nm or 790-820 nm.[101] This fundamental emission at 1064 nm can be frequency doubled to produce laser radiation at the second harmonic wavelength of 532 nm (Second Harmonic Generation, SHG). This second harmonic can then be mixed with the 1064 nm fundamental to produce the third harmonic wavelength at 355 nm (Third Harmonic Generation, THG), or frequency doubled itself to produce the fourth harmonic at 266 nm (Fourth Harmonic Generation, FHG). In this work, dichroic mirrors were used after the harmonic generator stages to separate out the harmonic needed from residual fundamental and lower harmonics. Harmonics 2 through 4 were all used in the course of the work presented in this thesis, either directly or as the source to pump a subsequent dye laser.

2.1.2.2. Fluorescent Dye Lasers

Dye lasers operate using chemicals with highly efficient fluorescent pathways, combined with closely spaced vibrational levels within the electronic states. The emission is induced by excitation by a pump laser from the S_0 state of the dye molecules to a vibrationally excited level within the S_1 electronic state. This is followed by rapid, radiationless relaxation to the ground vibrational state of S_1. Fluorescence then occurs between this state and a range of

vibrational energy levels of the S_0 state. By this method, laser excitation at a single wavelength produces fluorescence at a wider band of wavelengths which are all longer than the initial excitation wavelength. The fluorescence is amplified by a lasing cavity, via stimulated emission. A grating is used to select an individual wavelength, followed by more amplification stages using stimulated emission after excitation by the same initial laser source.[102] In the current work the output of the dye lasers was frequency doubled with a β-barium borate (BBO) crystal to create radiation of a chosen wavelength in the UV region. The optimum angle of the crystal for doubling is dependent on the wavelength of the incident light, so wavelength scans utilised a motorised mount following a pre-recorded calibration plot. Narrow band dichroic mirrors were used in the beam line to separate the UV light from the residual fundamental.

2.1.2.3. Excimer/Exciplex Lasers

Excimer (Excited Dimer) and Exciplex (Excited Complex) lasers create a population inversion by inducing the formation of an excited bound species from two otherwise unbound species, created from a combination of pressure and electrical discharge. This excited species subsequently relaxes to the ground state through fluorescence. This fluorescence wavelength is characteristic of a specific gas mix; in this work, we used Argon-Fluorine exciplex formation, which emits at 193 nm.[103]

2.1.3. REMPI Spectroscopy

Resonance Enhanced Multi-Photon Ionisation (REMPI) is used in the experimental procedures described in this thesis to provide quantum state selective detection of certain species. These processes are described by a (n + m) marker, e.g. (2 + 1) REMPI. Here the n denotes the number of photons absorbed by the species to reach an excited resonant electronic state, followed by absorption of m photons to ionise the molecule from that state. The initial resonant excitation makes the process dependent on the species being in a specific quantum state, so REMPI spectroscopy can be used to infer the quantum state distribution of a reaction or photodissociation product and any features specific for each state. The REMPI detection schemes used in this thesis are listed in Table 1.

Species	Wavelength /nm	REMPI Type	Resonant Transition
Br	260.61	2+1	$5p^4D_{3/2} \leftarrow {}^2P_{3/2}$ [104]
	266.63	2+1	$5p^4P_{3/2} \leftarrow {}^2P_{3/2}$ [104]
	266.69	2+1	$5p^4S_{3/2} \leftarrow {}^2P_{1/2}$ [104]
I	265.91	2+1	$({}^3P_2)7p[1]_{1/2} \leftarrow {}^2P_{3/2}$ [105]
CH_3	286.26	2+1	$4p_z{}^2A_2'' \leftarrow \tilde{X}^2A_2''$ [106]
NO	225-226	1+1	$A^2\Sigma^+ \leftarrow X^2\Pi$ [107]

Table 1: REMPI Schemes used in this thesis

2.1.4. Molecular Beams

Molecular beams were generated using pulsed General Valve nozzles (Parker Series 9), driven by 28 V pulse generators at a 10 Hz repetition rate. PTFE poppets and seals were used for Methane and O_2 gases, with Vespel used for NO and cyanogen halides due to the enhanced chemical resistance.

These nozzles were connected to one of two gas manifolds. These contained cylinders for pre-mixes to be made up of gaseous species of interest with the carrier gas, which could then be passed to the nozzles via a built-in regulator. Solid and liquid species were introduced to the system through in-line traps between the manifold and nozzle. Solids were placed in powder form between glass wool plugs within the traps, while liquids were directly applied to the glass wool. Carrier gases were then passed through these traps, to carry vapour to the nozzle. Gas pressures used were typically 3-4 bar, except for cyanogen halides where 1-2 bar was used to promote sublimation due to the low vapour pressures.

2.1.5. Calibration

Calibration of VMI optics relies on the radial distance of signal being proportional to the speed of the ion creating the signal. This proportionality constant is dependent on the ion optics voltages and location of the laser pathway relative to the ion optic plates, as well as inversely proportional to the square root of the ionic mass. In this work, calibration is performed for a specific ion optic voltage and laser position. As such the only variation to note is that of ionic mass (m_i), and the relation between the ionic speed (S) and radial distance (R) is therefore:

$$S = a \cdot \frac{R}{\sqrt{m_i}}$$

Equation 23

In this expression, a denotes a constant for each set of ion optics voltages and laser configuration. This constant can therefore be determined for a system where the distribution of S is known, allowing a new system to be analysed in terms of speed and hence kinetic energy. In this work, we utilised the production of O^+ from O_2 to determine this calibration for work presented in chapters 4 and 5, based on the characterisation of this system by Eppink and Parker.[108] The calibration procedure is shown in Figure 14.

a)

b)

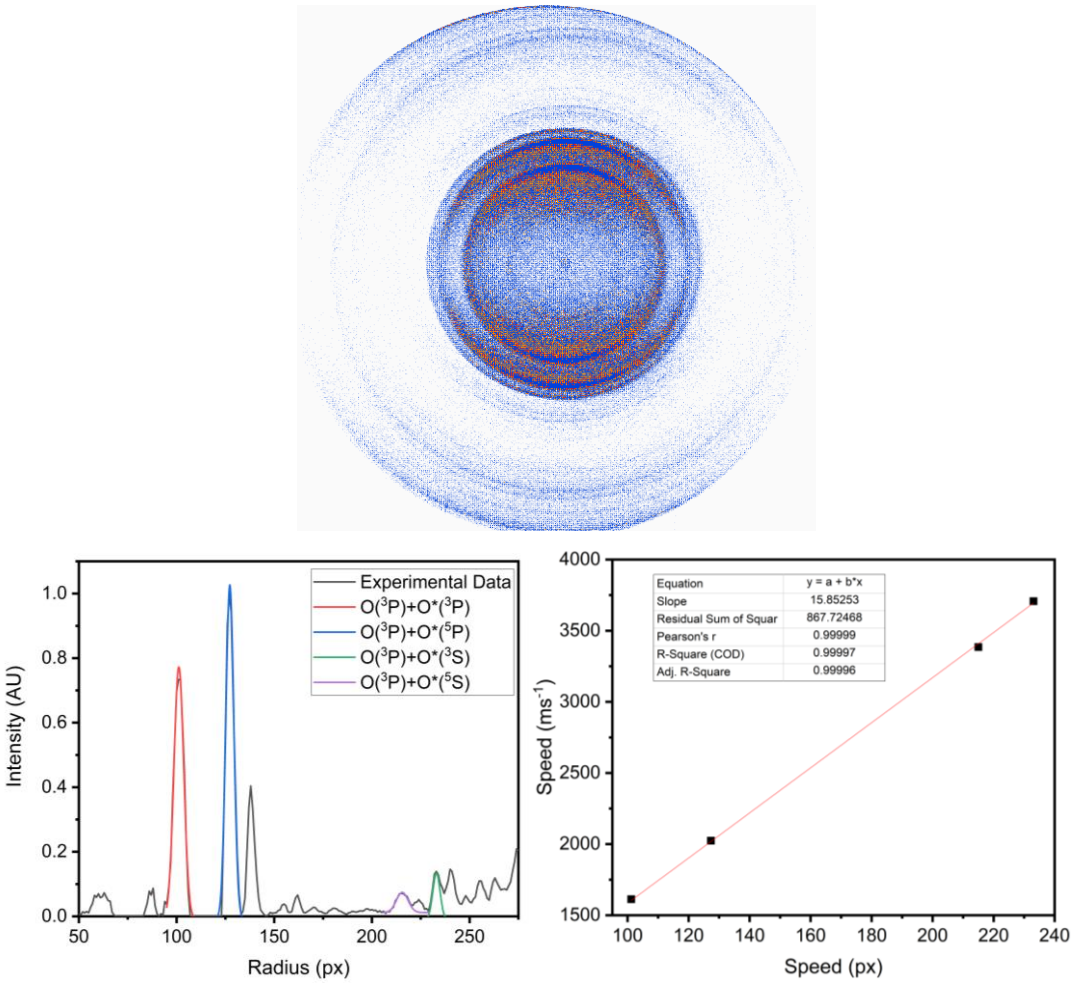

Figure 14: (a) VMI image of O^+ from O_2 at 225 nm, with the laser polarised vertically in the plane of the image. The radial dependence of this image has been analysed in (b). The first graph shows a pBasex fit[80] to the experimental data, along with fits using Origin[109] to 4 key peaks, corresponding to production of $O(^3P)$ atoms alongside O* atoms where an electron is promoted to the 3p level in one of four electronic states. The second graph shows a fit between these peaks and the literature values of the kinetic energy release published by Eppink and Parker.[108] The error is found by repeating this fit at the maximum and minimum peak positions based on adding or subtracting the standard error reported by the Origin peak fit.

2.2. Computational methods

Chapter 3 reports the results of quasi-classical trajectory (QCT) studies for the reaction of chlorine radicals with propene. This work is based on an Empirical Valence Bond (EVB) potential energy surface (PES) previously created by Hornung *et al.*,[51] and interfaced with the VENUS trajectory simulation software.[110] The trajectory outcomes were subsequently analysed through custom written Python and Fortran scripts. The principles of the QCT technique for simulation of reaction dynamics are covered in Chapter 1, with this section covering the details of the implementation.

Early work on molecular dynamics simulations was performed manually by Hirschfelder, Eyring and Topley for the reaction of Hydrogen atoms with Hydrogen molecules, based on a PES previously calculated by Polanyi and Eyring based on London interaction forces.[111] This PES was subsequently used by Wall, Hiller and Mazur to perform computational trajectory simulations, using the speed advantage to perform multiple trajectories that could be averaged to produce a statistical result.[112] Karplus, Porter and Sharma subsequently developed this approach further by initialising the trajectories with quantum state specific rotational and vibrational energy distributions, then allowing the reaction to proceed under classical conditions, creating the quasiclassical trajectory (QCT) approach.[113] More recently binning of the resultant vibrational and rotational energies has become a common step in the analysis. This procedure is frequently implemented via a histogram binning approach (QCT-HB), which is used here, although an alternative Gaussian binning approach (QCT-GB) can give increased accuracy at the cost of requiring a substantially greater number of trajectories.[56] The passive approach to checking zero point energy (ZPE) conservation used here originates in the work of Varandas, where the ZPE of the products is checked against the theoretical ZPE and any trajectories leading to products with energies beneath this level are discarded.[114]

The current work used the QCT-HB approach with Varandas's ZPE check on both products, with the PES based on a fit to *ab initio* points using the EVB model of Warshal and Weiss.[50]

2.2.1. Potential Energy Surface

The potential energy surface used in this work is the most complete ("EVB3") of the three created by Hornung *et al.* in their prior work. These EVB surfaces were created from a fit to an array of *ab initio* points. The key intermediates of 1- and 2-chloropropyl radicals and a π-

adduct of a Cl atom interacting with the propene C=C bond, along with the reactants and products, were geometry optimised using RMP2/6-311G(d,p)[115, 116] calculations, with their energies calculated using the CCSD(T)-F12B/cc-pVDZ-F12 method.[117, 118] A further 300 points at geometries around those of the intermediates were calculated under the same conditions, with the distances between the chlorine atom and each of the sp^2-hybridised carbon atoms kept constant during each geometry optimisation. The direct abstraction pathway, where the Cl atom removes a hydrogen from the sp^3 carbon of propene, underwent geometry optimisation at the B3LYP/6-311G(d,p) level[35] due to failures to converge using RMP2. The calculations were performed using the MOLPRO suite of codes.[119]

The EVB fit parameterised these *ab initio* energy levels using functions representing bond stretching and angle, torsional, and improper torsional bending in the system, along with van der Waals interactions between each atom pair.[51] Bond stretching of the bond r_{ij} between any atoms i and j was fitted to a Morse potential of the form:

$$E(r_{ij}) = D_0\left[1 - \exp\left(-\beta(r_{ij} - r_{ij,0})\right)\right]^2$$

Equation 24

with $r_{ij,0}$ being the equilibrium distance between the atoms, β the force constant and D_0 being the dissociation energy. Bending of the angle θ_{ijk} between any atoms i, j and k was fitted to a quartic function of the difference between θ_{ijk} and the equilibrium angle $\theta_{ijk,0}$ with the force constants below quadratic being set to zero, i.e:

$$E(\theta_{ijk}) = k_2(\theta_{ijk} - \theta_{ijk,0})^2\left[1 + k_3(\theta_{ijk} - \theta_{ijk,0}) + k_4(\theta_{ijk} - \theta_{ijk,0})^2\right]$$

Equation 25

Torsional and improper torsional energy, based on the dihedral angle φ_{ijkl} between atoms i, j, k and l, was fitted to

$$E(\varphi_{ijk}) = \sum_{a=1}^{4} \frac{1}{2} V_a\left[1 - \cos\left(a\varphi_{ijk} - \varphi_{ijk,0}\right)\right]$$

Equation 26

with $\varphi_{ijkl,0}$ as the equilibrium dihedral angle and V_a the barrier height parameters. Van der Waals interaction was modelled as a four parameter Buckingham-Corner function:

$$V(x_{ij}) = \varepsilon\left(\frac{8-2c_6}{\beta-8}exp\left[\beta(1-x_{ij})\right] - c_6 x_{ij}^{-6} - c_8 x_{ij}^{-8}\right)$$

$$x_{ij} = \frac{r_{ij}}{r_{ij,0}} \quad c_8 = \frac{6c_6 + \beta - \beta c_6}{\beta - 8}$$

Equation 27

where ε is the maximum well depth, β is the repulsive force constant and c_6 is an attraction constant. In regions where x_{ij} becomes very small, the attractive term can create an unphysically intense attractive field (known as the "Buckingham Catastrophe"), so when $x_{ij} < 1$ the attractive terms are multiplied by a damping coefficient of $\exp\left[-4(x_{ij}-1)^3\right]$ to prevent this.

2.2.2. Trajectory Simulations

An adapted version of the VENUS trajectory simulation software was used to run the trajectory simulations. Previous work in the Bristol research group enabled the software to interface with the EVB potential energy surfaces,[52] and further modifications were made to output a selection of internal coordinates every 50 time steps. The software uses a combination of fourth-order Runge-Kutta and sixth-order Adams-Moulton methods to numerically integrate the trajectories of the species using classical equations of motion.[110]

The fourth-order Runge-Kutta (RK4) method approximates the velocity change after each time step n of width h as:

$$v_{n+1} = v_n + \frac{1}{6}h(k_1 + 2k_2 + 2k_3 + k_4)$$

Equation 28

In this equation k_1 is the initial velocity gradient. Values k_2 and k_3 are then calculated as the gradient at half the timestep were the gradient to be constant at k_1 and k_2 respectively. The value of k_4 is finally set as the gradient at the end of the timestep, were the gradient to be constant at k_3.[120]

The Adams-Moulton integration works as a predictor-corrector method. The predictor stage suggests a value of v_{n+1} (termed v'_{n+1}), based on a function of v_n through v_{n-4}. This is then corrected by a function of v'_{n+1} along with v_n through v_{n-4}.[121]

In the trajectories reported in this work, the initialisation conditions selected a starting separation of the centres of mass of the chlorine atom and propene at 9 Å. The numerical integration timestep was set at 0.15 fs. The initial collision energies in the centre-of-mass frame were set at either 7, 14, or 28 kJ mol^{-1}, with the propene beginning in the rovibrational ground state.

The orientation of the propene molecule was randomised based on Euler's angles. These are defined based on the principal axes of the molecule (X,Y,Z), those of the reference frame (x,y,z), and a "line of nodes", termed N and defined as the cross product of z and Z. The rotation of the propene is then calculated using three random numbers, R_1 through R_3, by:

$$\theta = \cos^{-1}(2R_1 - 1) \text{ (angle between z and Z)}$$
$$\varphi = 2\pi \cdot R_2 \text{ (angle between x and N)}$$
$$\psi = 2\pi \cdot R_3 \text{ (angle between X and N)}$$

Equation 29

Here, the cosine is used to ensure a uniform distribution at each elevation θ, by making the distribution proportional to the circumference at that elevation (the circumference being proportional to cos(θ)). The impact parameter (b) is sampled up to a maximum value b_{max} of 8 Å using a fourth random number, R_4, by:

$$b = b_{max} \cdot \sqrt{R_4}$$

Equation 30

where the square root is used to ensure a uniform distribution across the area of the circle of radius b_{max}.

Reactive trajectories terminated when the HCl product reached a distance of 5 Å from the allyl radical coproduct, otherwise the trajectories terminated after 1.5×10^7 timesteps (2.25 ns) or if the chlorine atom exceeded 9 Å from the central carbon of the propene molecule. The output reported both the initial propene orientation and impact parameter used for each trajectory, as well as the total, vibrational and rotational energies, along with the scattering angle and trajectory lifetime. This information is alongside the coordinates output every 50 time steps (7.5 fs).

2.2.3. Analysis

Analysis of the trajectory outputs was performed with custom-written Python and Fortran scripts. The analysis of integral and differential cross sections was done by scripts co-written by Dr Hornung and the author of this thesis. The analysis of the stepwise data at each 7.5 fs time interval was done by a script written by the author of this thesis. The details of this analysis are covered in Section 3.3.

3. Computational Studies of the Reaction of Chlorine Atoms with Propene

This chapter is adapted, with permission, from the paper "Collision Energy Dependence of the Competing Mechanisms of Reaction of Chlorine Atoms with Propene", by Frederick J. J. Cascarini, Balázs Hornung, Mitchell S. Quinn, Patrick A. Robertson and Andrew J. Orr-Ewing. This was published in The Journal of Physical Chemistry A, Volume 123, Issue 13, pages 2679-2686. Copyright 2019 American Chemical Society.

Minor changes have been made to formatting including figures, section and reference numbers to suit a thesis structure. I also include a consideration of Suits *et al.*'s discussion of these results in a review paper[122] at the end of section 3.4.4.

Contribution to the work:

This project builds on previous work by Dr Balázs Hornung on the development of a global potential energy surface for the reaction of a Cl atom with propene.[51] All the trajectory calculations and analysis reported in this chapter were carried out by the author of this thesis, with assistance from Dr Balázs Hornung. Co-workers Dr Mitchell S. Quinn and Dr Patrick A. Robertson assisted in the interpretation of the results. The research was conducted under the supervision of Prof. Andrew J. Orr-Ewing.

3.1. Introduction

The photochemically induced reactions of atomic chlorine with volatile organic compounds (VOCs) in the Earth's atmosphere can start sequences of oxidation reactions similar to the pathways initiated by hydroxyl radical reactions.[123] This chlorine-atom chemistry is particularly significant in the marine boundary layer and in coastal regions.[124-127] Of particular interest are reactions with isoprene and higher terpenes, which constitute 30–50% of biogenic VOCs.[128] Unsaturated organic compounds such as these react with chlorine atoms to produce alkyl or alkenyl radicals, which can react further in the atmosphere to form long-chain enols and enones. These oxygen-containing polar organic compounds contribute to the formation of secondary organic aerosols. However, the mechanisms of reactions of alkenes with chlorine atoms are less studied than those of alkanes, which involve direct hydrogen

abstraction pathways to produce alkyl radicals.[52, 129-133] The reactions of Cl atoms with unsaturated VOCs typically exhibit greater mechanistic complexity, with competition between addition and abstraction reactions leading to different outcomes.[134-137] Building on the Bristol group's prior experimental and computational studies of the dynamics of prototypical Cl-atom reactions with alkenes,[51, 137] the current work explores the factors influencing this competition in the first steps of the Cl-atom initiated chain of atmospheric oxidation reactions of unsaturated VOCs.

Propene is the simplest hydrocarbon to contain both sp^2 (C═C) and sp^3 (–CH_3) hybridized carbon atoms, and its reactions with Cl atoms serve as a simpler analogue to reactions of isoprene and terpenes. The reaction with chlorine atoms under low-pressure conditions ultimately produces HCl and the resonance-stabilized allyl radical (CH_2CHCH_2):

$$Cl + CH_3CHCH_2 \rightarrow HCl + CH_2CHCH_2$$

$$\Delta_r H^{\theta}_{298K} = -63.1 \text{ kJ mol}^{-1}$$

Reaction 1

The presence of the alkene functional group introduces the possibility of reaction pathways other than direct H atom abstraction. These more complicated mechanisms include formation of a chloropropyl radical adduct,[138, 139] which can be stabilized at higher pressure by bath–gas collisions, and "roaming" dynamics, in which the chlorine atom becomes temporarily trapped in the potential well created by the π-orbital of the alkene.[137] Roaming dynamics have previously been well characterized for unimolecular reactions such as the photodissociation of formaldehyde (H_2CO)[140-142] and acetaldehyde.[143-146] Clear-cut evidence is rarer in bimolecular reactions, although roaming contributions have been proposed for reaction of Cl atoms with isobutene, which is expected to be mechanistically similar to Reaction 1.[147]

Experimental accounts of the mechanism of Reaction 1 demonstrate variations between reactions performed at high collision energies (for example, using translationally excited Cl atoms from photolysis of a precursor molecule) and at thermal energies. Under the former conditions, velocity map imaging (VMI) experiments suggest direct abstraction dominates,[137] whereas at thermal energies longer-lived intermediates involving addition to the double bond have been argued to increase in significance.[134, 135]

A global potential energy surface (PES) for Reaction 1 was previously developed using an empirical valence bond (EVB) fit to the *ab initio* computed energies of a range of structures of reactants, intermediates, and products.[51] Using this PES, quasi-classical trajectory (QCT) calculations were propagated at collision energies of 28 kJ mol^{-1} to simulate scattering distributions derived from experimental VMI studies.[51] Making further use of this global PES, the current work investigates the impact that collision energy has on the reaction mechanism, with the aim of understanding the apparent mechanistic differences observed in the translationally hot and thermal regimes. In particular, the studies reported here include investigation of the relative significance of direct abstraction and addition–elimination mechanisms at a range of collision energies, and seek evidence for the previously proposed roaming type dynamics.

3.2. Computational Details

Trajectory simulations were computed using a global EVB PES for Reaction 1. This PES, and the methods used to create it, have been described in detail previously;[51] as such, only a brief discussion is included here.

The prior work by Hornung et al.[51] developed three EVB-fitted PESs for Reaction 1 to unravel the contributions of various features on the multidimensional energy landscape to the product scattering and internal energy distributions. The current work uses the most complete of these PESs, labelled as EVB3 in ref 51. This EVB surface was fitted to ab initio points calculated using CCSD(T)-F12B/cc-pVDZ-F12 energies for a wide range of possible structures sampled in all degrees of freedom. The structures were optimized using RMP2/6-311G(d,p) calculations, except for the hydrogen abstraction channel where difficulties in convergence necessitated use of the B3LYP/6-311G(d,p) level of theory. The EVB model was then used to fit the parameters of an EVB matrix, defined in ref 51, to a set of 1000 of these ab initio points. The outcomes of QCT calculations on this EVB-fitted PES at a collision energy of 28 kJ mol^{-1} were previously compared with experimental data and found to give satisfactory agreement.

Two slices through the global EVB PES of particular significance for the reaction dynamics are depicted in Figure 15. The upper plot shows the locations of the two potential energy wells corresponding to the 1- and 2-chloropropyl addition complexes (shown in blue/black), as well

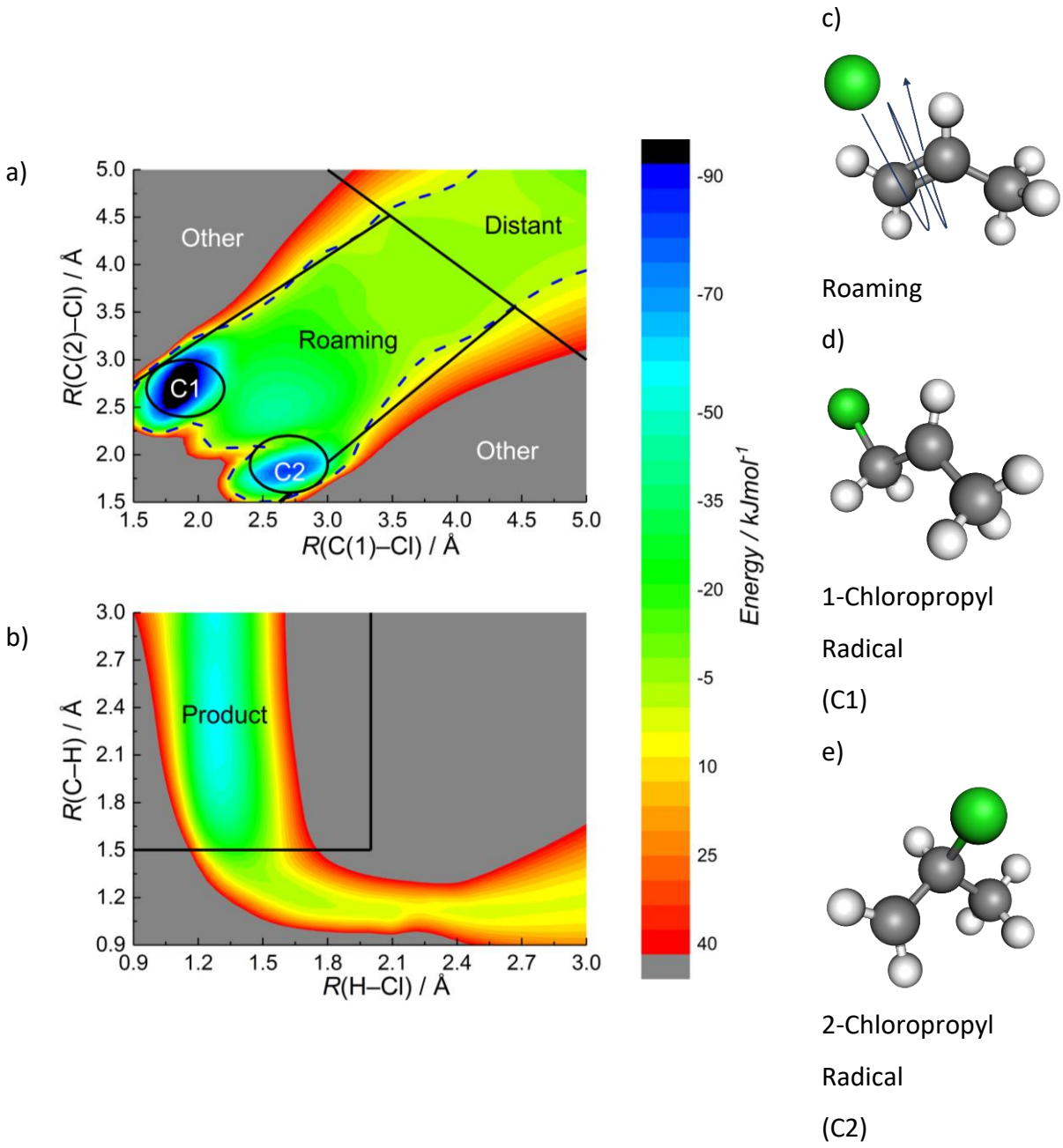

Figure 15: Depictions of two 2-dimensional slices through the global EVB PES previously reported by Hornung et al.[51] In (a), the PES is plotted based on relaxed scans at fixed distances of the Cl atom from the terminal and central C atoms in the C═C bond, C(1) and C(2). In (b), the fixed coordinates used are the distance of the Cl from a methyl-group H atom, and the same H atom's distance from the methyl group carbon. The overlaid lines demark areas of the PES used to classify reaction trajectory types, as explained in Table 2. The C1 and C2 labels in (a) identify the 1-chloropropyl and the 2-chloropropyl radical addition complexes, respectively. The dotted line in (a) depicts the energy contour at 0 kJ mol^{-1}, which guided our choice of conditions for a roaming assignment. Insets (c), (d) and (e) depict schematically a possible roaming state, and 1- and 2-chloropropyl radical structures.

as the region in which a chlorine atom interacts more loosely with the π-electron system of the alkene (the green area appearing diagonally across the image).

The EVB PES was interfaced with the VENUS program, which was used to propagate classical trajectories over the surface.[110] The starting separation of the centres of mass of the chlorine atom and propene was selected to be 9 Å, with impact parameters randomly sampled at values up to 8 Å, and with random initial orientation of the propene molecule. Reactive trajectories terminated when the HCl product reached a distance of 5 Å from the allyl radical coproduct. All trajectories were propagated with a time step of 0.150 fs. Batches of trajectories were initiated with initial collision energies in the centre-of-mass frame of either 7, 14, or 28 kJ mol^{-1}. 7 and 28 kJ mol^{-1} were selected to be representative of experimental thermal and hyperthermal conditions respectively,[134-138] with 14 kJ mol^{-1} chosen as an intermediate value. A breakdown of the numbers of trajectories analysed is provided below.

The outputs from the trajectory simulations were used to compute distributions of populations of the quantum states of the HCl product, the internal energies of the allyl radical coproduct, and scattering angles, as well as opacity functions (describing the probability of reaction at different impact parameters) and reaction times. In addition, selected internal coordinates were recorded every 50th time step, corresponding to a temporal spacing of 7.5 fs.

3.3. Analysis

Analysis of completed trajectories used custom-written Python and Fortran scripts. The analysis process first considered the internal energy of the products of Reaction 1, discarding any trajectories for which the internal energy of either species was below its vibrational zero-point energy. Trajectories that satisfied this check were then classified by whether they ended with a hydrogen atom bonded to the chlorine (reactive trajectories), or with the reactants re-forming (unreactive trajectories). The reactive trajectories were further processed by assigning vibrational and rotational quantum states to the HCl using a histogram binning algorithm. Differential cross sections (DCS) were then extracted by fitting the distribution of scattering angles (across all product states) to a sum of Legendre polynomials up to fourth order. Error bars were calculated for the DCS and opacity functions using a bootstrapping process.[148] This process was based on 1000 data sets randomly sampled with replacement

from the original data set. The results were used to generate the 95% pointwise confidence interval, which is shown in the corresponding figures. The error bars computed for the vibrational and rotational distributions also represent 95% confidence intervals, based on a margin of error approximated by $N^{-1/2}$.

Mechanisms of reaction were assigned by analysing the internal coordinates of trajectories at each propagation step using the definitions listed in Table 2. These defined regions classified the reactive trajectories according to the states identified by Hornung *et al.*:[51] the transient formation of energized 1- or 2-chloropropyl radical intermediates; a roaming state; the chlorine atom distant from the propene; reaction products. The assignment tests were performed in the order they are presented in Table 2, with subsequent criteria only being checked if all prior tests were returned as false.

assignment	**definition**
products	R(Cl–H) < 2 Å
	R(C(3)–H) > 1.5 Å
distant	R(C(1)–Cl) + R(C(2)–Cl) > 8 Å
1-chloropropyl radical	(R(C(1)–Cl) – 1.9 Å)^2 + (R(C(2)–Cl) – 2.7 Å)^2 ≤ 0.09 Å^2
2-chloropropyl radical	(R(C(1)–Cl) – 2.7 Å)^2 + (R(C(2)–Cl) – 1.9 Å)^2 ≤ 0.09 Å^2
roaming region	1.13 × R(C(1)–Cl) – 1.47 Å ≤ R(C(2)–Cl) ≤ 0.89 × R(C(1)–Cl) + 1.42 Å
other	a situation that does not satisfy any condition listed above.

Table 2: Categories and Their Definitions Used for Assignment of Trajectories

The definitions listed in Table 2 are based on the identification of different regions of the multidimensional EVB PES, as illustrated in Figure 15. The work presented here concentrates in large part on the minority indirect pathways: complex-mediated reactions involve addition to one or other C atom of the double bond to form 1- or 2-chloropropyl radicals transiently before HCl elimination, whereas weaker interactions with the π-electron density of the double bond might result in roaming trajectories across a broad and energetically flat region of the PES. These pathways are not mutually exclusive, because elimination of HCl from an energized chloropropyl radical might involve some degree of roaming dynamics.[147]

The regions corresponding to the two isomers of the chloropropyl radical are visible as deep potential wells in the depiction of the PES in Figure 15a. Each such assignment is characterized by an elliptical boundary around the appropriate PE well. Assignment of a roaming state is more complicated. This work assigns only an upper limit to the contribution from roaming trajectories by counting those in which the chlorine atom interacts transiently with the π-electron system, with the corresponding weakly attractive region of the PES demarcated in Figure 15a and defined numerically in Table 2. The set of trajectory steps identified by this method is a superset of all the trajectories that would satisfy a more precise definition of roaming.[149, 150] The quantitative bounds of this assignment were set by linear fits of the coordinates of Figure 15a to the 0 kJ mol^{-1} PE contour line of the EVB PES.

3.4. Results and Discussion

The analysed outcomes for batches of successful quasi-classical trajectories are reported here as populations of HCl quantum states, opacity functions, reaction times, scattering angle distributions, and classifications of reaction mechanisms. The total numbers of computed trajectories that successfully terminated in the allocated computer time, as either reactive or unreactive, were 64 695 at a collision energy of 7 kJ mol^{-1}, 134 884 at 14 kJ mol^{-1}, and 109 894 at 28 kJ mol^{-1}. Of these sets of trajectories, 3756, 5848, and 4419 respectively resulted in HCl and allyl radical products. Subsequent checks identified 1772, 2893, and 2252 trajectories at 7, 14, and 28 kJ mol^{-1} collision energies which satisfied our condition of HCl and allyl radical internal energies greater than the zero-point vibrational energies of the two products. Only these final groups of trajectories were retained for further analysis.

3.4.1. Product HCl Quantum State Populations

Figure 16 depicts the populations of rotational and vibrational levels of the HCl products at each of the three collision energies studied, normalized by dividing the population in each state by the total population. These population distributions reflect the outcomes of both direct and indirect reaction pathways and show little or no dependence on the collision energy. This insensitivity to collision energy can be understood if the trajectories sample similar transition state geometries for the H-atom abstraction step in the reaction, regardless of the collision energy and the preceding mechanism to reach the transition state. This result supports the conclusion drawn by Hornung et al.,[51] using reduced forms of the global EVB

a)

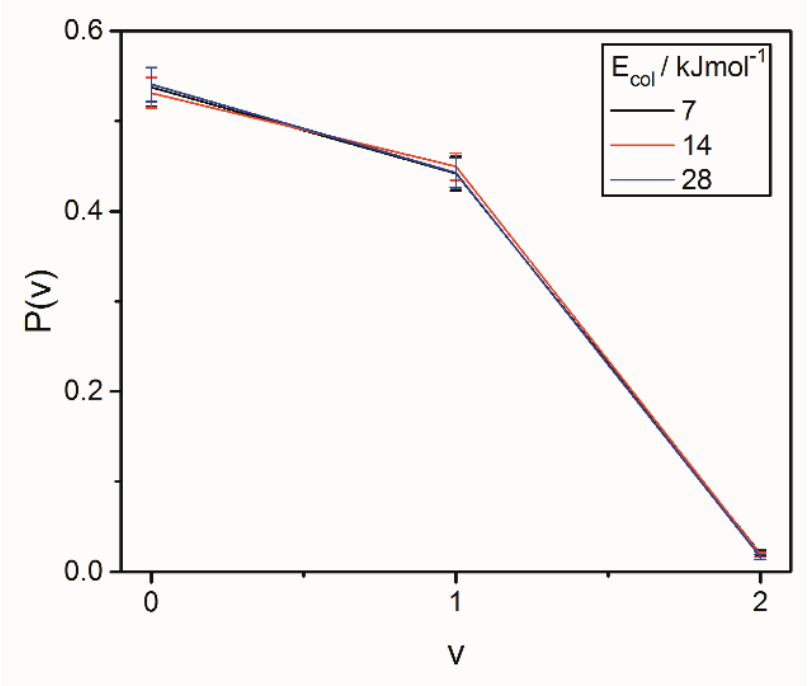

b)

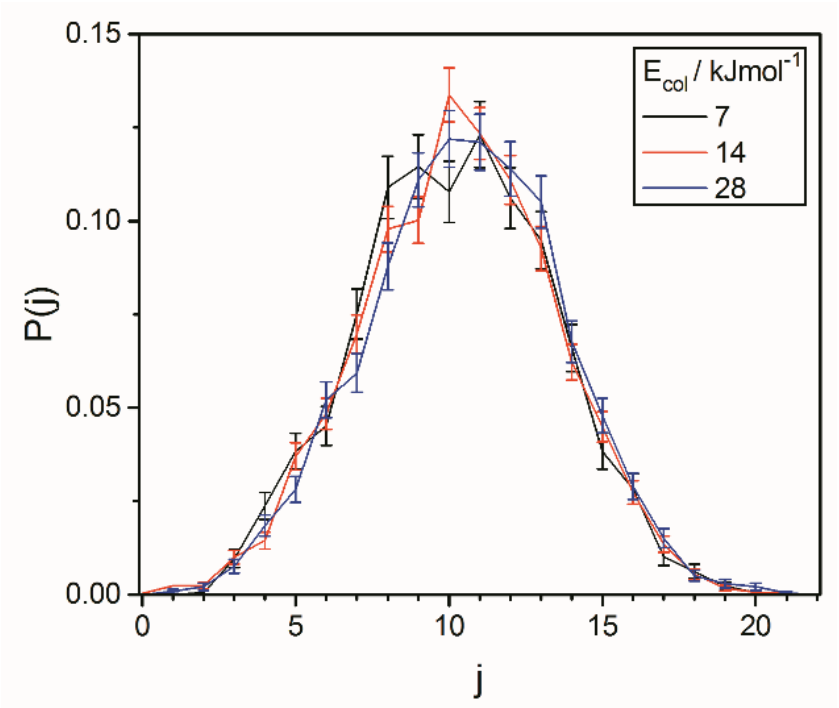

Figure 16: Simulated (a) vibrational and (b) rotational level populations of the HCl products of Reaction 1 at three different collision energies. The labels v and j denote the vibrational and rotational quantum numbers of the HCl, respectively. The distributions were deduced from the outcomes of classical trajectories propagated on the EVB PES described in the text and illustrated in Figure 15, with initial collision energies of 7 kJ mol^{-1} (black), 14 kJ mol^{-1} (red), or 28 kJ mol^{-1} (blue). They have been normalized such that the sum of all the populations is unity for a given data set.

PES, that the populations of rotational and vibrational states are controlled by a transition state for H-abstraction, which is sampled by both direct and indirect routes, and the shape of the exit valley from the transition state to products. Specifically, the quantum state population distributions computed using a restricted PES allowing only the direct abstraction pathway were the same as those computed using the full EVB PES incorporating 1- and 2-chloropropyl radical complex formation and interactions with the π-electron cloud of the C═C bond. The current work extends the conclusions from the prior study by demonstrating that, even with the full topography of the global EVB PES available for dynamical exploration, the collision energy of the reaction has a negligible impact on the final HCl product quantum state population distribution. Below, it is shown that the collision energy does impact on the proportion of long-lived intermediates sampled by the trajectories, but these competitive indirect and direct pathways to reach the H-abstraction transition state do not ultimately influence the product state population distributions.

3.4.2. Impact Parameter and Reaction Time

Opacity functions plotted in Figure 17 depict the dependence of reaction probability on the initial impact parameter. They are normalized such that the corresponding distributions expressed in terms of the reduced impact parameter (Equation 31) integrate to unity.[9]

$$b_{red} = \frac{2b^2}{b_{max}^2} - 1$$

Equation 31

The plots show enhanced reactivity at higher impact parameters for lower collision energies, which is consistent with long-range attractive and barrierless interactions drawing the reactants together more effectively when the collision energy is smaller.

The plots in Figure 18 explore this behaviour further by displaying how the computed trends in reaction time depend on impact parameter for the three different choices of collision energies. The behaviour for reactive and unreactive trajectories is also compared. The plots reveal some of the consequences of changing collision energy on the reaction dynamics and mechanisms.

It is useful to compare the trajectory time distributions for unreactive trajectories to those expected for simple bypassing trajectories in which the chlorine passes the propene molecule

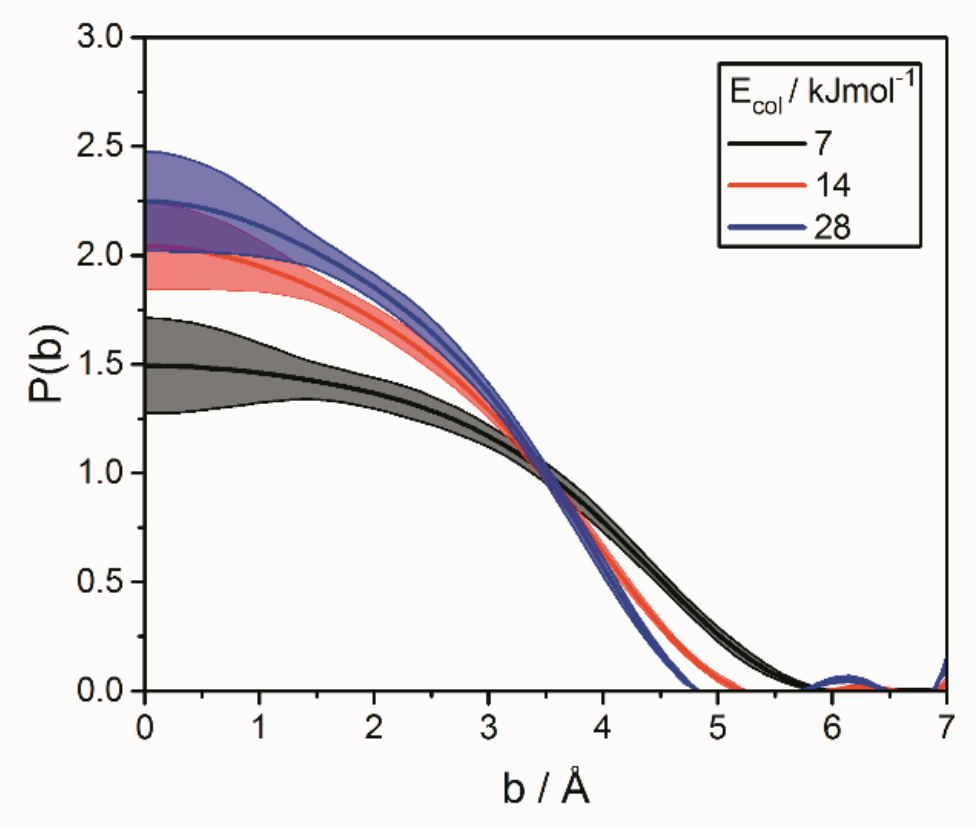

Figure 17: Dependence of reaction probability on the initial impact parameter, *b*. Computed opacity functions, *P*(*b*) are shown for the three collision energies studied, with the inset key defining the colour scheme used. Solid lines are the computed distributions, with the shaded surrounding areas showing uncertainties at the 95% confidence level.

without any intermolecular interactions. The dependence of this bypass time on impact parameter is depicted by the black lines plotted in the panels in Figure 18. This time scale is reduced at high impact parameters because of the spherical initialization and termination conditions of the trajectory simulation, which are defined for the chlorine being a certain radius from the centre of the propene molecule. As such, the distance between the initialization and termination locations in the event of no interaction between the two species reduces at higher impact parameters, because the distance across a sphere centred at the propene centre of mass decreases.

Unreactive trajectories closely follow the model bypass trajectory timings, especially at higher collision energies, with only the lowest collision energy data set showing any significant deviation. In contrast, reactive trajectories frequently exhibit timings faster than would be expected of a bypass trajectory. This behaviour is attributed to acceleration caused by attractive interactions between the Cl atom and the propene molecule during the direct

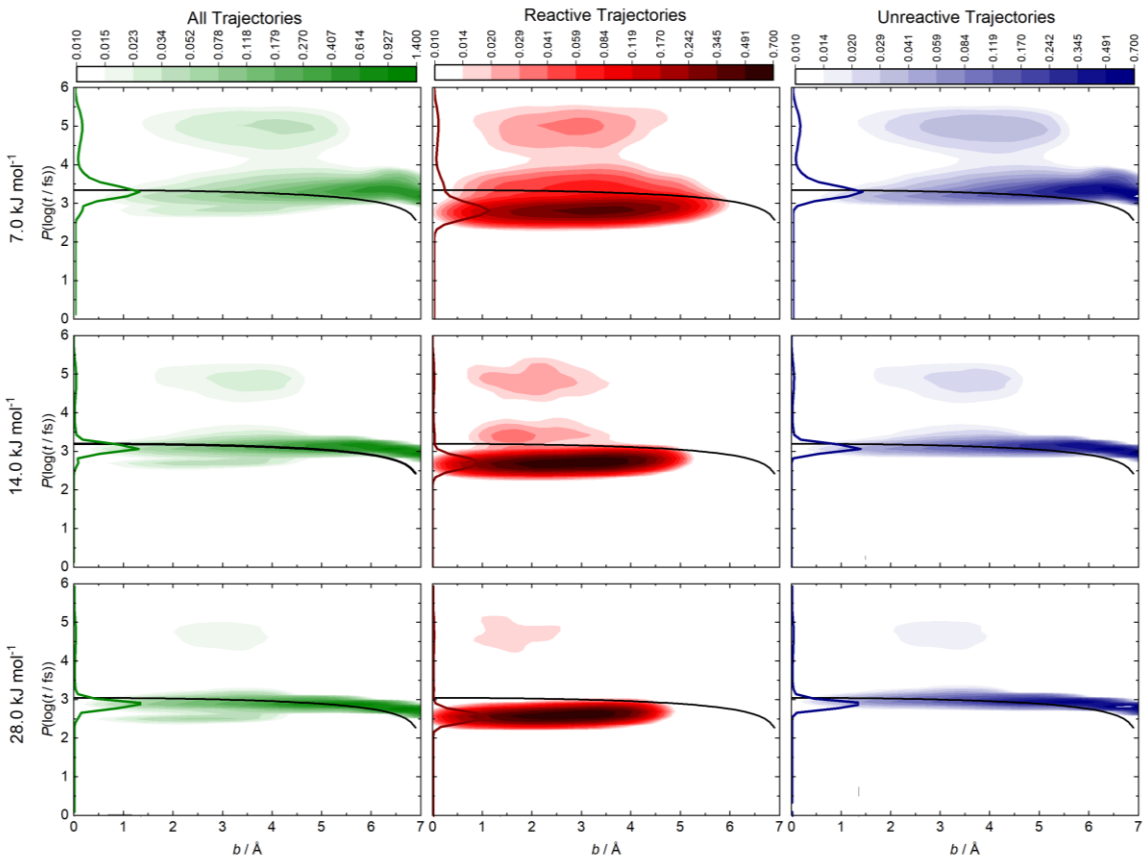

Figure 18: Depictions of the dependence of trajectory durations (plotted as the base-10 logarithms of trajectory completion times) on initial impact parameter, for the three collision energies studied. The three columns classify the trajectories as unreactive (right), reactive (centre), and the sum of reactive and unreactive outcomes (left). Trajectory outcomes are shown by colour maps, which use a base-10 logarithmic scaling to highlight the long-lived features and are compared to the time scale for bypass of a propene molecule by a Cl atom with the same starting collision energy and a range of impact parameters (black solid lines). The functions plotted alongside the ordinates depict kernel density estimations of the trajectory outcomes as a function of time, in arbitrary units.

abstraction trajectories which dominate the reactivity. Moreover, apportioning some of the exothermicity of reaction to product translation can increase the kinetic energy of the products compared to reactants.

At the higher collision energies of 14 and 28 kJ mol^{-1}, trajectory completion times close to the bypass time scale dominate for both reactive and unreactive data sets. For reactive collisions, 93% (28 kJ mol^{-1} collision energy) and 86% (14 kJ mol^{-1} collision energy) of these trajectories are best characterized as direct abstraction of a hydrogen atom from the methyl group of propene. At the 7 kJ mol^{-1} collision energy, 70% of reactive trajectories are direct, and a secondary peak in the distribution of reaction times becomes more prominent at longer delays. This alternative scattering behaviour is evidence of long-lived intermediates. Its

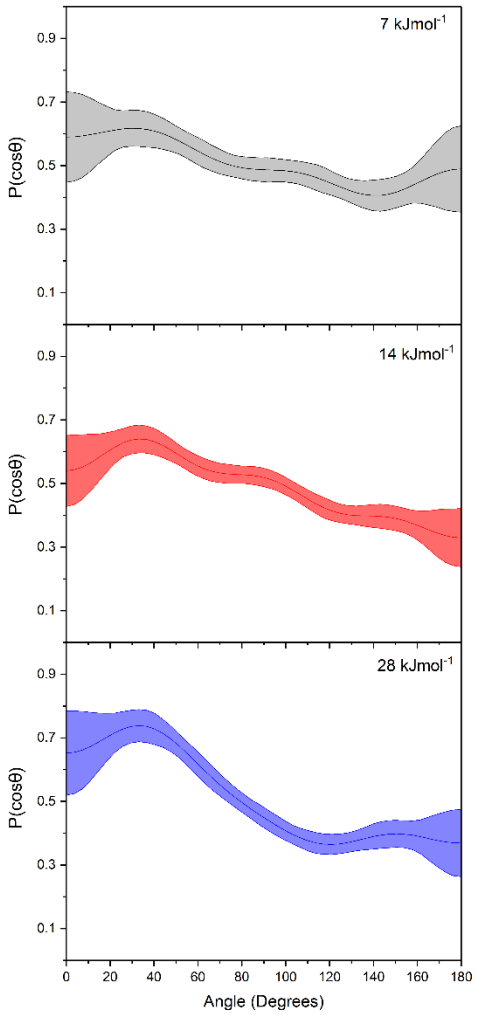

Figure 19: Computed distributions (solid lines) of product HCl scattering angles, defined with respect to the relative velocity of the Cl-atom. The distributions are shown for three collision energies; 7 kJ mol^{-1} (top, black), 14 kJ mol^{-1} (middle, red), and 28 kJ mol^{-1} (bottom, blue), and are summed over all product HCl vibrational and rotational quantum states. The distributions are calculated as a normalized fit of the cosine of the scattering angle to a sum of Legendre polynomials. The order of the Legendre expansion has been selected independently at each energy through a minimization of the statistical risk. The shaded areas depict the 95% confidence interval of the mean.

presence in the analysis of both reactive and unreactive trajectories demonstrates that the participation of these long-lived states does not preclude either dissociation back into the reactants or progression on to the reactive transition state. The likely cause is a contribution from energized 1- or 2-chloropropyl addition complexes, and perhaps also roaming dynamics. These possibilities are explored further in Section 3.4.4.

3.4.3. Scattering Angle Distributions

Fitted distributions of HCl scattering angles, summed over all vibrational and rotational quantum states, are plotted in Figure 19 for the three collision energies. At the higher collision energies, most products are forward scattered, although a broad distribution is characteristic of facile abstraction of an H-atom from an sp^3-hybridized carbon atom.[52, 132, 133, 147, 151-153] However, the scattering angle distributions becomes increasingly isotropic at lower collision energies, supporting the findings reported in Section 3.4.2 of the growing importance of long-lived intermediates, and possible steering of Cl-atom approach directions by long-range attractive forces. The plots in Figure 18 indicate that these complexes survive for time scales of 10^4–10^5 fs, which exceed the rotational period of the energized chloropropyl radicals.

3.4.4. Trajectory Assignments

As was noted in Section 3.4.2, most of the reactive trajectories at the three collision energies considered involve direct abstraction of an H-atom. Here, the focus is put on the minority of indirect trajectories, which show more complicated reaction dynamics. The contribution to reaction by indirect pathways involving long-lived addition complexes is confirmed by further examination of the stepwise progression of the reactive trajectories. This analysis was performed on a set of 1308 trajectories at 7 kJ mol^{-1}, 2535 at 14 kJ mol^{-1}, and 4527 at 28 kJ mol^{-1}. After the first few picoseconds of product build-up, which are dominated by direct abstraction reactions, quantitative analysis of the remaining incomplete trajectories shows that the 1-chloropropyl radical is strongly favoured: more than 80% of the delayed trajectories exist as this intermediate at any single time step. This preference is shown in Figure 20, which displays the proportions of trajectories assigned to the categories listed in Table 2 at each time step.

Focusing on the indirect trajectories after direct reactions have completed, Figure 20 shows that the relative proportion of each assignment type remains largely invariant over time. Although the long-lived trajectories become more important as a proportion of all reactive trajectories at lower collision energies (reactive trajectories lasting longer than 1.5 ps increase from 7% at 28 kJ mol^{-1} to 30% at 7 kJ mol^{-1}), the balance of types of these long-lived trajectories does not change.

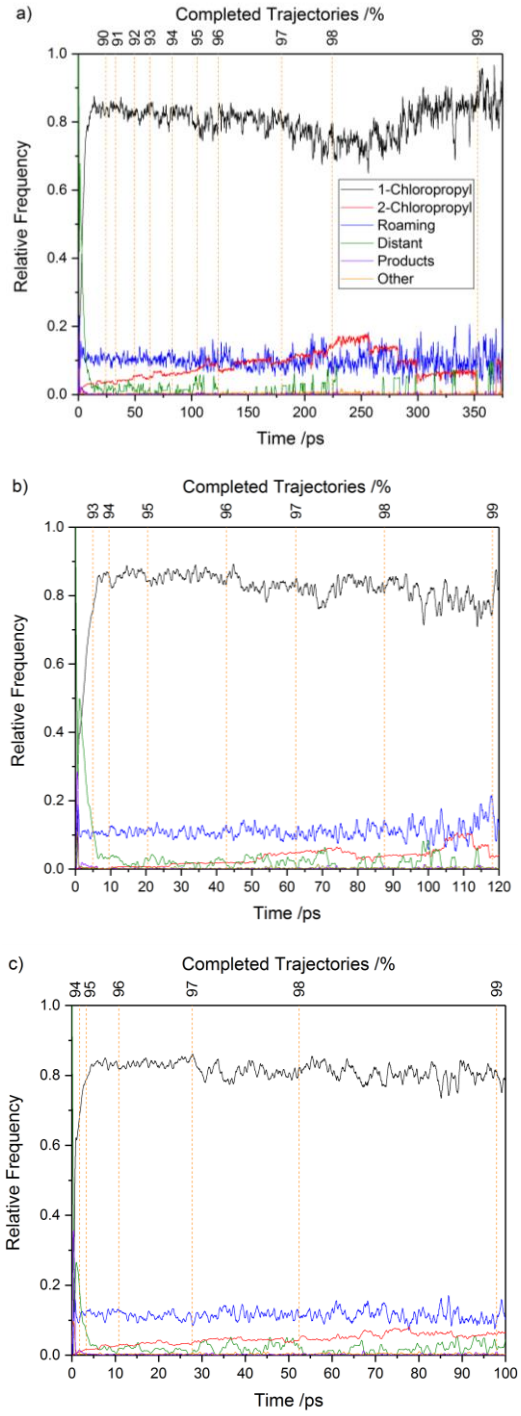

Figure 20: Proportion of incomplete reactive trajectories assigned to intermediates corresponding to different regions of the PES at each time step. The inset key provides the colour codes for the different intermediates. The plots show the outcomes for ensembles of trajectories propagated at initial collision energies of (a) 7 kJ mol^{-1}, (b) 14 kJ mol^{-1}, and (c) 28 kJ mol^{-1}. The top axis in each plot depicts the percentages of trajectories that have completed at given timesteps. The data were smoothed using a second-order Savitzky–Golay filter with a 0.9975 ps width. The graphs are curtailed shortly beyond 99% completion of trajectories.

	percentage of time		
trajectory type	7 kJ mol^{-1}	14 kJ mol^{-1}	28 kJ mol^{-1}
1-chloropropyl	78.2%	81.6%	80.1%
2-chloropropyl	7.0%	2.5%	4.9%
roaming*	10.2%	10.8%	11.5%
distant	4.1%	4.6%	2.9%
products	0.2%	0.2%	0.2%
other	0.3%	0.3%	0.4%

Table 3: Proportions of Time Spent by Indirect Reactive Trajectories in Each Assignment

*See main text for further discussion.

There is a clear preference for formation of the 1-chloropropyl radical intermediate over the 2-chloropropyl radical at all collision energies. This observation agrees with experimental measurements by Lee and Rowland, who reported measured branching ratios of 1-chloropropyl to 2-chloropropyl radicals that varied from 6.6 ± 0.1 to 12.3 ± 0.1, depending on the partial pressures of the reactants.[138] To compare with these experimental values, the ratio of the total time spent by all reactive trajectories as these two different isomers of the chloropropyl radical was calculated. This analysis yields 1-chloropropyl to 2-chloropropyl radical ratios of 16 at 28 kJ mol^{-1} and 11 at 7 kJ mol^{-1}. At 14 kJ mol^{-1}, a larger number of trajectories were propagated, giving a total of 17 897 reactive trajectories, to test the consistency of these ratios. A bootstrapping analysis of these trajectory outcomes using 1000 samples produced a mean ratio of 23 ± 7 at the 95% confidence interval. When this uncertainty is applied to the 7 kJ mol^{-1} calculations, the computed values overlap the experimental ratios reported by Lee and Rowland. The calculations indicate that the 1-chloropropyl radical is consistently favoured over the 2-chloropropyl radical for the range of collision energies studied, despite the 2-chloropropyl radical potential well being deeper by 10.5 kJ mol^{-1} (-102.9 kJ mol^{-1} relative to the reactants, compared with -92.4 kJ mol^{-1} for 1-chloropropyl).

A more complete analysis of the trajectories that continue beyond 1 ps, before forming HCl + allyl radical products, provides the classification ratios reported in Table 3. These values demonstrate that the 1 chloropropyl structure is sampled for more than three-quarters of the duration of these indirect reactive trajectories. Notwithstanding the lenient definition of

roaming structures in this study, only around a tenth of the total time of propagation of the indirect trajectories is found to be spent in a roaming assignment.

Further analysis shows that a significant amount of these roaming assignments involved fast (few femtoseconds) excursions from the 1-chloropropyl assignment. This behaviour suggests excess internal energy in the 1-chloropropyl radical occasionally localizes sufficiently in a C–Cl bond to induce large-amplitude vibrational motion in the trajectory. To study this effect further, 211 long-lived (>1.5 ps) reactive trajectories at a collision energy of 7 kJ mol^{-1} were randomly selected. The assignments of these trajectories were then modified such that any set of roaming assignments in adjacent 7.5 fs time bins that did not span at least 10 time bins (i.e., 75 fs), was changed to the assignment immediately following the set. The basis for this reassignment was that roaming dynamics are mechanistically distinct from single oscillations of large-amplitude vibrational motions extending beyond the PES regions defined as 1- or 2-chloropropyl in our analysis (Table 2). This procedure reduced the roaming assignment proportion to 2.5% of the total time.

Following the publication of this work, Suits *et al.* have discussed this finding of minimal roaming in a review paper.[122] Concern is expressed at the minimum time boundary of 75 fs, due to roaming in the photodissociation of formaldehyde being observed over time periods averaging 70 fs. However, this difference between hydrogen and chlorine roaming can be explained by the differences in mass of the two atoms. The impact of changing the nature of the atom can be demonstrated by considering a key motif in roaming reactions: the revolution of one species about the π system of a C=C bond. If the entirety of the highest collision energy studied in the present work, 28 kJ mol^{-1}, remained in the kinetic energy of the Cl atom, then for one orbit around a bond to take 75 fs the orbital radius would need to be around 15 pm. This radius is less than a tenth of the van der Waals radius of the chlorine atom.[154] As such, I argue no roaming can take place by a chlorine atom in a period less than 75 fs with a collision energy of 28 kJ mol^{-1}, since it would be unable to complete a fraction of the orbit in this time. By contrast, the orbital radius under the same conditions for a hydrogen atom would be around 90 pm, ¾ of the van der Waals radius of hydrogen. In combination with the higher amounts of energy in formaldehyde dissociation studies, due to the activation energy for the pathway being around 343 kJ mol^{-1},[155] it is then entirely possible that a hydrogen atom could complete a full rotation at a reasonable distance within 70 fs.

3.5. Conclusions

The exothermic reaction of Cl atoms with propene to make HCl serves as a benchmark system to understand the dynamics of Cl-atom reactions with unsaturated hydrocarbons. Quasi-classical trajectory calculations using a full-dimensionality PES developed previously by Hornung et al., are used to explore the collision energy dependence of the reaction dynamics. Direct abstraction of an H-atom from the terminal methyl group of the propene, with reaction complete within 1 ps, is the dominant pathway at the three collision energies studied (70% of reactive trajectories at 7 kJ mol^{-1}, 86% at 14 kJ mol^{-1}, and 93% at 28 kJ mol^{-1}) but the minor contribution of indirect pathways increases as the collision energy decreases. The regions of the global PES sampled by these indirect pathways are classified as energized 1-chloropropyl radical and 2-chloropropyl radical adducts, or roaming-encounter and distant-encounter complexes (the latter arguably corresponding to long-range roaming dynamics). At all three collision energies studied, the indirect trajectories spend approximately 80% of their time sampling the 1-chloropropyl radical PE well, and less than 10% in the vicinity of the 2-chloropropyl PE well. The trajectories sampled the roaming potential energy region for ~10% of their time. However, significant amounts of this time arise from high frequency motion across our chosen boundary between the 1-chloropropyl radical state and the roaming region. When these motions are reclassified as large-amplitude vibrations of the energized chloropropyl radicals, the roaming proportion reduces dramatically. The calculations demonstrate that distributions of product HCl populations among vibrational and rotational levels are insensitive to the initial collision energy, but that the range of impact parameters leading to successful reaction widens at lower collision energies. This effect, and the small increase in propensity for indirect dynamics, cause more isotropic scattering of the products in the centre-of-mass frame as the collision energy decreases. The results go some way to bridge the gap between molecular beam studies of the dynamics of the Cl + propene reaction at elevated collision energies and the studies of reaction rate coefficients, product HCl vibrational excitation, and trapping of 1- and 2-chloropropyl radical intermediates performed under thermalized conditions. The QCT analysis provides new insights for the likely mechanisms of reactions of Cl atoms with various unsaturated VOCs of natural and anthropogenic origins in the troposphere.

4. Photodissociation of 2,4-dibromofluorobenzene at 260 – 285 nm

Contribution to the Work

Dr Mitchell S. Quinn designed the experimental apparatus, and he and the author of this thesis worked together on its construction, testing and characterisation. The data collection and analysis was performed by the author of this thesis, with assistance from Dr Mitchell S. Quinn and Dr Patrick A. Robertson. The work was completed under the supervision of Prof Andrew J. Orr-Ewing.

4.1. Introduction

The photochemistry of both alkyl and aryl halides has been widely studied,[156,157] motivated by these species serving as exemplars for nσ* and πσ* bond dissociation pathways and ππ* excitation.[158-160] Beyond this, alkyl and aryl halides are common environmental pollutants,[161-163] so understanding their photochemistry is beneficial for assessment of their atmospheric impacts.

Photoexcited alkyl halides typically dissociate through halide (X) lone pair donation into the anti-bonding orbital of the C-X bond (n → σ*).[164] Aryl halide dissociation instead introduces pathways via a range of π* electronic states leading to more complex dynamics.[158, 165] These extra pathways result in key distinctions between the dynamics of each; in particular, longer dissociation timescales arise, and transition dipole moments are based on the aryl π system rather than the C-X bond. The initially photoexcited singlet ππ* states then cross over into triplet states with σ* character, resulting in the dissociation of the C-X bond.[166] This intersystem crossing (ISC) is influenced by the molecule's symmetry, making the process dependent on the aryl substitution pattern. For example, ortho- and meta- substituted aryl halides with two different halogen substituents may undergo ISC more readily than para-substituted aryl halides because of their lower symmetry.[167] Out-of-plane bending of the C-X bond due to the π π* excitation further lowers the symmetry, potentially down to C_1, and also promotes ISC.[168]

In the case of bromine and iodine, the large spin-orbit interaction also becomes a significant factor. This spin-orbit coupling may mediate the ISC process, hastening the bond dissociation,[166] although it has been suggested computationally that this has only a very small impact in bromofluorobenzenes.[169] The spin-orbit coupling is also sufficient for the ground ($J = {}^3/_2$) and excited ($J = {}^1/_2$) spin-orbit states of the fragment Br or I atoms to be easily distinguished via REMPI detection methods, and the independent detection of the two states can provide valuable information about the non-adiabatic photodissociation dynamics.[158, 170]

Aryl monohalides and dihalides have been widely studied, at both nanosecond[158, 165, 171-173] and ultrafast[167, 174-176] time resolution. A variety of polyhalides have also been examined, with an area of particular interest being in the impact of fluorination in promoting aryl ring torsion and altering bond strengths.[166, 167, 177-180] However, there is only limited prior work on 2,4-dibromofluorobenzene (DBFB). These prior studies characterised the near-UV[93] and IR[94] spectra of this and selected similar species. The UV spectrum observed and characterised 32 vibronic transitions in the 285-265 nm wavelength region based on the purely electronic transition at 35 510 cm^{-1} (281.61 nm), which is the region the current work also covers. The IR spectrum revealed 45 bands in the 250-4000 cm^{-1} region. Of particular interest are a pair of ground state features at 610 and 500 cm^{-1} assigned to modes involving a carbon-bromine bond. The former vibrational mode is reported to have a corresponding wavenumber in the UV-excited state of 714 cm^{-1}.

The dissociation pathways that DBFB follows might be expected to be similar to those of the simpler monobromofluorobenzenes. However, contrasting descriptions of the details of these species' dissociation pathways can be found in the prior literature. Three main computational studies producing excited-state potential energy surfaces (PESs) have been reported for monobromofluorobenzenes, by Gu *et al.*, Borg *et al.* and Li *et al.* with relevance for the absorption at wavelengths around 266 nm.

Gu *et al.* studied m- and p-bromofluorobenzene at the CIS/6-31G*[181, 182] level of theory, in combination with photofragment spectroscopy studies using a rotatable detector located after a Time of Flight – Mass Spectrometry (TOF-MS) apparatus to determine the angular distribution.[177] In Gu *et al.*'s work, dissociation was assigned to a single pathway involving initial excitation to a $\pi\pi^*$ S_1 state. This excitation was followed by ISC to a high-lying vibrational energy level of a quasi-bound triplet state, with passage over the barrier leading

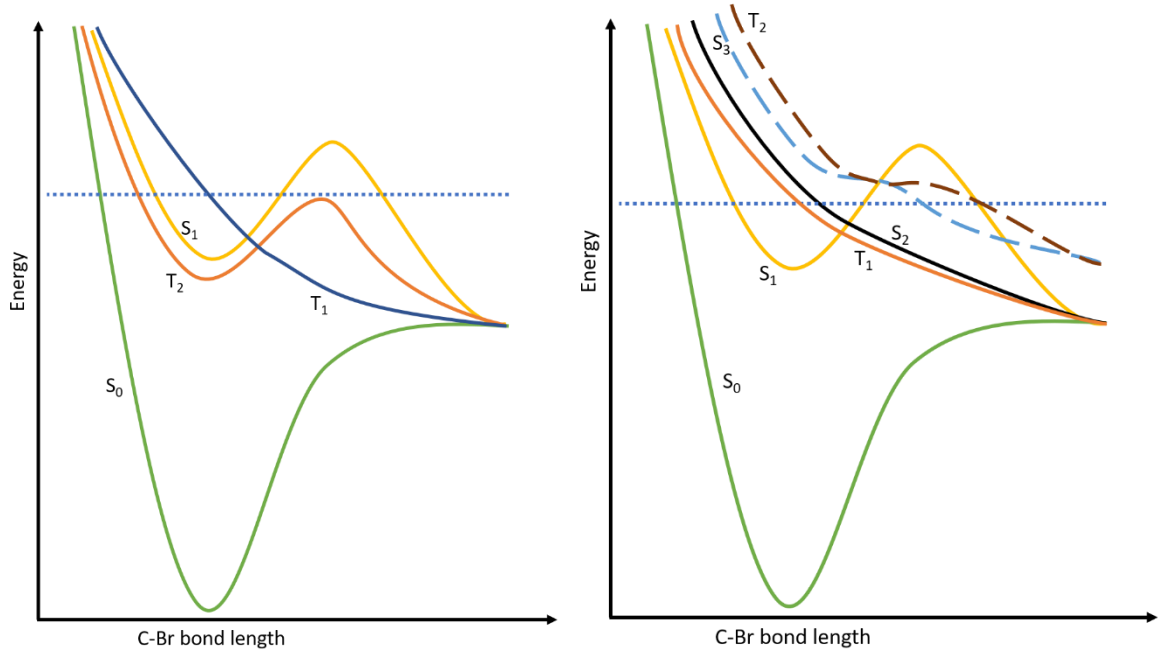

Figure 21: Simplified representations of possible electronic states and their dependence on C-Br bond length for o-bromofluorobenzene, based on prior work by Borg et al.[167] (left) and Li et al.[183] (right). The horizontal dashed line denotes the excitation energy at 270 nm, the wavelength used in the experimental work on this species.

to dissociation. This pathway would be analogous to a $S_0 \rightarrow S_1 \rightarrow T_2$ pathway on the PESs shown on the left of Figure 21. The experimental studies described this pathway as leading to anisotropic product recoil velocities, with a total kinetic energy release (TKER) substantially below the maximum amount of energy available.

Borg *et al.* studied o-, m- and p-bromofluorobenzene, as well as selected di- and penta-fluorobromobenzenes, at the CASPT2 level of theory[184] using a contracted form of the ANO-S basis set[185] for hydrogen, fluorine and carbon and a contracted relativistic ECP basis set[186] for bromine. This computational work was paired with TOF-MS experimental studies. The calculations produced the PESs depicted on the left of Figure 21, and identified two pathways for dissociation of o- and m-bromofluorobenzene at 270 nm. One was confidently assigned to $S_0 \rightarrow S_1 \rightarrow T_1$ dynamics, with the S_1 and T_1 states being of $\pi\pi^*$ and $\pi\sigma^*$ character respectively. The other pathway was suggested to be a direct photoexcitation into bound state T_2, at an energy above the barrier to dissociation. Direct excitation to the T_2 state is enabled by spin-orbit mixing with the nearby S_1 state.[167] VMI work performed by Tang *et al.* assigned further details to these two pathways. These VMI studies determined the purported

$S_0 \rightarrow S_1 \rightarrow T_1$ pathway to be isotropic, due to slow ISC that lasts longer than a rotational period, with maximal TKER. The anisotropic pathway they observed was assigned to prompt dissociation via the T_2 pathway. Tang *et al*. explained Gu *et al*.'s contrasting results as being due to a lack of resolution between the two pathways.[178]

Li *et al.* subsequently performed computational studies on the same three bromofluorobenzenes using CASPT2/CASSI-SO theory[187] and a contraction of the ANO-VTZ basis set[188] for all atoms. A simplified representation of their PESs is shown on the right of Figure 21. This simplification shows only states relevant to their assignment of dissociative pathways, and T_1 and T_2 in this figure each represent three triplet electronic states of similar energy (with each trio relating to the same overall pathway). The numbering used here is based on this simplified representation. Li *et al.* supported Tang *et al.*'s assignment of a slow pathway via an initial $S_0 \rightarrow S_1$ excitation followed by ISC to T_1. However, Li *et al.* were unable to find evidence of a directly accessible triplet state for a fast pathway so rejected the assignment of direct excitation to such a state. Instead all pathways were assigned as passing through the same initial excitation to a singlet state, followed by either fast internal conversion into S_2 for prompt, anisotropic dissociation, or slow intersystem crossing into T_1 for a longer-lived, isotropic pathway. Both pathways exclusively produced spin-orbit ground state bromine atoms, with the spin-orbit excited form produced by a pair of higher-lying states (S_3 and T_2) crossing the same singlet state, which arise from spin-orbit mixing of repulsive singlet and triplet states.[183]

This chapter presents molecular beam and velocity map imaging (VMI) studies characterising the photochemistry of DBFB on a nanosecond timescale, accompanied by TD-DFT calculations to assist in assignment of the features. This work expands the studies of bromofluorobenzene dissociation into a more complex molecule and was undertaken as preparation for further research into the photodynamics of DBFB at shorter timescales, potentially using either XUV core electron ionisation or through Coulomb Explosion Imaging techniques. The conclusions of such a body of research would then address further factors beyond those present in monobromofluorobenzenes, such as any impact of a second heavy atom on the dissociative pathways and the relative propensities of dissociation of each of the two C-Br bonds.

4.2. Experimental Methods

This work utilised the molecular beam and velocity map imaging apparatus described in Chapter 2. A sample of DBFB was sourced from Sigma Aldrich at a purity of 98%. This sample was applied to glass wool held in an inline trap and mildly heated to induce vaporisation. Argon carrier gas (1.5 – 2 bar backing pressure) was passed through this sample to deliver it to the high-vacuum chamber via a General Valve nozzle directed along the time-of-flight axis towards the imaging detector.

Photodissociation studies were undertaken in the same spectral region as the UV spectrum published by Tripathi and Pandey,[93] through both one- and two-colour laser methods. UV radiation in this range was produced by frequency doubling in a BBO crystal the output of either of two tunable pulsed dye lasers (both Sirah, Models PRSC-G-24 and CSTR-G-24, each using Coumarin 540A dye). These dye lasers were each pumped by the third harmonic of a separate Nd:YAG laser (Quanta Ray GCR 200 and Surelite Continuum SLIII-10), both operating at 10 Hz. Both laser sources were loosely focused into the chamber by 50 cm lenses.

Two methods were adopted to investigate the photochemistry: Photofragment Excitation (PHOFEX) Spectroscopy and Velocity Map Imaging. In each case, a pump laser pulse was applied at a selected wavelength between 260 and 285 nm. A probe laser pulse timed to arrive around 40 ns later detected photofragment Br atoms in either the $J=^3/_2$ (hereafter Br) or $J=½$ (Br*) spin-orbit states via a 2 + 1 REMPI process. VMI experiments used either 260.61 nm (ionising via the two-photon resonant Br $^2P_{3/2} – 5p^4D_{3/2}$ transition), or 266.69 nm ($^2P_{1/2} – 5p^4S_{3/2}$) probe wavelengths,[104] and recorded an image over 400,000 – 800,000 ion counts.

In the PHOFEX experiments, only the 260.61 nm detection wavelength was used, recording the integrated ion count signal over 15 laser shots as the pump laser wavelength was scanned with intervals of 0.005 nm. Data were aggregated over multiple scans of up to 6 nm width, and spectra from each scan were scaled by a multiplier such that overlapping regions matched.

Calibration experiments were performed by VMI detection of O^+ from O_2 photolysis at 225 nm.[108] The observed image contains a series of rings corresponding to well-understood dissociation pathways with well-characterised differences in energy. As such, plotting the

speed expected for each ring (calculated from conservation of energy and linear momentum) against the radial distance allows the determination of speed per radial pixel.[189] In the studies reported here, this image radius calibration factor was 7.09 ± 0.19 ms^{-1} $pixel^{-1}$.

4.3. Experimental Results

The PHOFEX spectrum, shown in Figure 22, clearly shows multiple peaks, particularly in the 272 – 283 nm region. Many of these peaks overlap with transitions identified in the UV spectrum recorded by Tripathi and Pandey.[93] Major observed peaks from the current work are listed in Table 4, along with peaks and assignments recorded by Tripathi and Pandey that may be contributing. As previously noted, the assignments involving an excited state mode at a wavenumber of 714 cm^{-1} are of particular interest as this mode is expected to involve a C-Br bond.

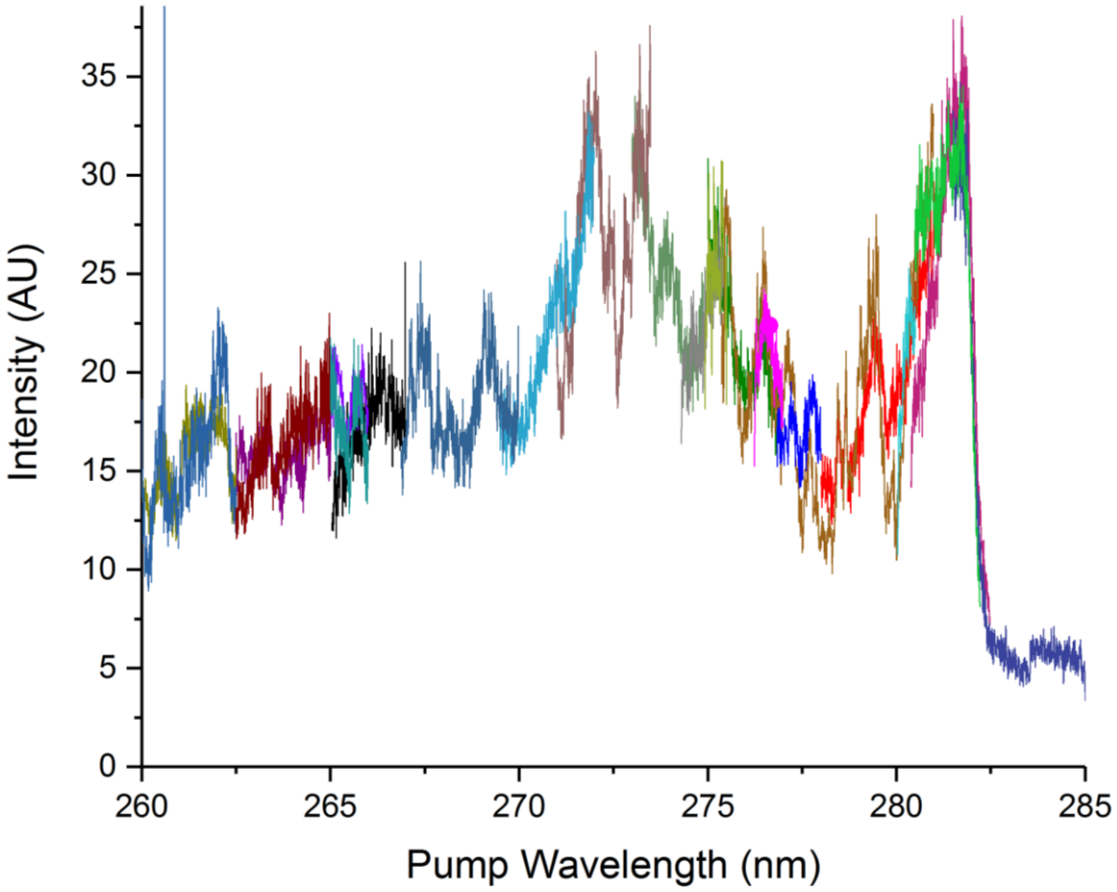

Figure 22: PHOFEX spectrum of DBFB, detecting Br fragments by 2+1 REMPI at a wavelength of 260.61 nm. Colours indicate the individual scans that were joined to make the full spectrum. All data has been smoothed by a 5 point (corresponding to 0.0125 nm) Savitzky-Golay filter.

This Work	Previously Observed	
Wavelength	Wavelength (nm)	Assignment (cm^{-1})
281.8	281.85	(0,0) – 30
	281.61	(0,0)
279.5		
277.8		
277.2	276.95	(0,0) + 714 – 4 x 30 (0,0) + 714 – 119 (0,0) + 627 – 30
276.5	276.72	(0,0) + 627 (0,0) + 714 – 3 x 30
	276.56	(0,0) + 714 – 2 x 30
	276.33	(0,0) + 714 – 30
275.3	275.63	(0,0) + 770
	275.45	(0,0) + 836 – 30
	275.13	(0,0) + 836
273.9		
273.2	273.43	(0,0) + 1087 – 30
	273.25	(0,0) + 1087
272.0		
269.0	269.37	(0,0) + 770 + 836
	269.17	(0,0) + 836 x 2 – 30
	268.90	(0,0) + 836 x 2
267.4		
262.0		

Table 4: The wavelengths of peaks observed in the PHOFEX spectrum of DBFB recorded in the current work, along with bands and assignments from Reference 93. The peak wavelengths reported from the current work correspond to maximum intensities of the observed bands. The final column lists possible assignments from Reference [93]. Here (0,0) indicates the origin of the electronic transition, positive numbers are vibrational excitations of the upper electronic state and negative numbers are difference frequencies resulting from vibrationally excited DBFB in the lower electronic state. The 714 cm^{-1} frequency is attributed to the C-Br bond of S_1 DBFB.

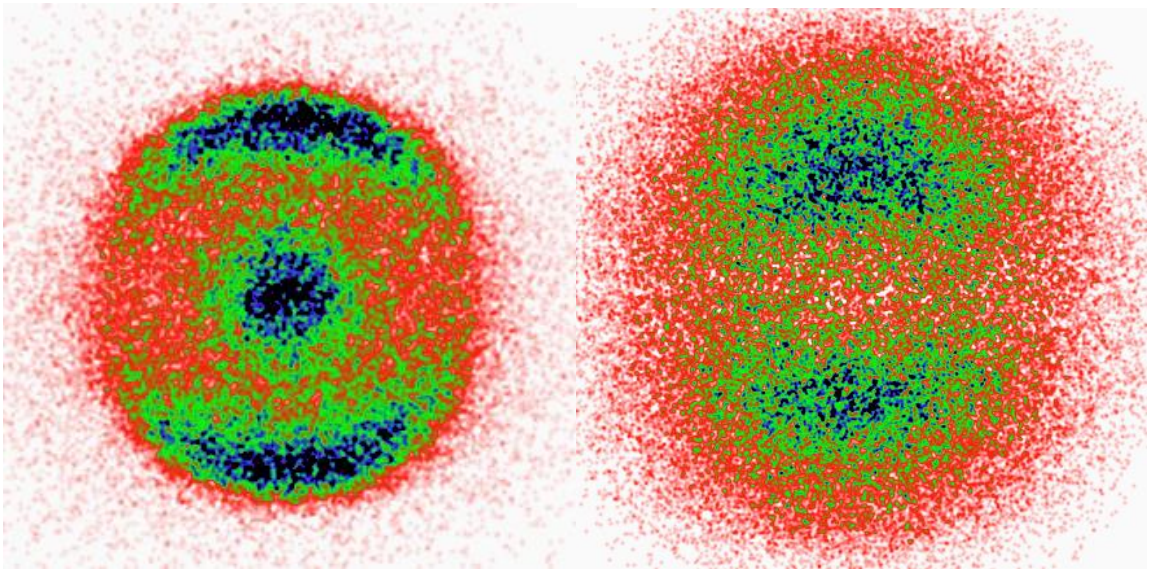

Figure 23: Typical raw, DC sliced VMI images for Br (left) and Br* (right) from the photolysis of DBFB. The Br is detected at 260.61 nm, with the image shown being after excitation of DBFB at 279.5 nm. The Br* is detected at 266.69 nm, with the image shown using only this wavelength for excitation of DBFB and detection of Br*. All lasers are polarised vertically in the plane of the image.

Typical raw VMI images for each Br spin-orbit state are shown in Figure 23. Br VMI studies produced images with pronounced structure, consisting largely of a sharp anisotropic ring at a radial distance of around 750 ms^{-1}, along with a broad, largely isotropic signal extending from the image centre to radii corresponding to speeds above 1000 ms^{-1}. Speed distributions at different pump wavelengths are shown as angular integrations in Figure 24a. Application of Equation 32, derived from the conservation of linear momentum, converts these speed distributions into total kinetic energy release of the photofragments. In this equation m_x and v_x are the mass and speed of species x respectively, and BFB is the bromofluorobenzyl radical cofragment (C_6H_3BrF). These TKER distributions are shown in Figure 24b.

$$TKER = \frac{1}{2} m_{Br} v_{Br}^2 \times \frac{m_{DBFB}}{m_{BFB.}}$$

Equation 32

To better display the trend across wavelengths, the speed distributions were fitted using Origin to the sum of two Gaussian functions. These Gaussians consisted of a narrow, intense function for the peak around 800 ms^{-1}, and a broader function across the full image width to account for the underlying component. A demonstration of this fit is shown in Figure 25a, and the TKER values for the mean speed of these Gaussian functions are plotted in Figure 25b.

a)

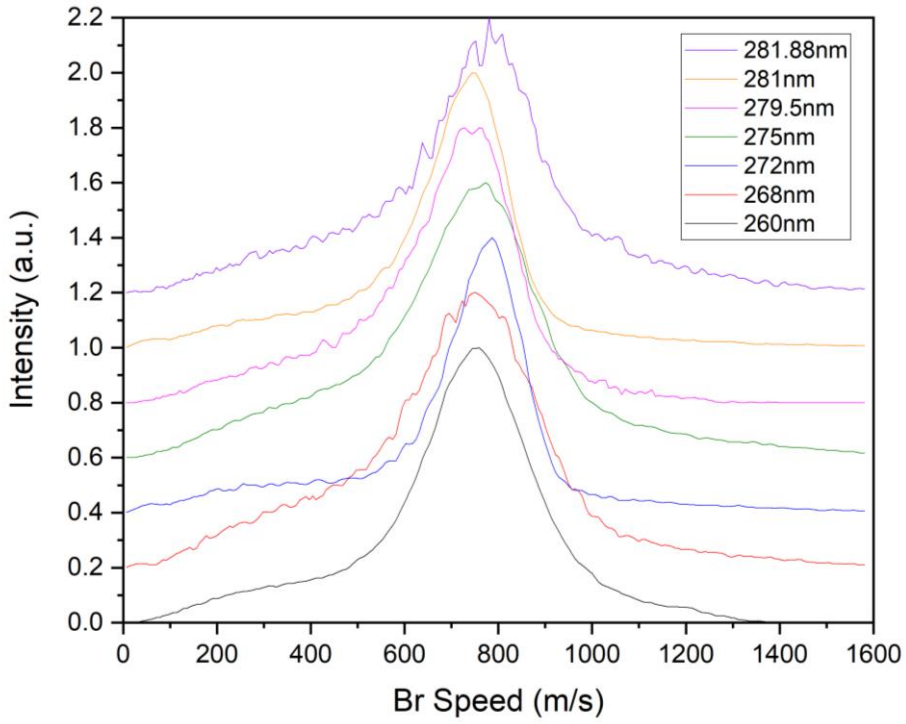

b)

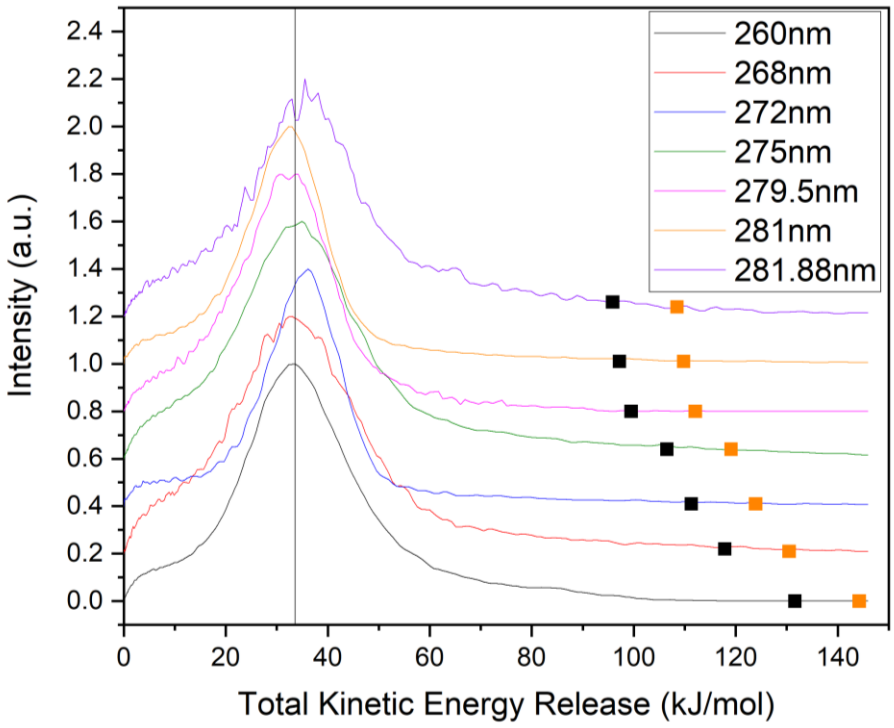

Figure 24: Speed (a) and Total Kinetic Energy Release (b) distributions of Br atoms (detected by 2+1 REMPI at 260.61 nm) from DBFB photolysis at different UV wavelengths shown by the inset colour keys. Panel (b) includes a vertical reference line at the peak for 260nm (33.6 kJ mol^{-1}) and the estimated maximum possible TKER values, using literature bond dissociation energies for ortho- (black) and para- (orange) bromofluorobenzene. Individual traces have been offset vertically to better distinguish the data sets.

Linear fits of each of these produce slopes of -0.01 ± 0.06 kJ mol^{-1} nm^{-1} for the narrow peak, and -0.28 ± 0.10 kJ mol^{-1} nm^{-1} for the broad peak. This analysis shows that the mean TKER of the narrow peak is effectively independent of excitation wavelength, while the broad peak shows a gradual increase in TKER at lower wavelengths (greater photon energies).

Using the C-Br bond dissociation energies for o-bromofluorobenzene and p-bromofluorobenzene reported by Tang et al. of 328.8 and 316.2 kJ mol^{-1} respectively,[178] it is possible to compare the overall TKER distributions, and the means of each fitted Gaussian function, with the maximum possible value based on conservation of energy. Figure 24b compares the maximum possible TKERs for ortho and para Br-atom loss with the overall distribution. Figure 26 subsequently shows the proportion of excess energy apportioned into internal energy at the maximum of the intense peak: at least 60% of the total available energy becomes internal energy of the bromofluorobenzyl cofragment, with an increase at shorter wavelengths in keeping with the consistent TKER value.

Br* proved very difficult to detect. Only one image of quality suitable for analysis could be recorded, and was produced under one-colour photolysis and REMPI detection conditions at 266.69 nm. This image is reproduced on the right of Figure 23, and Figure 27 shows the TKER distribution derived from image analysis. This TKER plot shows signal extending to much higher energies than are observed for ground-state Br($^2P_{3/2}$), which is likely the result of imperfect background subtraction caused by a low signal-to-noise ratio. Only the peak TKER intensity region around 40 kJ mol^{-1} can be confidently considered to have comparable signal to that observed for Br($^2P_{3/2}$). These experimental observations suggest that spin-orbit excited Br($^2P_{1/2}$) is a minor product of the photodissociation of DBFB at the UV excitation wavelengths used here.

The spatial anisotropy of the bromine atom recoil velocities from DBFB photolysis can be characterised by a β parameter (see section 1.6.1). The Br* image of Figure 2 shows a single identifiable feature with a β-parameter value around +0.5. Velocity map images of ground state bromine show isotropic signals at low TKER, with β-parameter values rising to between 0.5 and 1.3 at the maximum intensity point of the TKER distribution. Depictions of some of these TKER-dependent β-parameters are shown in Figure 28. The maximum β parameter varies at different pump wavelengths, with no clear trend. As Figure 29 shows, the measured

a)

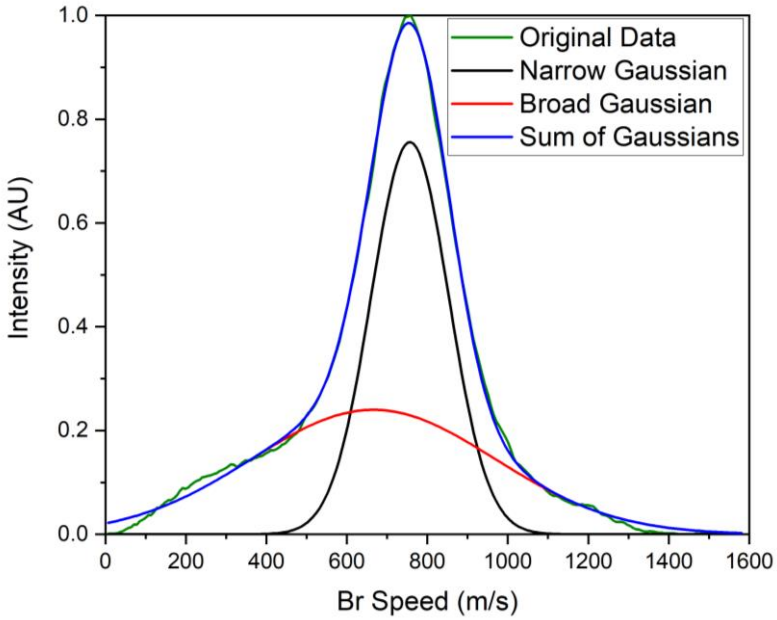

b)

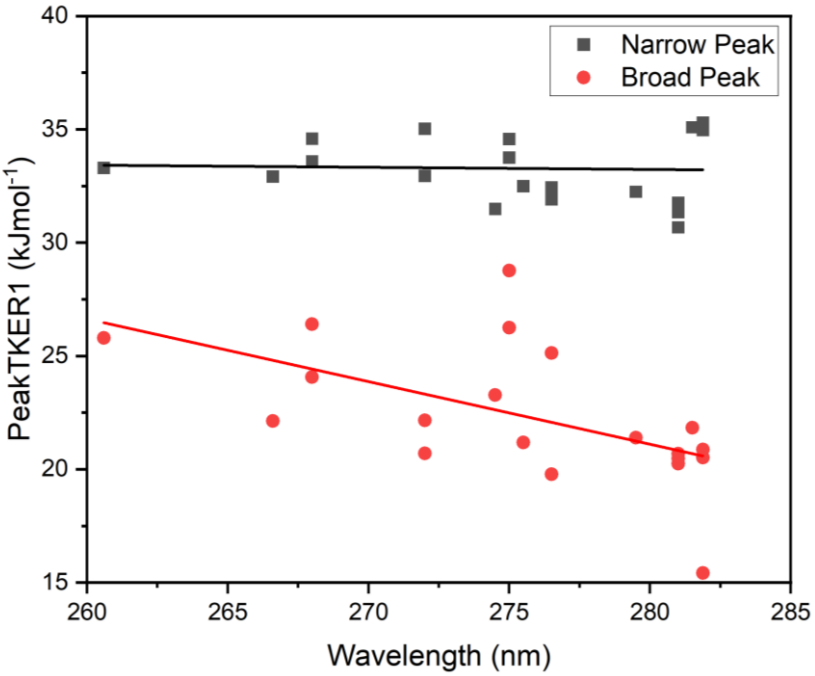

Figure 25: Demonstration and results of the fitting process which was used to decompose the TKER distributions into two components and analyse these. (a) shows the data from detection of Br at a DBFB photolysis wavelength of 260 nm (Green), superimposed with two fitted Gaussian functions (Black and Red) and the sum of the fit (Blue). (b) shows the TKER values at the maxima of each of the two fitted Gaussian functions for the Br ($^2P_{3/2}$) data shown in Figure 24b. The black dots correspond to the narrow peak centred around 35 kJ mol^{-1}, while the red dots are for the broad underlying Gaussian component. Linear fits to each data set are also shown, with gradients of -0.01 ± 0.06 kJ mol^{-1} nm^{-1} for the narrow peak, and -0.28 ± 0.10 kJ mol^{-1} nm^{-1} for the broad peak.

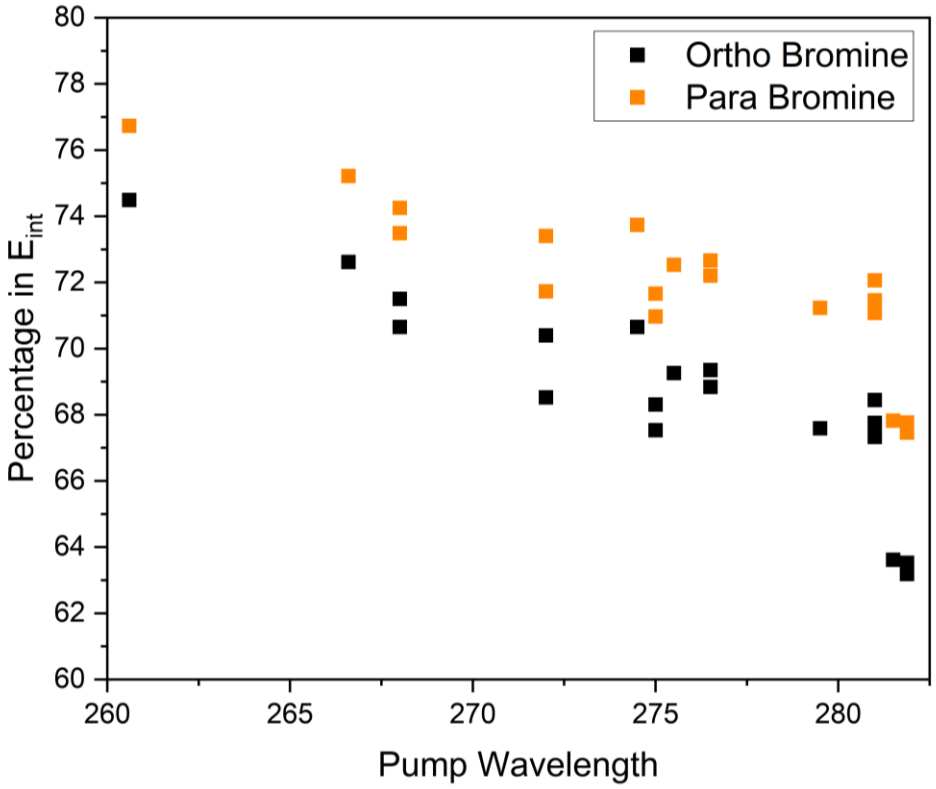

Figure 26: Percentage of excess energy apportioned into internal energy of the bromofluorobenzyl cofragment from the UV photolysis of DBFB. These percentages are shown by wavelength and using previously reported bond dissociation energies for ortho and para bromofluorobenzenes (see main text).

β values of the anisotropic peak appear to correlate well with the partially resolved bands in the PHOFEX spectrum at the same wavelengths. This relationship suggests there may be two or more pathways giving overlapping contributions to each peak in the spectrum, each with different photofragment recoil anisotropy.

4.1. Computational Results

Computational calculations of DBFB energy levels and conformations were performed using Gaussian 09[190] at B3LYP,[35] CAM-B3LYP[191] and ωB97XD[192] levels of theory, all using the aug-cc-pVTZ basis set.[193] These calculations consistently predict a S_0 – S_1 transition with ππ*character, with an S_2 state lying higher in energy with πσ* character but with zero oscillator strength from S_0.

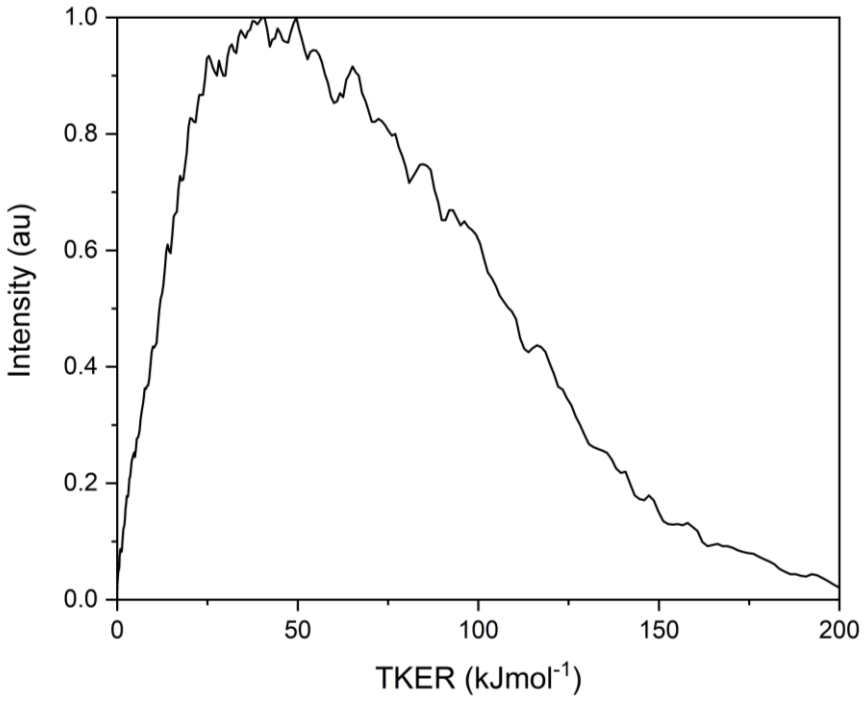

Figure 27: TKER distribution for Br* fragments from the 266.69 nm photolysis of DBFB.

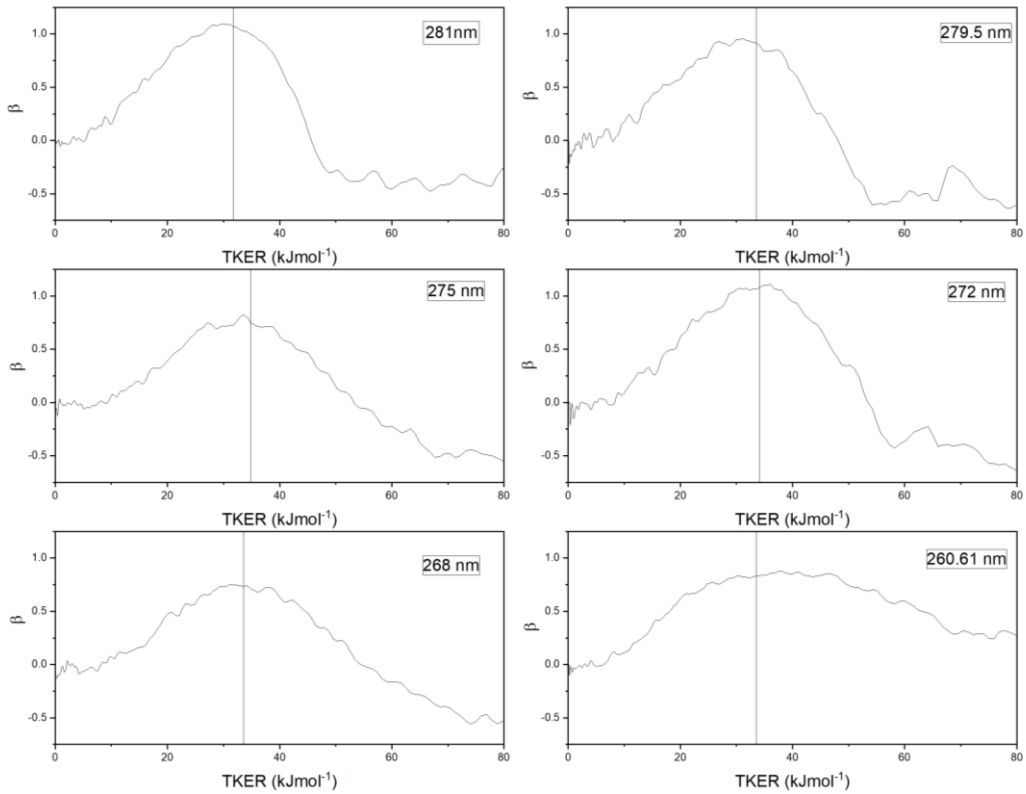

Figure 28: Plot of β values against TKER for Br VMI data obtained for the UV photolysis of DBFB at various UV wavelengths. Vertical lines mark the maximum intensity TKER value.

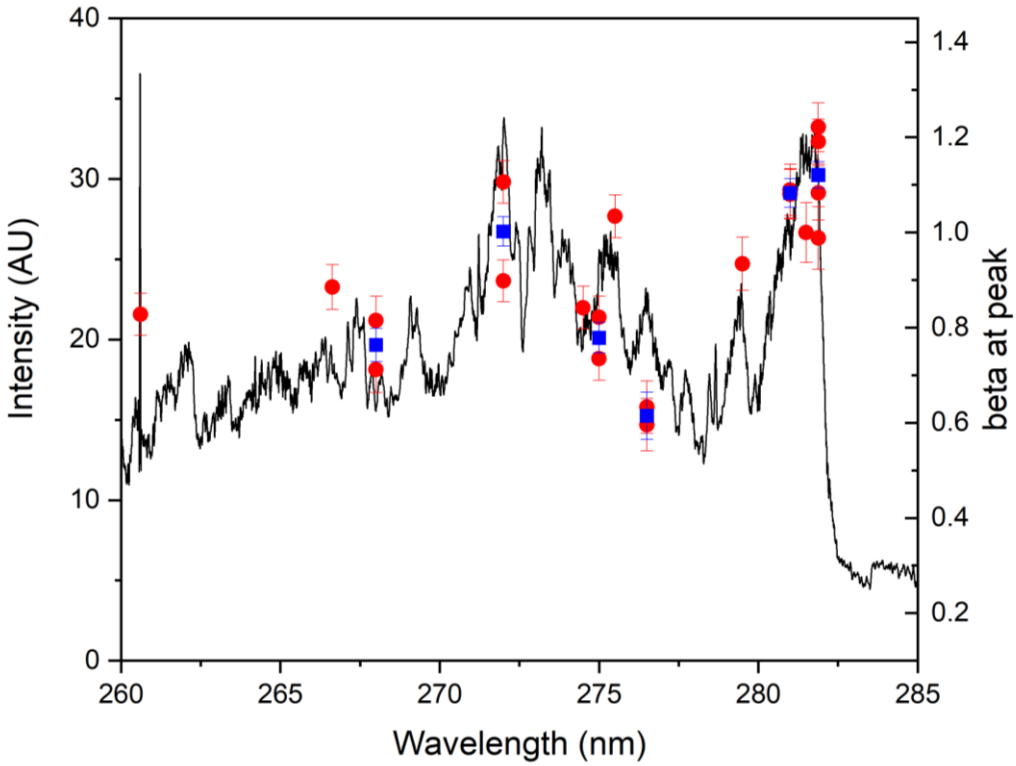

Figure 29: Overlay of the PHOFEX spectrum (black line) obtained by detection of Br fragments from DBFB excitation and the corresponding β parameters (red circles) measured by VMI at selected UV excitation wavelengths. The PHOFEX spectrum has been smoothed by a 40-point (0.1 nm) Savitzky-Golay filter. This graph shows that the β values appear larger near some of the peaks on the PHOFEX spectrum (the β value x-axis scaling has been chosen to best demonstrate this). The error bars in red show the uncertainty in the β value fitting. At six wavelengths, multiple experimental runs were performed, with the average of the fitted β values shown by blue squares, with error bars from error propagation. The excitations known to involve the C-Br bond are those in the 276 – 277 nm region.

The energies predicted for these transitions are significantly higher than the observed transition around 281.88 nm (see Table 5). However this discrepancy is likely caused by errors arising from the quantum chemistry methodologies and would benefit from benchmarking with higher-level calculations, potentially using CAS-SCF which has shown good accuracy in prior studies of disubstituted bromofluorobenzenes.[167, 183] Quantum chemical searches for excited triplet states failed to converge.

Level of Theory	$S_0 - S_1$		$S_0 - S_2$		$S_0 - S_3$	
	E^{vert} /nm	f	E^{vert} /nm	f	E^{vert} /nm	f
B3LYP/aug-cc-pVTZ	258 (A')	0.0292	253 (A'')	0.000	232 (A'')	0.0004
CAM-B3LYP/aug-cc-pVTZ	244 (A')	0.0301	228 (A'')	0.000	215 (A')	0.0360
ωB97XD/aug-cc-pVTZ	244 (A')	0.0303	225 (A'')	0.000	215 (A')	0.0393

Table 5: Computed vertical excitation energies (E^{vert}) and oscillator strengths (f) for the first three singlet states of DBFB and the excited state symmetries.

Due to the lack of oscillator strength to S_2, and S_3 being significantly higher in energy, the main electronic transition in the studied spectral region is therefore assigned to the $S_0 - S_1$ excitation. The transition dipole moment of this excitation lies almost parallel to the ortho C-Br bond (deviating by around 4°). Since the β parameter for a prompt dissociation can be calculated by:

$$\beta = 3\ \cos^2 \chi - 1$$

Equation 33

Where χ is the angle between the transition dipole moment and the velocity vector of the leaving atom,[194] the β parameters for cleavage of the ortho and para C-Br bonds would be expected to be around 1.98 and -0.44 respectively. The observation of a strong parallel transition indicates that prompt loss of the ortho bromine atom is the most significant dissociation pathway detected at the peaks in the TKER distributions.

The minimum energy geometry in the S_1 state, calculated at the ωB97XD/aug-cc-pVTZ level of theory, has the C-Br bond of the ortho bromine atom angled out of the plane of the benzene ring by around 30°, as shown in Figure 30. The bond between the ortho carbon and bromine atom is also lengthened relative to the S_0 geometry by around 0.5 Å, while the para C-Br bond and the C-F bond are both shortened by around 0.1 Å. This evidence further supports the deduction that it is this specific ortho Br atom that is released upon photodissociation. The geometry change may also be contributing to the high internal energy of the bromofluorobenzyl cofragment, with the recoil of the displaced Br atom inducing co-fragment rotation by applying a torque around the benzene ring. This bending distortion also

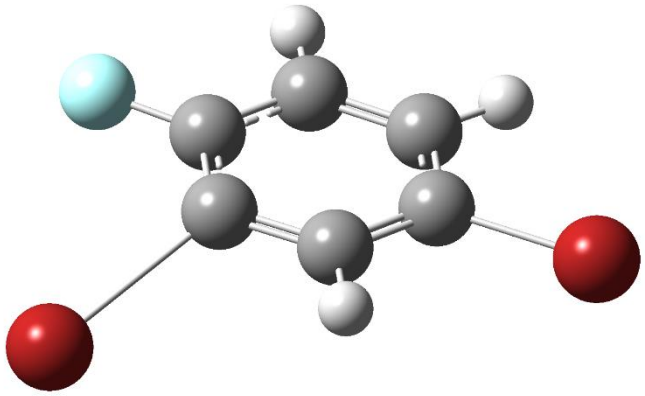

Figure 30: Depiction of the optimised geometry of DBFB in the S_1 state, calculated at the ωB97XD/aug-cc-pVTZ level of theory. The ortho bromine C-Br bond (left) is angled out of the plane of the benzene ring by around 30°, with the bond being extended by 0.5 Å relative to the S_0 geometry. The other C-Br bond and the C-F bond are each shortened by 0.1 Å relative to S_0.

accounts for the difference between the predicted β value above for the planar DBFB geometry and the observed values. The displacement of the ortho Br atom increases the angle between the transition dipole moment and the breaking C-Br bond to around 28°, decreasing β (by Equation 33) to around 1.33, which is in better accord with the maximum values observed in the experimental results.

4.2. Discussion

Although the observation of a prominent anisotropic pathway with TKER significantly below the maximum suggests agreement with the work of Gu *et al*. (with assignment to a $S_0 \rightarrow S_1 \rightarrow T_2$ pathway as summarised in the introduction to this chapter), the observation of varying β values across the region studied is good evidence of there being a mixture of competing pathways, as per the interpretation of Tang *et al*. However, the similarity in β value between that calculated based on the S_1 optimised geometry and the value derived from the experimental images is consistent with a prompt dissociation pathway from the S_1 state, in contrast to the interpretation by Tang *et al*. Since the S_1 state is of ππ* character and is unlikely to have a low enough barrier for direct dissociation from this state, this prompt dissociation pathway would need to involve transfer into a state with σ* character. The similarity between the computed and experimental β values suggests a prompt dissociation pathway, with minimal rotational averaging. This requirement for prompt dissociation makes

the involvement of ISC unlikely, and therefore this process is expected to involve a second singlet state.

This prompt pathway can be assigned to two intersections on the S_1 state, one accessible from the planar geometry and another that only becomes accessible in the bent geometry. At or near the planar geometry the anisotropic pathway likely proceeds through $S_0 \rightarrow S_1 \rightarrow S_2$ (as per the graph to the right of Figure 21), as observed by Li *et al*. The calculations performed above describe S_2 in DBFB as being of πσ* character, and that it is nearby to S_1 (particularly at the B3LYP level) such that it should have a crossing with the S_1 state that is energetically available. This crossing between S_1 and S_2 will be assisted by any movement out-of-plane, which would reduce the symmetry and bring the S_1 and S_2 states to near-degenerate at an avoided crossing. This near-degeneracy enhances the coupling of the S_1 and S_2 states, which will aid dissociation by creating a pathway across a single adiabatic surface which skirts a conical intersection between S_1 and S_2, as observed by Karlsson and Borg *et al*.[168] and shown in Figure 31b. The fast dissociation along this adiabatic surface will maintain the β values predicted from the $S_0 \rightarrow S_1$ excitation and S_1-state geometry relaxation, as is observed in this work.

Borg also observed that when the C-Br bond in o-bromofluorobenzene is angled at 42° from the plane of the benzene ring, a transition between the ππ* S_1 state and an otherwise high-lying singlet nσ* state occurs. The increase in the angle lowers the energy of the crossing point of this nσ* state with the S_1 state to an accessible level, and ensures mixing between the two states, allowing dissociation to occur along an avoided crossing (Borg reports uncertainty as to whether the energetic intersection of the two states is a conical intersection or avoided crossing in the planar geometry).[169] This has recently been observed in 1-bromo-2,6-difluorobenzene[195] and it is likely that a similar transition is also accessible in DBFB, providing another fast pathway with minimal rotational averaging prior to C-Br bond cleavage. This pathway is depicted in Figure 31c. The observation of a 30° angle in the present work, potentially combined with further vibrational excitation of an out-of-plane bending mode, could result in a sufficient angle to make this pathway possible.

Since the non-adiabatic transitions to both the πσ* and nσ* surfaces are assisted by out-of-plane motion of the C-Br bond, vibrational excitation of modes including this motion

could promote these pathways. However, the non-planar minimum energy geometry of S_1 renders such vibrational modes unnecessary because it encourages relaxation to a structure with out-of-plane C-Br distortion. Furthermore, the β value for the region of the PHOFEX spectrum showing the 714 cm^{-1} mode (which is assigned to a C-Br bond) has the lowest of the observed β values (see Figure 29), further suggesting that this mode does not promote either of the above dissociative pathways. In contrast, excitation at the band origin leads to large β values without promoting any vibrational excitation. As such, the significance of the prompt dissociation pathway is expected to be based on variation in the transition moments of vibronic excitations into S_1, rather than on the excitation of particular vibrational modes.

The reduction in the experimentally observed β will come from the involvement of an alternative pathway with either a more isotropic distribution or a negative β parameter. The experimentally observed β value will then be a weighted average of the two pathways' individual β values. The best candidate for a negative β would be dissociation of the para bromine from the S_1 surface, which is predicted to give a β value around -0.44. However, the shortening of the para C-Br bond in the optimised S_1 geometry suggests that the S_1 surface strengthens this bond, making the dissociation of the para bromine unlikely. As such, the alternative pathway is expected to be due to a process involving an ISC step, with the slow rate of ISC processes leading to rotational averaging which reduces β. This ISC step may either be via the S_1 state, in a $S_0 \rightarrow S_1 \rightarrow T_1$ pathway (as is assigned in Li *et al.*'s work), or directly by $S_0 \rightarrow T_2$ excitation (as is assigned in Borg *et al.*'s work). The latter route would be accessible in an electric-dipole transition through spin-orbit coupling with the S_1 state. The smaller β values are expected to correspond to weaker excitations into S_1 (e.g. at wavelengths off-resonant with bands in the PHOFEX spectrum), which would also weaken the contribution from the $S_0 \rightarrow S_1 \rightarrow T_1$ pathway; hence, it is proposed that the reduction in β is a result of an additional direct $S_0 \rightarrow T_2$ excitation pathway.

The very low proportion of Br* product in the dissociation is consistent with the explanation presented in Li *et al.*'s work. This explanation describes Br* production as from higher energy pathways in o-bromofluorobenzene, due to the nature of the spin-orbit coupling. As such a similar effect is expected to be present in DBFB.

a)

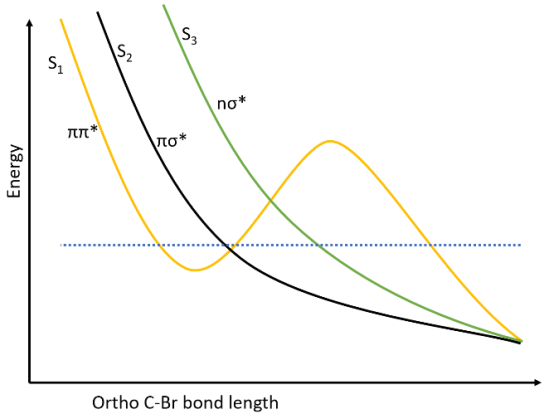

b)

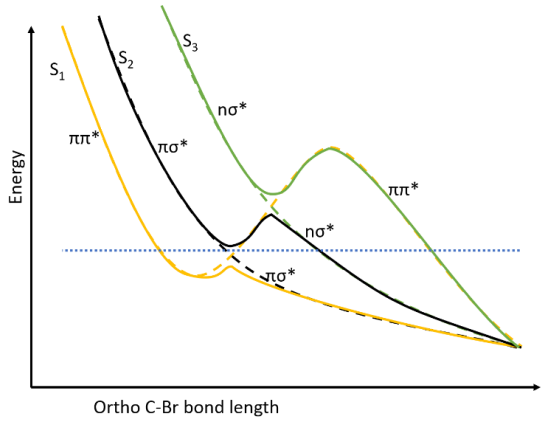

c)

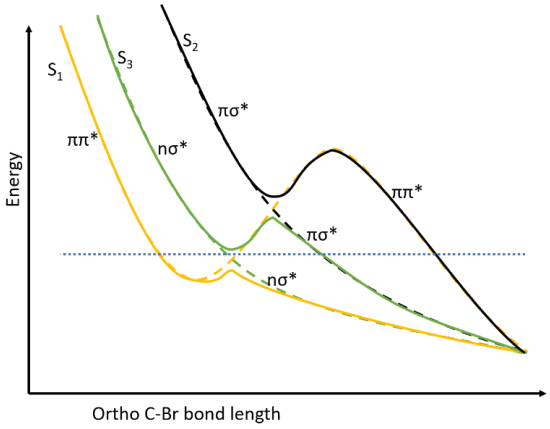

Figure 31: Schematic potential energy surfaces to demonstrate the proposed prompt dissociation pathways of DBFB from S_1. The horizontal blue line on each diagram shows the approximate region of the excitation energy. Panel (a) shows the three relevant states in the planar configuration, whilst (b) and (c) show the same states when the ortho C-Br bond is displaced from the benzene plane by either a small angle (b) or a large angle (c). In the latter two cases, diabatic states are shown by dashed lines to demonstrate the avoided crossings on the adiabatic surfaces (solid lines). Note the intersection of S_1 and S_3 in (a) may either be a conical intersection or an avoided crossing in this geometry. A conical intersection is shown here for simplicity and to better demonstrate the diabatic potentials since it would be substantially above the energetic limit in either case.

The work of Gu *et al*. attributes the reduced TKER of the anisotropic component of the Br photofragment recoil distributions to vibronic excitation of the phenyl ring in the initial excitation. The structure observed in the PHOFEX spectrum supports this vibronic excitation remaining significant in DBFB. This increased internal energy is supplemented in the current work by the observation of the ortho C-Br bond bending out-of-plane. Dissociation along such an out-of-plane vector would apply torque to the benzene ring, and therefore increase the rotational energy of the cofragment. These two sources of internal energy therefore explain the low proportion of TKER observed, relative to the total energy of the system.

The combination of experimental and computational results presented here indicates a preference for ortho C-Br bond dissociation. This preference could also be predicted, based on the influence of the fluorine atom, as discussed by Gu *et al*.[177] Here, the electron-attracting nature of the F atom is argued to weaken C-Br bonds in the vicinity, and a C-Br bond in the ortho position might experience this weakening effect to a greater extent than in the more distant para position.

4.3. Conclusions

The production of Br by photodissociation of 2,4-dibromofluorobenzene has been studied at UV wavelengths in the 260 – 285 nm region. Br is produced in substantial quantity throughout this region up to a threshold around 282 nm. Regions of enhanced photodissociation yield are observed when the wavelength of the UV photolysis laser is scanned into resonance with previously reported vibronic bands which are assigned to the S_1 ($\pi\pi^*$) state. Variation in the β-parameter with photoexcitation on and off resonance with these vibronic features suggests the photodissociation proceeds via more than one pathway. Based on previously published arguments, the competition may arise from a combination of excitation via S_1 followed by either a subsequent $\pi\sigma^*$ or $n\sigma^*$ pathway accounting for the larger β values, and an alternative pathway probably involving direct excitation from S_0 into a triplet state for the smaller β values. Both the $\pi\sigma^*$ and $n\sigma^*$ pathways are promoted by the out-of-plane distortion of the C-Br bond that is observed to occur on the S_1 surface.

Br* is produced substantially less favourably than Br by photodissociation in this wavelength region. The observed preference for Br photoproducts is in keeping with similar observations in other bromofluorobenzenes. Analysis of kinetic energy distributions of Br* is inconclusive

because of the shortage of VMI data of sufficient quality for this minor photoproduct. However, there is evidence from one image that the Br* recoil distributions display some structure, with a peak in TKER at around 40 kJ mol^{-1}, and a positive anisotropy of around $\beta = +0.5$.

Computational studies suggest the bromine atom ortho to the fluorine is bent out of the plane of the benzene ring in the intermediate S_1 state, and may therefore be specifically ejected by the dominant dissociation process. This mechanism is supported by quantitative analysis of observed photofragment β parameters. The out-of-plane distortion may contribute to the observed substantial internal energy of the aromatic co-fragment by promoting rotational or vibrational excitation upon C-Br bond rupture.

5. Inelastic Scattering of NO with Methane

This chapter is adapted, with permission, from "Observation of Rainbows in the Rotationally Inelastic Scattering of NO with CH_4", Xu-Dong Wang, Patrick A. Robertson, Frederick J. J. Cascarini, Mitchell S. Quinn, Joseph W. McManus and Andrew J. Orr-Ewing, J. Phys Chem. A 2019, Vol 123, Issue 36, Pages 7758-7767. Copyright 2019 American Chemical Society.

Minor changes have been made to formatting including figures, section and reference numbers to suit a thesis structure. Supplementary information has also been incorporated into the main text. Details of the experimental apparatus have been moved to Chapter 2.

Contribution to the work:

The experiments reported here were conducted in a crossed molecular beam apparatus designed by Dr Mitchell S. Quinn and constructed and tested by Dr Mitchell S. Quinn and the author of this thesis. Dr Xu-Dong Wang subsequently designed and constructed a modification to improve the differential pumping. Dr Xu-Dong Wang, Dr Patrick A. Robertson, the author of this thesis and undergraduate student Joseph W. McManus worked together to collect all the data. Data analysis and interpretation was shared among the author of this thesis, Dr Xu-Dong Wang, and Dr Patrick A. Robertson, with assistance from Joseph W. McManus. The work was completed under the supervision of Prof Andrew J. Orr-Ewing.

5.1. Introduction

Rotational energy transfer (RET) is a facile and ubiquitous molecular process in important gas-phase environments, such as flames, planetary atmospheres, and the interstellar medium.[196] The dynamics of RET have therefore been extensively studied both experimentally and theoretically,[197, 198] with crossed molecular beam (CMB) scattering experiments providing a direct means to examine RET mechanisms. In combination with resonance-enhanced multiphoton ionization (REMPI) and velocity-map imaging (VMI) detection methods, CMB experiments can be used to obtain the differential cross section (DCS) for the inelastic scattering with quantum-state resolution. Using these state-of-the-art experimental methods, numerous systematic investigations have reported the collisions of NO with rare gases, as well as those of CO with He and Ne and those of OH with He and Ar.[8, 199-204]

In contrast, DCS measurements for collisions between two molecules remain largely unexplored.[205-212] This is probably because of the experimental and theoretical challenges introduced by the additional complexity of molecule–molecule collisions, both in molecular-beam preparation of the colliders and in the analysis and interpretation of the results of experiments. For example, theoretical development of accurate multidimensional potential energy surfaces (PES) and computational simulation of the quantum scattering become much more challenging than that for atom–diatomic molecule collisions. Furthermore, the open-shell nature of NO + CH_4 introduces additional problems associated with diabatization of the potentials.[213] Since many of the systems of practical interest in combustion and atmospheric chemistry involve molecule–molecule collisions, there is a strong desire to improve current understanding and modelling of the associated energy and angular momentum transfer. While there are pioneering reports of measurement of DCSs for molecule–molecule rotational energy transfer using CMB methods with rotatable detectors, with either universal mass-spectrometric or REMPI detection,[214-217] only very recently have some studies appeared which exploit the CMB-VMI approach. Examples include HCl colliding with N_2 or CH_4, where clear evidence of positive rotation–rotation correlations was observed,[218] as well as the first measurements of DCSs for diatomic/polyatomic molecule + diatomic molecule collisions, namely, NO + H_2 and D_2, ND_3 + H_2, and CH_3 + H_2, D_2 and N_2.[205, 206, 219, 220] Here, studies are reported into the rotationally inelastic scattering of NO with CH_4. Although both NO and CH_4 molecules play significant roles in the chemistry of gaseous environments including planetary atmospheres and combustion systems, their inelastic collision dynamics have not been the subject of prior experimental or theoretical study.

The degree of rotational energy transfer between two colliding molecules is controlled by the intermolecular PES. As most inelastic collisions are dominated by repulsive interactions, it is possible to observe rotational rainbows, which are sensitive probes of the PES anisotropy.[221-224] Rotational rainbows manifest as angular maxima in the differential cross sections and have been observed in the elastic, rotationally inelastic, and reactive collisions of atoms and molecules.[6, 225] Simplified, but powerful, classical treatments based on model representations of the forms of the repulsive potentials, such as the two-dimensional hard ellipse model, can provide valuable understanding of the dynamics of the inelastic scattering.[226, 227] Furthermore, the lessons learned about rotational rainbows in the scattering of molecules

with atomic species such as the rare gases can be applied to more complicated system with many more degrees of freedom.[5, 6, 24, 228, 229] By contrast, L-type rainbows arise from attractive forces between collision partners.[9, 24, 203, 227, 230] Quantum mechanically, the L-type rainbows originate from partial waves with higher total angular momentum (J) than the glory partial wave and can therefore only occur when these high partial waves contribute to the scattering cross section. As these partial waves cannot transfer sufficient energy to excite a molecule to high rotational levels, L-type rainbows are particularly prominent for small changes in the rotational angular momentum (j) of the colliding molecule.[26] The inelastic scattering of NO with CH_4 provides an opportunity to observe these L-type rainbows by obtaining velocity-map images for NO scattered into low final angular momentum states j'_{NO} (i.e., low Δj_{NO} transitions).

This chapter details a study of the rotationally inelastic scattering of NO with CH_4 at a mean collision energy of 700 cm^{-1}. DCSs for collisions of NO with CH_4 were experimentally measured using CMB methods coupled with j'_{NO}-level and spin–orbit-state specific REMPI detection and VMI of the scattered NO. Two-dimensional hard ellipse and L-type models are applied to interpret the physical origins of the scattering-angle dependent structures that are observed in the DCSs.

5.2. Experimental Methods

This work utilised the crossed molecular beam velocity map imaging apparatus described in Chapter 2. A 2.5% gaseous mixture of nitric oxide (CK Special Gases Limited, 99%) in argon (Air Liquide, 99.8%) crossed a neat methane beam (Air Liquide, 99.5%) at a 90° angle. The stagnation pressure behind the pulsed nozzle for the expansion of both colliding partners was around 3 bar.

UV radiation in the wavelength range 225–226 nm required for (1 + 1) REMPI detection of scattered NO was generated by frequency doubling in a BBO crystal the output of a tunable pulsed dye laser (Sirah, Model PRSC-G-24, using Coumarin 460 dye) pumped by a Nd:YAG laser (Quanta Ray GCR 200) operating at 10 Hz. The blurring effect on the scattering images of the ion-recoil speed (around 14 m/s) introduced in the (1 + 1) REMPI detection scheme for NO is equivalent to around 1 pixel radius on the detector, and so is small compared to the energy resolution of the apparatus. The energy and line width of the probe laser beam were

1.0 mJ/pulse and 0.4 cm^{-1}, respectively, and the beam was loosely focused into the ionization region of the scattering chamber with a 50 cm focal length lens. The distributions of population over NO rotational levels in the incident supersonic NO/Ar molecular beam, and in the inelastically scattered NO final levels, were probed using (1 + 1) REMPI spectroscopy through the (0, 0) band of the NO $A^2\Sigma^+$–$X^2\Pi$ transition at wavelengths around 226 nm. To probe the rotational states j'_{NO}= 7.5, 8.5, 10.5, 11.5, 12.5, 13.5, 16.5, and 18.5 of NO ($X^2\Pi_{1/2}$), the R_{21} branch was used. For j'_{NO} = 10.5, the overlapping Q_{21} + R_1 branch transitions were also used. These transitions via R_{21} branches probe the Λ-doublet state of f parity for all rotational levels. However, the transitions via the overlapping Q_{21} + R_1 branches probe the Λ-doublet state of e parity for j'_{NO}= 10.5. All spectral assignments were made using the PGOPHER program.[231] In the reported experiments, the Doppler shift of inelastically scattered NO is smaller than the laser line width; therefore, the laser frequency was fixed, rather than scanned over the full width of the Doppler profile of the transition(s).

Nitric oxide ions were extracted through the ion optics assembly, set for VMI conditions, and accelerated onto a position-sensitive detector consisting of a pair of microchannel plates (MCPs; 75 mm diameter), a phosphor screen, and CCD camera. A high-voltage pulse with a width of about 100 ns was applied to the front microchannel plate to detect selectively a central portion of the ion packet. This pulse also acted as a mass gate to remove interferences from other ions. Since the temporal widths of the scattered NO product Newton spheres are around 150 ns in the experiments, the Finite Slice Analysis (FINA) method was used to reconstruct the images to obtain the velocity distributions of the scattered products.[232] After reconstruction, the images and the total translational energy distributions were sharper, but the overall profiles and peak positions remained similar. A more detailed discussion appears on page 85. The two molecular beams and the REMPI probe laser beam propagated in a plane parallel to the face of the VMI detector and were aligned to optimize the scattering signal. The nozzle producing the beam of neat methane was operated in a repeating mode of 50 shots on and 50 shots off. The desired scattering signal was then obtained by subtraction of the background (i.e., without methane) image from the total image.

The collision energy in the measurements was 700 ± 80 cm^{-1} and was precisely determined by analysing velocity-map images of the beam spots obtained using REMPI detection of NO present in the NO/Ar molecular beam, and seeded at a low concentration into the CH_4

molecular beam. The measured mean collision energy agrees with a value of 680 cm^{-1} expected for molecular beam velocities of room-temperature NO seeded in Ar and of neat CH_4 of 560 and 1100 m/s, respectively.[18] The rotational level population distribution in the incident NO beam was determined by comparison of experimental spectra using an unfocused and attenuated ionization laser (with energy of less than 0.1 mJ per pulse to avoid saturation effects) with spectra simulated using the PGOPHER program. The NO molecules were determined to be cooled to a rotational temperature of 6 ± 2 K, at which 90% of NO molecules were in the lowest quantum state (j_{NO} = 0.5, Ω = 1/2) with an equal population of the two Λ-doublet (e/f) levels. Supersonic expansion of neat CH_4 without a seed gas does not lead to comparably efficient rotational cooling. Previous investigation showed that after such an expansion the methane molecules were distributed as follows: 31% in j_{CH4} = 0, 56% in j_{CH4} = 1, and 13% in j_{CH4} = 2.[233] In addition, the rotational temperature of CH_4 molecules in a neat methane molecular beam was previously estimated to be about 9 K from the measured speed distribution.[225, 234] Although vibrational cooling of the molecular beams is expected to be poor, <0.1% of NO or CH_4 molecules are vibrationally excited at room temperature. Due to this, vibrational excitation of the incident beams is expected to have minimal impact on the results.[235, 236]

In the crossed molecular beam experiment, the measured signals are proportional to the number density of the scattered NO products within the detection laser volume at the time the detection laser arrives, and depend on parameters such as the molecular beam pulse durations and lab frame speeds of the scattered NO. Therefore, prior to any analysis of experimental images, a density-to-flux transformation is required to correct the images for the nonuniform detection efficiency. DCSs can then be extracted from the corrected images. A similar computer program to that of Liu,[77] but custom-written and based on the Bristol laboratory's apparatus and experimental parameters, is used here for the density-to-flux transformation.

An example of its application is shown in Figure 32. In this figure, panel (a) shows a raw image for inelastic scattering of NO with CH_4 into the final rotational level j'_{NO}=11.5, for which the signal intensity in the top right side, corresponding to slower speeds in the laboratory frame, is higher than in the top left side. In this image, the relative velocity vector lies along the

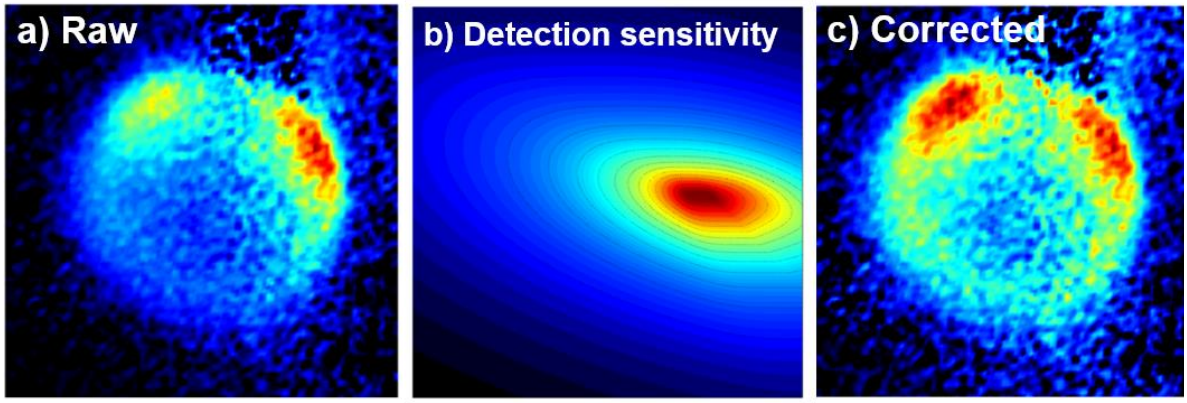

Figure 32: Density-to-flux transformation for an image of scattered NO with the final rotational level j'_{NO}=11.5. (a) Raw image; (b) simulated detection sensitivity function; (c) corrected image. The corrected image is acquired by division of the raw image by the detection sensitivity function. The Newton diagram for this data is the same as in Figure 36.

positive diagonal between these two regions of product scattering, and the DCS should be symmetric about this vector. To correct for biases in detection, all intensity data in this image are divided by the velocity-dependent detection sensitivity function shown in Figure 32(b), which is generated by the density-to-flux computer code. As a result, a density-to-flux corrected image is obtained, as is shown in Figure 32(c). In Figure 33, the black and red lines represent DCSs extracted from the raw and corrected images, respectively. The corrected DCS is close to symmetric with respect to a scattering angle of 180°.

To assess the impact of partial slicing of the experimental images, the Finite slice analysis (FINA) method was used to reconstruct the scattering images. Unlike most methods for image reconstruction, the FINA method does not require cylindrical symmetry in the scattering image.[232] Figure 34 shows the FINA reconstructed images for inelastic scattering of NO with CH_4 into the final rotational levels j'_{NO} = 8.5, 12.5. One of the most important parameters employed in FINA processing is slice width, and sliced widths of 80% and 90% are input for reconstruction of the images of j'_{NO} = 8.5, 12.5, respectively. The profiles of the overlapped rings are sharper in the reconstructed images compared to the unprocessed images, as shown in Figure 35. However, as can be seen, applying the FINA method to the scattering images introduces additional noise. The poorer signal-to-noise ratio in the reconstructed scattering images originates from the low resolution of the raw images and the interference from the beam spot (corresponding to a very small population of NO in the probed quantum state in

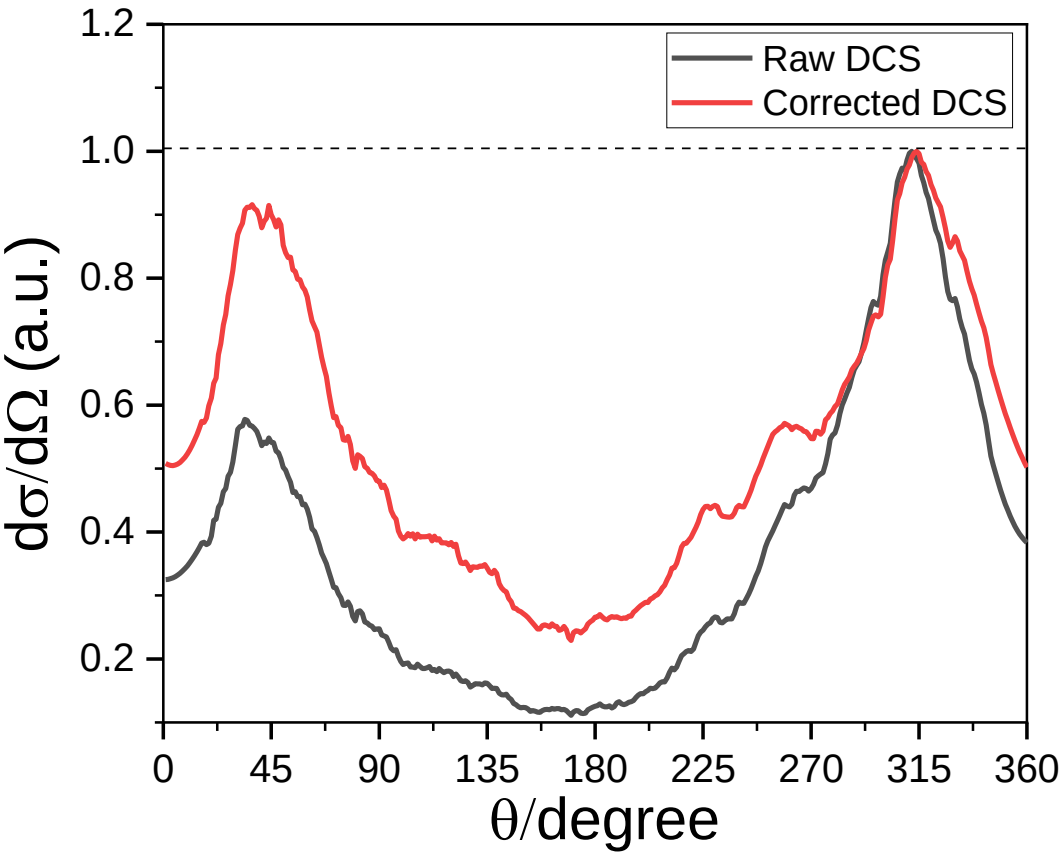

Figure 33 A comparison of DCSs extracted from the raw and corrected images shown in Figure 32 (a) and (c).

the NO/Ar molecular beam). Figure 35 illustrates that the total translational energy distributions obtained from the reconstructed images are sharper than those of unreconstructed images, but that their overall profiles and peak positions are similar. Some structures in the total translational energy distributions in Figure 35 are associated with experimental noise amplified by application of the FINA method.

Prior to investigation of NO + CH_4 scattering dynamics, the rotationally inelastic scattering of NO with Ar was studied at a collision energy of 640 ± 65 cm^{-1}. These experiments test the performance of the new apparatus against previously published studies, and allow comparison of the NO + Ar scattering dynamics with those for NO with CH_4.

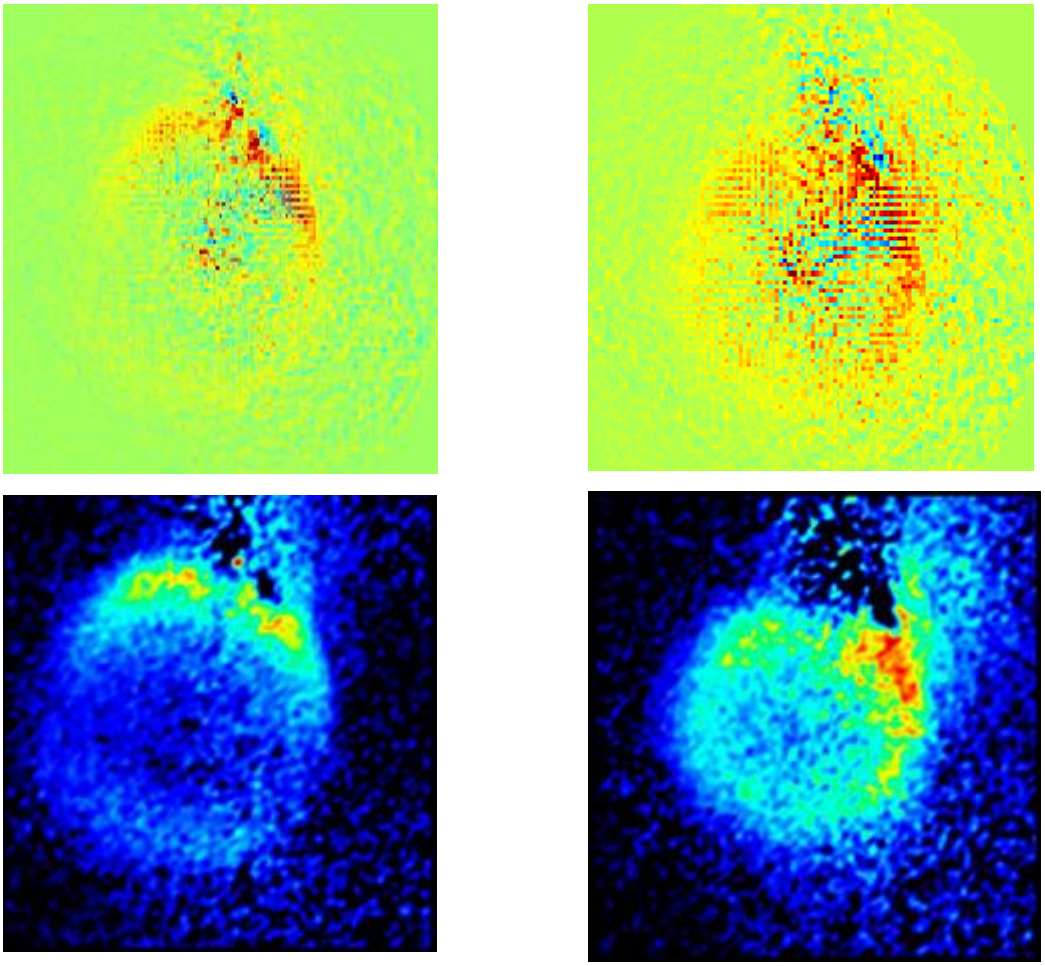

Figure 34: FINA reconstructed version (upper images) for inelastic scattering of NO with CH_4 into the final rotational levels j'_{NO}=8.5 (left), and j'_{NO}=12.5 (right). The unreconstructed versions are presented below each reconstructed image, for comparison.

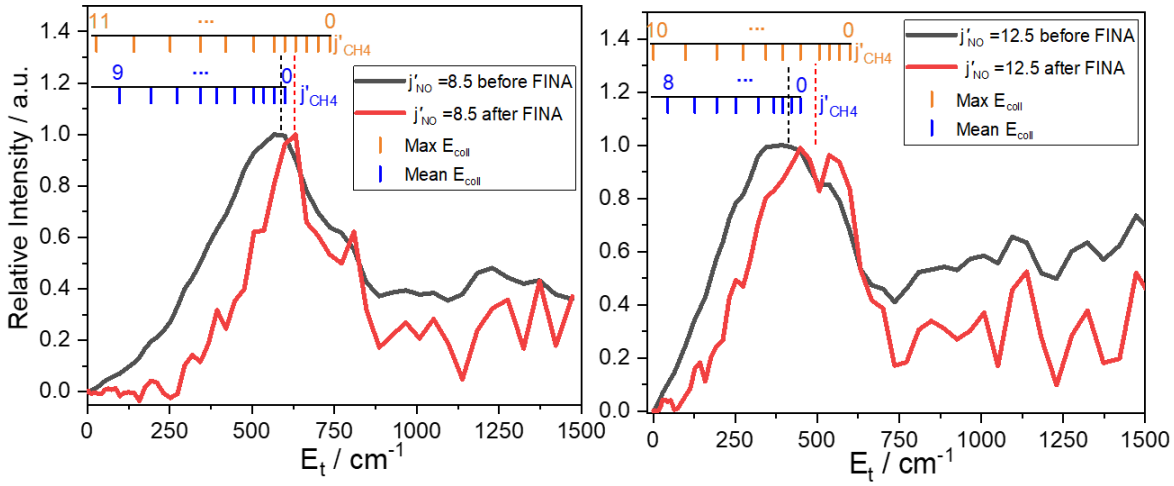

Figure 35: Comparisons of total translational energy distributions for unprocessed and FINA reconstructed images for inelastic scattering of NO with CH_4 into the final rotational levels j'_{NO}=8.5, and 12.5.

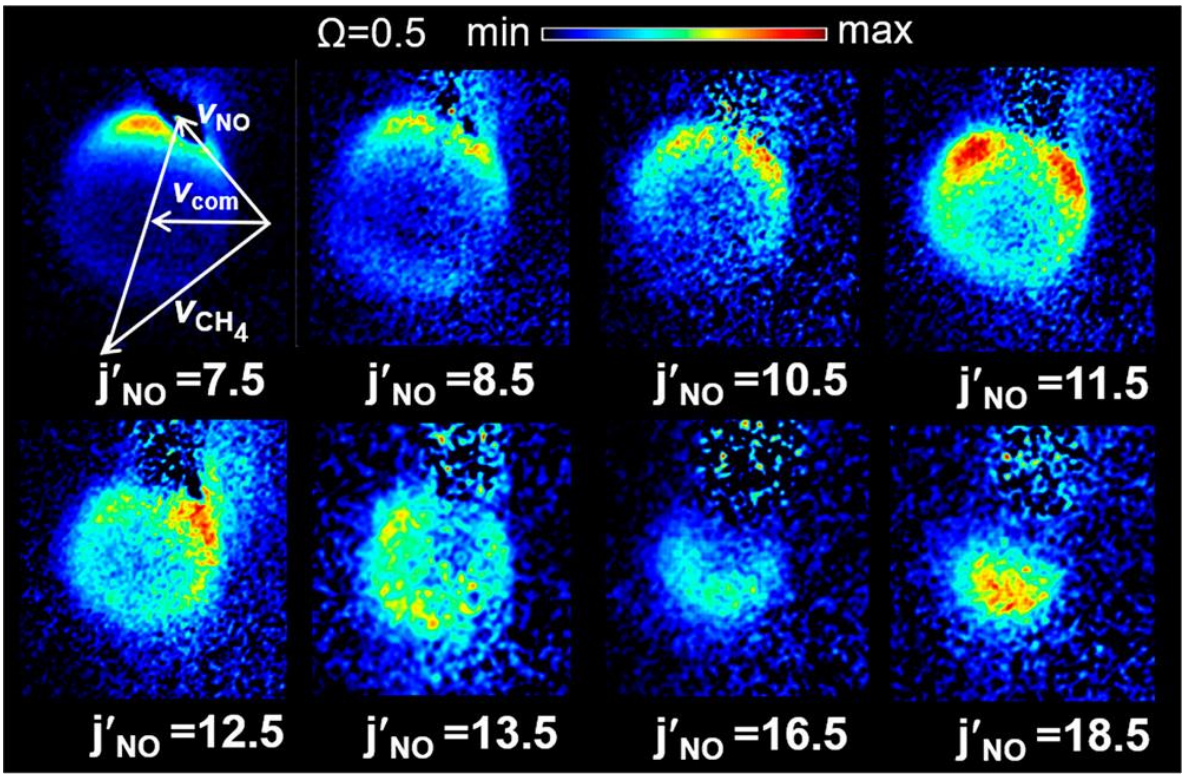

Figure 36: Images for the inelastic scattering of NO with CH_4 into the final rotational levels of NO labelled. Images were obtained at a mean collision energy of 700 cm^{-1}. A Newton diagram superimposed in the top left panel shows the molecular beam velocities v_{NO} and v_{CH4}, the centre-of-mass velocity vector v_{com}, and the relative velocity vector.

5.3. Results and Discussion

5.3.1. DCSs for Rotationally Inelastic Scattering of NO with CH_4.

The experimental velocity images for the inelastic scattering of NO with methane, denoted by their respective final angular momentum quantum numbers j'_{NO} , are shown in Figure 36 for spin−orbit conserving (Ω = 1/2) transitions into the final f Λ-doublet component of NO, CH_4 + NO ($^2\Pi_{1/2}$, j_{NO} = 0.5, f/e) →CH_4 + NO ($^2\Pi_{1/2}$, j'_{NO} , f). The mean collision energy for this inelastic scattering is 700 cm^{-1}. At the same collision energy, spin−orbit changing transitions (to Ω = 3/2) can also occur, and three images for lower Δj_{NO} transitions are given in Figure 37. Images in Figure 36 are corrected with the density-to-flux transformation, and a Newton diagram is superimposed in the first panel. Any remaining asymmetry in the two halves of each image, separated by the relative velocity vector, may be a consequence of either an imperfect density to flux transformation or fluctuations in factors such as laser intensity and molecular beam density. The centre-of-mass (CM) frame scattering angle θ is defined as the angle between the CM frame velocities of NO before and after a collision. It is clear from the

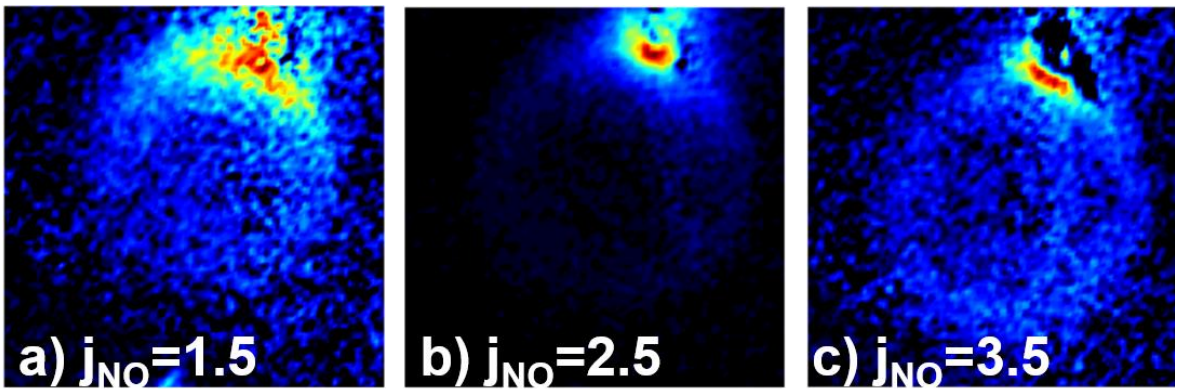

Figure 37: Images for the rotationally inelastic scattering of CH_4 + NO ($^2\Pi_{1/2}$, j'_{NO}=0.5, e/f) $\rightarrow$ CH_4 + NO ($^2\Pi_{3/2}$, j_{NO}, e), for j_{NO}= 1.5 to 3.5, at a mean collision energy of 700 cm^{-1}. The Newton diagram is the same as that shown in Figure 36.

images that the angular scattering distribution gradually shifts from the forward to the backward direction with increment of the final rotational energy of the scattered NO, behaviour which is similar to that observed in the collision of NO with Ar.[237] The radius of the scattering sphere, which scales with the square root of the kinetic energy of the scattered products, decreases with increasing product rotational energy because of conservation of the total energy.

Imperfect subtraction of background signals arising from the unscattered and incompletely cooled NO molecules in the parent molecule beam (referred to here as a beam spot) means that the scattered products cannot be observed in the parts of images closest to the forward scattering direction. In some cases, such as for j'_{NO} = 7.5, the forward scattering cannot be resolved on the right side of the image but can be largely distinguished from the beam spot on the left side.

To investigate the impact of e and f parity on the results, images of j'_{NO} = 10.5 were recorded at both the R_{21} branch, for the final f parity state, and the Q_{21} + R_1 branch for the final e parity state. These images are shown in Figure 38.

One evident difference in these two images is signal intensity, which confirms the expectation from simulated NO spectra that the signal levels of the overlapping Q_{21} + R_1 branches are higher than that of the R_{21} branch for j'_{NO} =10.5. As shown in Figure 39, the normalized DCSs for the transitions to the final e and f states are very similar, indicating that DCSs are not sensitive to the final Λ-doublet level for the j'_{NO} =10.5 final quantum state.

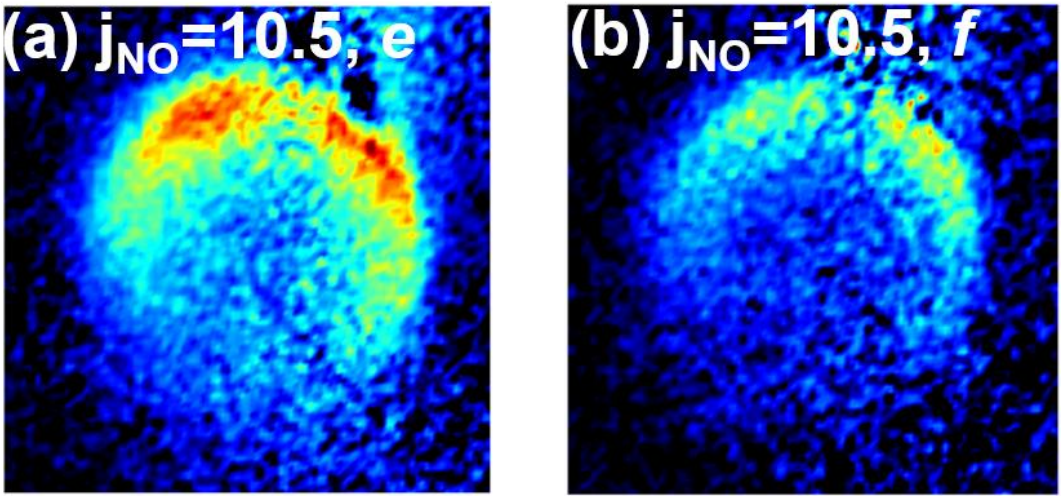

Figure 38: Images for the inelastic scattering of NO with CH_4 into the final rotational levels with quantum number j_{NO} =10.5 and e parity (a), and f parity (b).

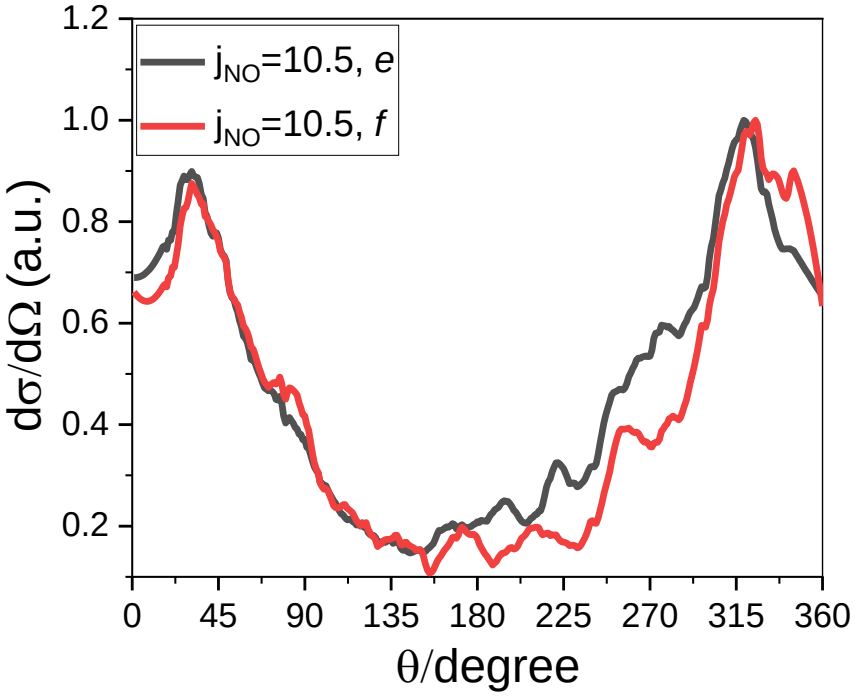

Figure 39 A comparison of DCSs extracted from the images shown in Figure 38 for j_{NO} =10.5 f and e final states.

Figure 40 shows the DCSs (denoted as dσ/dΩ where Ω is the CM frame solid angle) for scattering into all experimentally measured NO final rotational levels, obtained by extracting angular product distributions from scattering images using a custom-written program based on the method of Hall and co-workers.[238] The experimentally recovered DCS has an arbitrary intensity based on the intensity of the experimental image; therefore, angular distributions

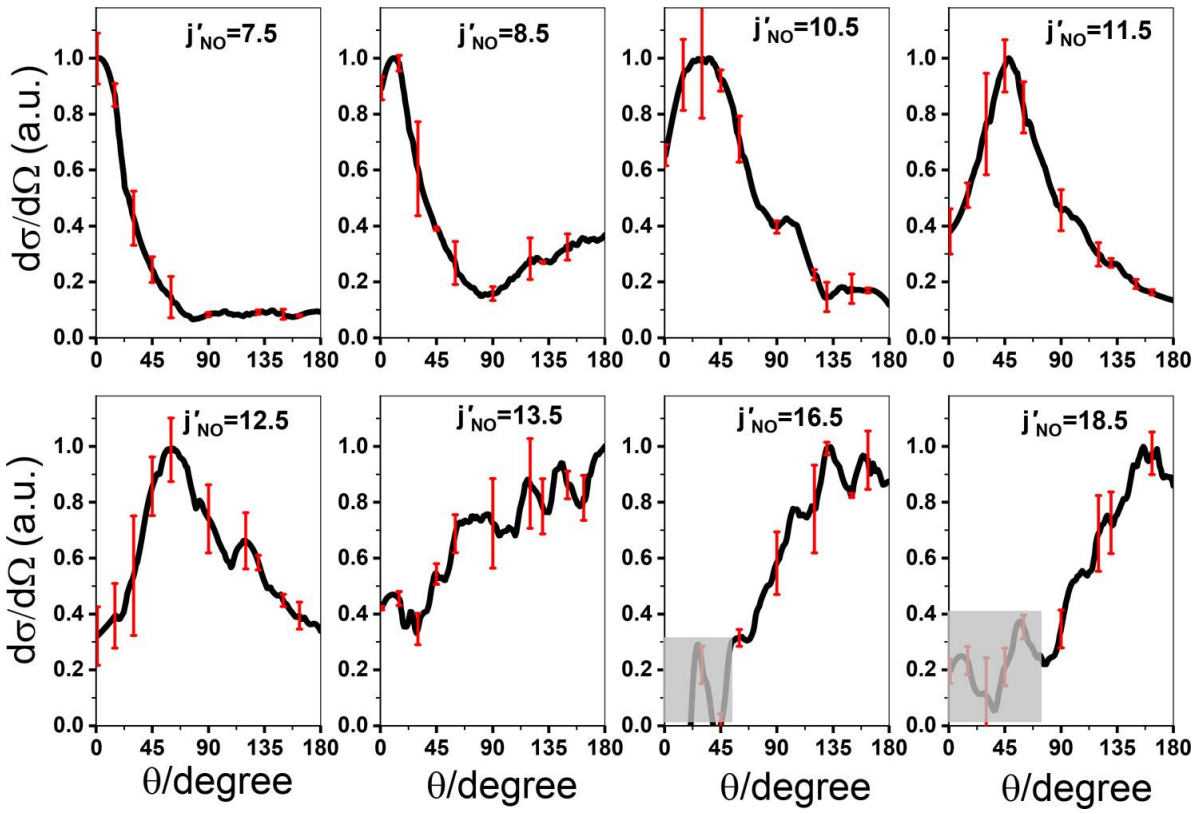

Figure 40: Differential cross sections for the inelastic scattering of NO with CH_4 extracted from the experimental images shown in Figure 36. Labels on the panels indicate the final rotational levels of NO probed (of both e and f parity). The error bars represent the intensity variation at the same scattering angle in the two halves of each image either side of the relative velocity vector. Small sections of the DCSs in the forward scattering direction are masked because, although the beam spots are weak at high j_{NO}', so too are the forward scattered signals.

normalized by maximum height are plotted. The trends observed in the DCSs confirm the qualitative conclusions drawn from the experimental velocity images: forward scattering is predominant for scattering into the lowest j'_{NO} states, with increasing sideways and backward scattering observed for higher j'_{NO} . A single broad maximum in the images corresponding to a peak in the scattering intensity (suggesting a rotational rainbow) monotonically moves from forward to backward scattering with increasing Δj_{NO}, which is broadly consistent with scattering dynamics controlled by repulsive intermolecular interactions. Similar behaviour was previously observed for NO + rare gases inelastic scattering, and it can be accounted for using a two-dimensional hard ellipse model.[5, 237, 239, 240] For NO + Ar inelastic scattering, two rotational rainbows corresponding to scattering at the N and O sites of NO were previously reported for j'_{NO} = 7.5 and 8.5.[237] To compare with the experiment results for inelastic scattering of NO with CH_4, rotationally inelastic scattering of NO with Ar (i.e., Ar + NO ($^2\Pi_{1/2}$,

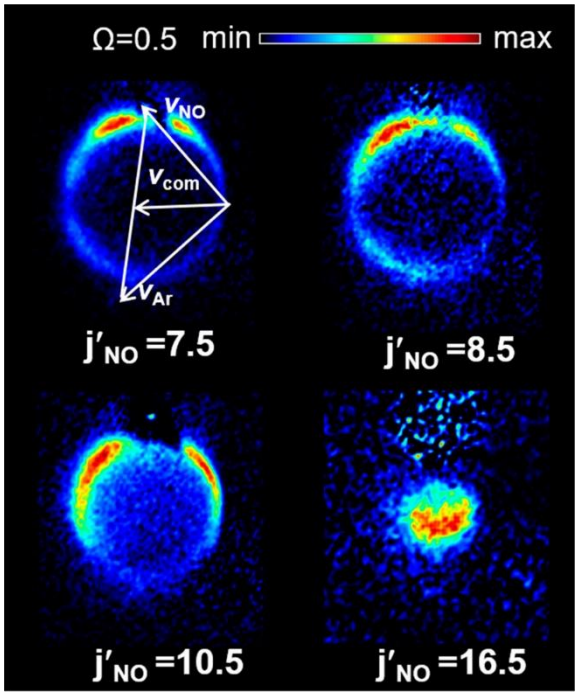

Figure 41: Images of the inelastic scattering of NO with Ar into final rotational levels with quantum numbers j_{NO}' = 7.5, 8.5, 10.5, and 16.5 and f parity. A Newton diagram for the conditions of the experimental measurements is superimposed in the first panel.

j_{NO} = 0.5, f/e) → Ar + NO ($^2\Pi_{1/2}$, j'_{NO} , f)) was investigated at a collision energy of 640 ± 60 cm^{-1} using the Bristol apparatus. The newly measured images shown in Figure 41 agree well with the previous study by Yonekura et al., and the positions of single or multiple rainbow peaks shown in Figure 42 are also in quantitative agreement.[237] As shown in Figure 41, two rotational rainbows can be seen in both images of j'_{NO} = 7.5 and 8.5 in the NO + Ar system. Similarly, for NO + CH_4 inelastic scattering, images of j'_{NO} = 7.5 and 8.5 exhibit a broad distribution in the forward scattering direction and a minor distribution in the backward scattering direction (see Figure 36). Considering the similar character, small differences in collision energy, and the velocity and angular spreads for the molecular beams inferred from the analysis of NO beam spots measured by VMI, it is possible that rotational rainbows are also observed in the NO + CH_4 inelastic scattering. Apart from the main character of a single broad maximum in the DCSs, some oscillatory structures can be seen, in particular for the higher final rotational levels (j'_{NO} = 13.5 and 16.5). Considering the spread in the collision energy (on the order of 10%) and the angular resolution of images (5−13°), along with the

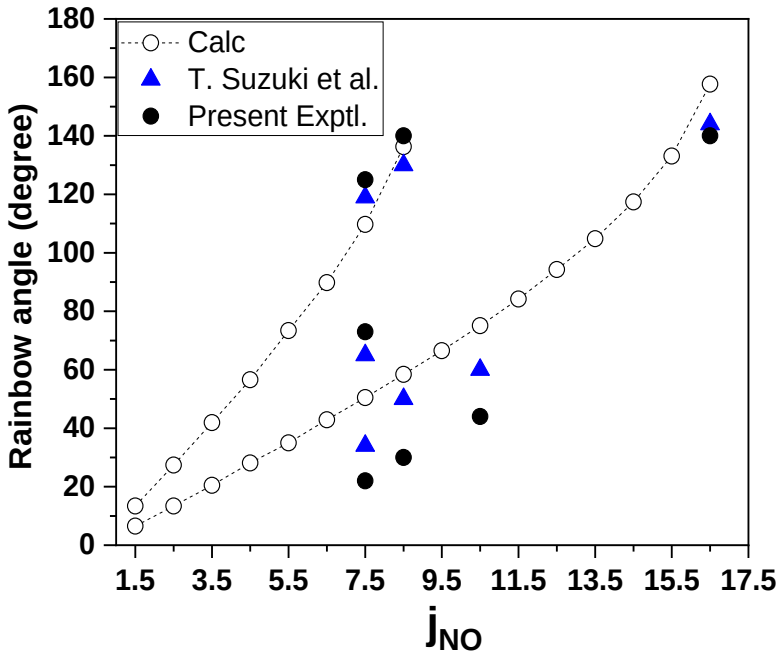

Figure 42: Comparison of the observed rotational rainbow angles obtained from the images for Ar + NO scattering shown in Figure 41 with predictions of a 2-dimensional hard ellipse model, as well as the corresponding angles reported by Suzuki and coworkers.[237] Note that for certain final rotational levels of NO, two or more rotational rainbow angles are observed.

error bars between either half of the image, the oscillatory structures in our DCS plots are more likely to be associated with experimental noise than quantum mechanical effects.

The images for inelastic scattering of NO with CH_4, including those processed by the reconstruction software FINA (see Figure 34), display obviously broader distributions in the radial (speed) coordinate than for Ar scattering with NO. These broad distributions indicate rotational excitation of the coproduct CH_4, which is discussed further in section 5.3.2. However, the general behaviour of the two systems is strikingly similar, with a shift from forward to backward scattering as Δj_{NO} increases.

5.3.1. Classical Models for Interpreting the Physical Origins of Structures Observed in DCSs.

There are no prior reports of classical or quantum mechanical scattering calculations for the NO + CH_4 system with which to compare these experimental results. Therefore, simpler model treatments are needed to guide the interpretation. The measurements show that the direction of the scattering changes from the forward to the backward hemisphere as the

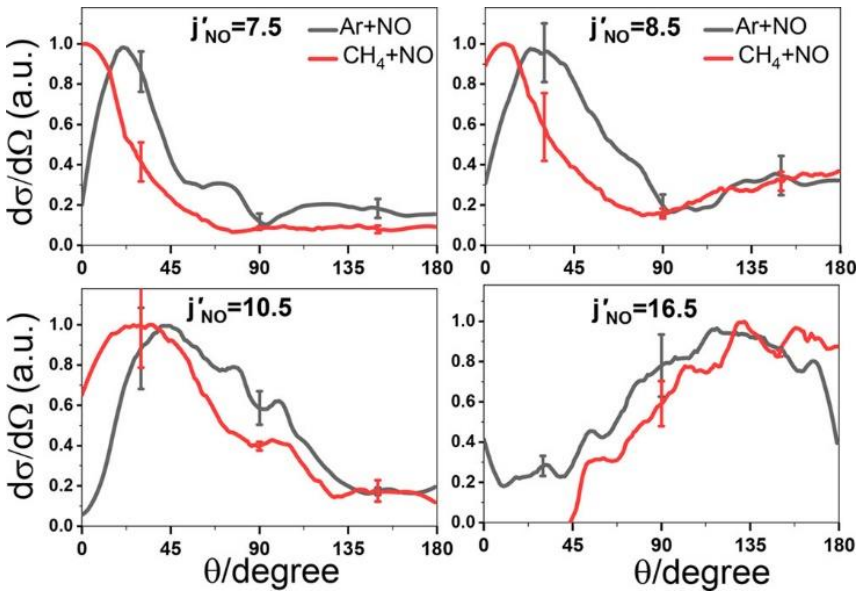

Figure 43: Comparison of DCSs for NO scattering from Ar (black curves) and CH_4 (red curves) for four different final j_{NO}' rotational levels of f parity, as labelled in the panels.

amount of angular momentum imparted to the NO product increases, and classical mechanics provides a qualitative explanation of this trend. Low rotational levels of NO can be populated by large impact parameter collisions at relatively long-range, in glancing impacts that result in only a small deflection of the NO and hence a small transfer of initial linear and orbital angular momenta into product rotational angular momentum. A higher degree of product rotational excitation implies a larger torque during the collision. This larger torque is generated by collisions with smaller impact parameters, and these more head-on collision geometries generally result in more backscattering.

Considering that methane is a spherical top molecule, it is possible that the inelastic scattering of NO with CH_4 can be directly compared to that of NO with Ar. Figure 43 depicts such a comparison of the extracted DCSs for the NO product rotational levels of j'_{NO} = 7.5, 8.5, 10.5, and 16.5 for the two systems. For j'_{NO} = 7.5 and 8.5, the DCSs of the NO + CH_4 system are peaked toward a lower scattering angle than those of the NO + Ar system. Moreover, there is only a single obvious broad maximum in the DCSs of the NO + CH_4 system, whereas one dominant and two minor peaks are seen for j'_{NO} = 7.5 from NO + Ar collisions. However, for j'_{NO} = 10.5 and 16.5, the DCSs show reasonable agreement between the two systems. As is shown in Figure 42, rotational rainbow angles can be well-predicted with a two-dimensional hard ellipse model for the inelastic scattering of Ar with NO. This model, proposed by Bosanac

et al., ignores attractive forces between the two species and approximates the repulsive interaction by a hard ellipse.[25, 241] It is therefore reasonable to suppose that the same model can aid the interpretation of inelastic scattering data for NO collisions with CH_4, at least for population of higher final rotational levels of the product NO. Here, the methane molecule is approximated as behaving as a structureless atom without internal degree of freedom. For an atom-ellipse hard collision model, the rotational rainbow angle θ_r satisfies Equation 34: [222, 240, 241]

$$sin\left(\frac{\theta_r}{2}\right) = \frac{j_f}{2 \cdot P_i \cdot b_{n,max}}$$

Equation 34

In this equation, j_f is the final rotational angular momentum, P_i is the incident momentum of the colliding atom, and $b_{n,max} = A - B$ is the difference between the major semiaxis A and the minor axis B of the ellipse and is related to the anisotropy of the interaction potential. The rotational rainbow angles increase with increasing rotational angular momentum transfer, $\Delta j = j_f - j_i$, and under the experimental conditions used, the initial angular momentum j_i is small and thus can be neglected. As is shown in Figure 44, by adjusting the anisotropy of the ellipse (i.e., $b_{n,max}$), the predicted rainbow angles can be made to match closely the rainbow angles observed experimentally for high j'_{NO} . Moving to lower j'_{NO} , the two-dimensional hard ellipse model increasingly fails to capture the observed angles, particularly for j'_{NO} = 7.5 and 8.5. This is suspected to be a consequence of increased sampling of the attractive part of the potential energy surface. The value of $b_{n,max}$ used for this comparison is 0.34 Å, which nearly equals the average experimental value of $b_{n,max}$= 0.32 Å for the NO + Ar system.[5]

Images for j'_{NO} = 7.5 and 8.5 from NO collisions with CH_4 show strong scattering into the 0−10° range which may arise from attractive forces between the collision partners. Although the role of attractive forces in rotational energy transfer has received less attention than collisions dominated mainly by repulsive forces, it is known that the existence of an attractive well in the PESs may give rise to an L-type rainbow. The occurrence of an L-type rainbow is manifested as an interference pattern at relatively small scattering angles.[230] The scattering angle is 0° for glory scattering, corresponding to an impact parameter for which the attractive and repulsive forces acting on the scattered particle balance perfectly.[18] As the impact

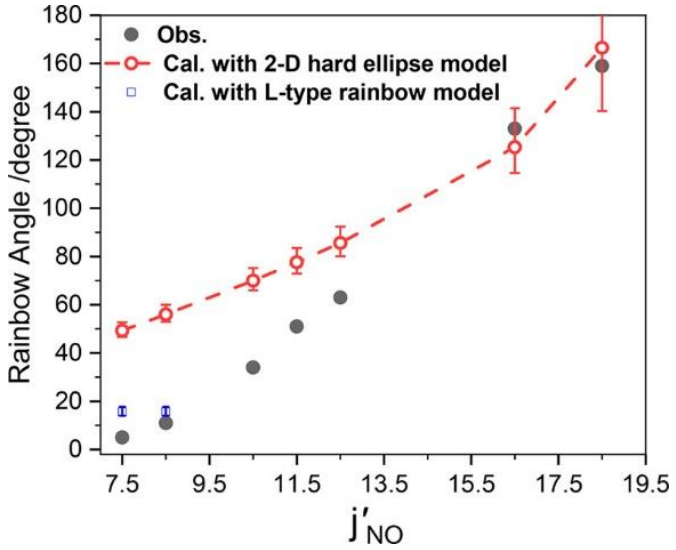

Figure 44: Observed (solid black circles) and calculated (open red circles) dependence of rotational rainbow angles on final rotational level j_{NO}' for NO scattering from CH_4. Blue squares represent angles calculated with the L-type rainbow model. The error bars are obtained by taking the spread of collision energies into account.

parameter increases further, the attractive part of the potential is sampled more heavily than the repulsive part, giving rise to a non-zero but small scattering angle, which is the classical mechanism of an L-type rainbow.[24] Quantum mechanically, the L-type rainbow originates from partial waves with total angular momentum J higher than that of the glory partial wave. As is explained in Section 5.1, L-type rainbows are most evident for low Δj_{NO} transitions.[26] The purely repulsive two-dimensional hard ellipse model cannot account for the maxima observed at small forward scattering angles for these lower final j'_{NO} products, and therefore it is proposed that the strong scattering into the 0−10° range can be attributed to L-type rather than rotational rainbows.

Within an L-type rainbow model, the angle θ_L at which the L-type rainbow is expected for inelastic scattering of a rare gas atom with a diatomic molecule can be approximated by[26, 224]

$$\theta_L = 2\frac{\varepsilon}{E_{coll}}$$

Equation 35

where ε and E_{coll} are the average well depth of the PES and the collision energy, respectively. In contrast to the rotational rainbow, the L-type rainbow scattering only depends on the system and the collision energy and not on the rotational excitation of the scattered molecule.

Using the minimum (114.4 cm^{-1}) of the isotropic potential as the average well depth, the position of the L-type rainbows θ_L predicted by this model for NO + Ar scattering is 14° at a collision energy of 730 cm^{-1} for Ar + NO ($^2\Pi_{1/2}$, j = 1/2) $\rightarrow$ Ar + NO ($^2\Pi_{1/2}$, j' = 3/2 and 5/2).[26] The average well depth of the PES for CH_4– NO van der Waals complexes is 95.5 cm^{-1} ; [242] hence, the L-type rainbow angle θ_L calculated with Equation 35 for the NO + CH_4 system is 15.6° under our experimental conditions. As is shown in Figure 44, this predicted rainbow angle is in reasonable agreement with the measured angles of 4 and 11° for NO in final rotational states of j'_{NO} = 7.5 and 8.5, respectively. Although not quantitatively predictive, the two-dimensional hard ellipse model and the L-type model offer qualitative and valuable insights into the origin of structures in the quantum state-resolved DCSs.

5.3.2. Rotational Excitation of CH_4 Co-Products.

The analysis of experimental velocity-map images for the scattering of diatomic NO from a polyatomic molecule such as CH_4 is more complicated than the analysis of collisions of NO with rare gas atoms because of the possibility of change of the internal energies of both the NO and its molecular collision partner. However, the analysis of the images potentially provides rich information about pairwise correlations between the final rotational levels of the two molecules involved in collisions, in this case the (j'_{NO} , j'_{CH4}) correlation. Since both the NO and CH_4 molecules can undergo rotational excitation during the collision, the experimental image for a specific final rotational level of NO, which is state-selectively detected in the REMPI scheme, is a sum over the scattering for all the rotational states of co-product CH_4 populated in coincidence. Within the NO images, the rotational excitation is observed as a series of concentric rings, corresponding to the Newton spheres for the scattered CH_4 co-products in different final j'_{CH4} states but overlapping because of the experimental resolution. The radial size of a NO image is proportional to the CM frame speed of the scattered NO. This radial size decreases with increasing j'_{CH4} according to the kinetic energy available to the NO molecule after partitioning the initial collisional and internal energies into both NO and CH_4 post-collision rotational excitation (E'_{rot}).

The total translational energy of the two products, $E_t = E_{coll} - \Delta E_{rot}$, is a function of both NO and CH_4 pre- and post-collision rotational energies because the change in the rotational energy from the collision, $\Delta E_{rot} = E'_{rot} - E_{rot}$, contains contributions from both NO and CH_4. The

initial rotational energies of the NO and CH_4 molecules, E_{rot}, are those of the rotational levels of the NO and CH_4 molecules populated in the molecular beams. As described in section 5.2, about 90% of NO molecules are in $j_{NO} = 0.5$. Due to the expansion of neat CH_4 molecules to form the second molecular beam, the initial conditions of CH_4 molecules are not as well controlled: it is estimated that 31% of the CH_4 molecules are in $j_{CH4} = 0$, 56% in $j_{CH4} = 1$, and 13% in $j_{CH4} = 2$ based on work by Buck et al.[233] An ion image can be blurred by the spreads in the initial velocity and angular distributions of the two molecular beams, together with the distribution of populations of rotational levels of the CH_4 molecules, which together cause an overlap of the scattered NO Newton spheres, leading to a broad distribution of NO speeds from the image analysis. Comparison of the radial widths of features in NO images from scattering with Ar demonstrates that much of the broadening can be attributed to the rotational excitation of CH_4 co-products. The mean collision energy for the CH_4 + NO system is 700 cm^{-1} with a full width at half-maximum (fwhm) of the distribution of 80 cm^{-1}. Within the principles of energy and linear momentum conservation, the rotational energy of the co-product CH_4 is determined by

$$E_{rot}(\mathrm{CH_4})' = E_{coll} - E_t' - E_{rot}(\mathrm{NO})' + E_{rot}(\mathrm{CH_4}) + E_{rot}(\mathrm{NO})$$

with primes denoting product properties. Here, E'_t is the total translational kinetic energy of both scattered products, and other terms have been defined earlier. E_{rot} for each species is considered to be that of its most populated energy level (i.e., $j_{NO} = 0.5$ and $j_{CH4} = 1$).

Since CH_4 is a spherical top with a rotational constant of 5.2412 cm^{-1},[243] the rotational energy levels of CH_4 can be estimated directly from a given product translational energy measurement. In Figure 45, CH_4 product rotational level assignments are superimposed onto total translational energy distributions obtained for the scattered NO product rotational levels of $j'_{NO} = 7.5$, 11.5, 13.5, and 18.5. Total translational energy distributions are obtained by integrating over all CM frame scattering angles. Because of the additional noise introduced by the FINA method, especially below $E'_t \sim 130$ cm^{-1}, and similar overall profiles for the total translational energy distributions obtained from unreconstructed and reconstructed images, the total translational energy distributions obtained from the unreconstructed images are preferred for this analysis.

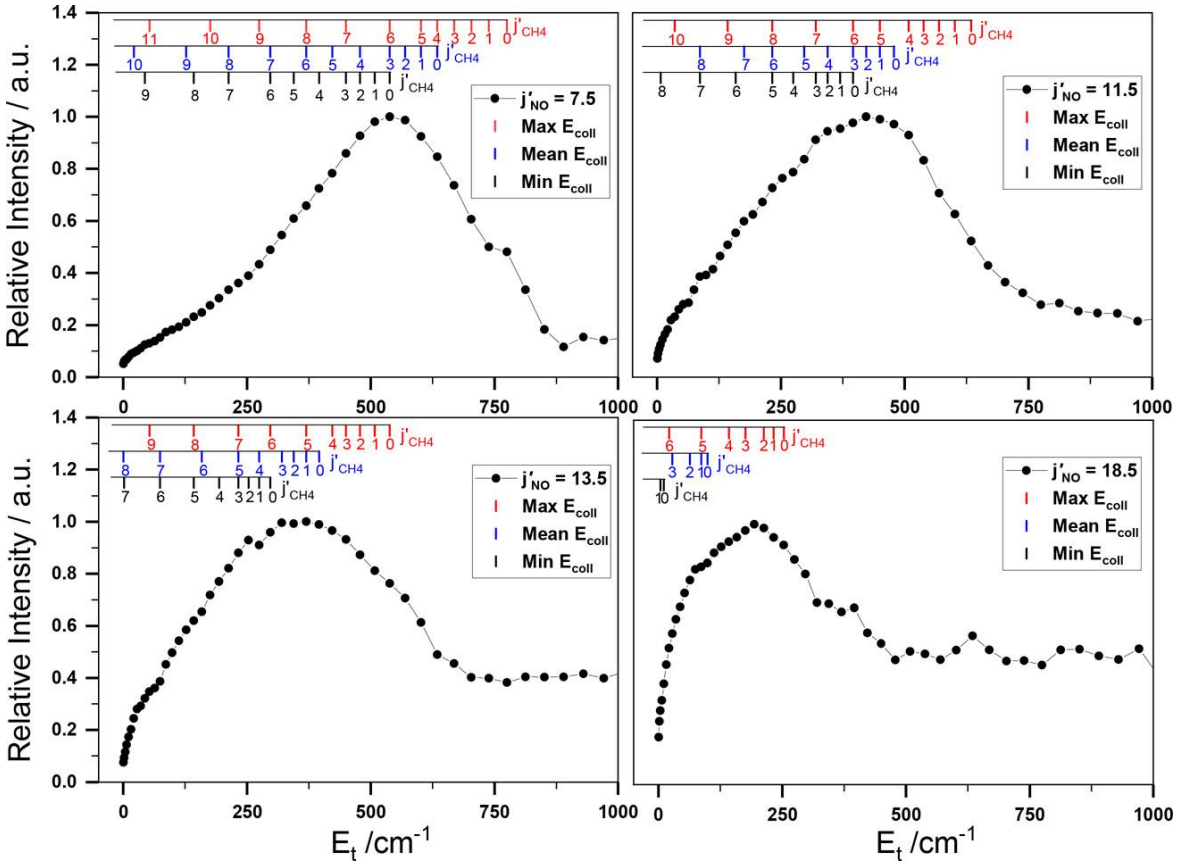

Figure 45: Total translational energy distributions of the scattered NO + CH_4 collision products, obtained by integrating over all CM-frame scattering angles for j_{NO}' = 7.5, 11.5, 13.5, and 18.5. Using arguments of conservation of energy and linear momentum, the combs at the top of each panel represent the positions of co-product CH_4 rotational levels estimated with three different collision energies encompassing the experimental spread of 700 ± 80 cm^{-1}.

The corresponding plots for j'_{NO} = 8.5, 10.5, 12.5, and 16.5 are given in Figure 45. As mentioned previously, the ±80 cm^{-1} spread in collision energies places some uncertainty on the derivation of the rotational level j'_{CH4}. Hence, the most populated final rotational levels j'_{CH4} were estimated for the three cases of minimum (620 cm^{-1}), mean (700 cm^{-1}), and maximum (780 cm^{-1}) initial collision energies. Even using the maximum collision energy to estimate the rotational level assignments for CH_4, a small part of the measured high total translational energy distribution cannot be assigned. It is possible that CH_4 and NO molecules with higher pre-collision rotational or vibrational energies, present because of imperfect cooling in the molecular beams, give rise to this higher energy component.

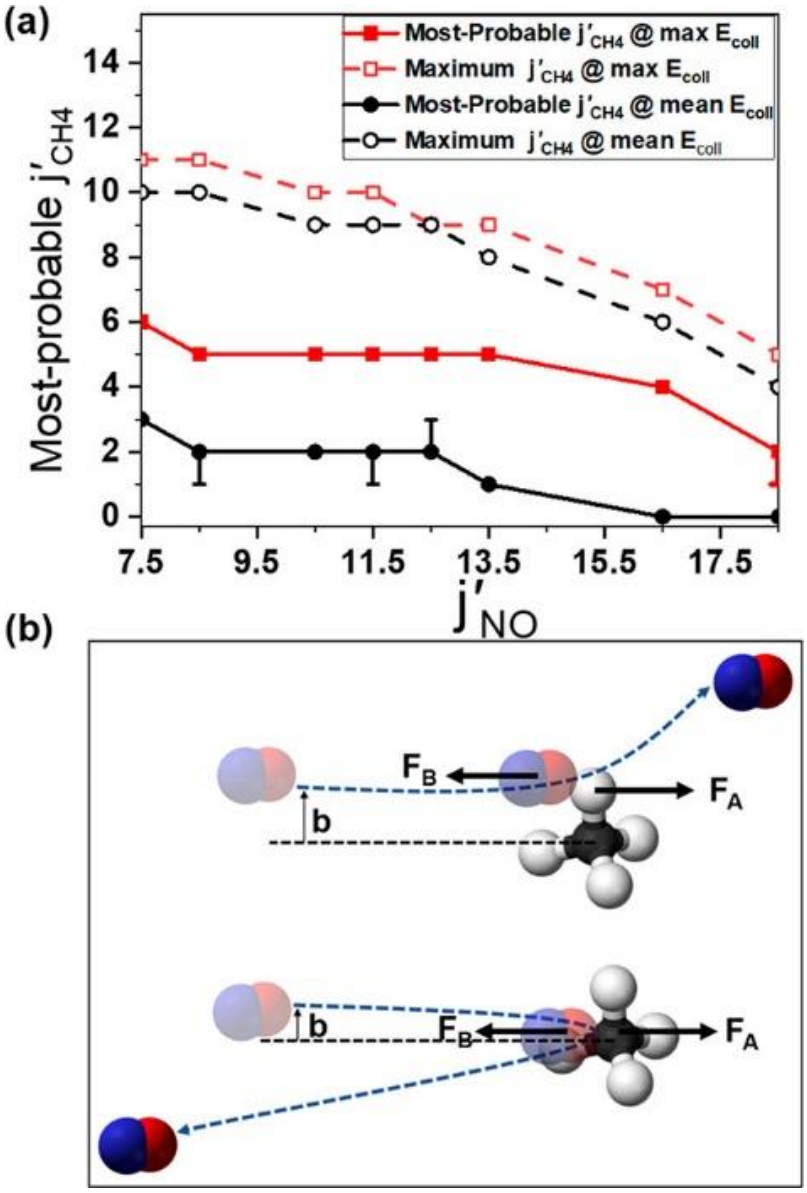

Figure 46: Dependence of rotational excitation of the co-product CH_4 on the final rotational level of NO. (a) Most-probable j_{CH4}' values for each partner j_{NO}' deduced from analysis of the radial intensity dependence of scattered NO velocity-map images. The j_{CH4}' values were determined from the rotational level assignments corresponding to peaks in the translational energy distributions shown in Figure 45. The error bars are obtained by taking the uncertainty of peak position in the translational energy distributions into account. Dashed lines show the predictions for maximum rotational excitation accessible on energy conservation grounds. Black and red points and lines correspond to data analysis using the mean (700 cm^{-1}) and maximum (780 cm^{-1}) experimental collision energies, respectively. (b) Schematic diagram for the mechanism of rotational excitation of the co-product CH_4. The NO and CH_4 molecules approach each other with different impact parameters b, and interact with repulsive forces F_A and F_B, generating different torques on the CH_4.

Furthermore, Figure 45 focuses on the most probable rotational levels j'_{CH4} , corresponding to the peaks in the total translational energy distributions. The most probable j'_{CH4} values deduced using the mean (700 cm^{-1}) and maximum (780 cm^{-1}) initial collision energies are shown in the upper panel of Figure 46. It should be noted that at the minimum collision energy, co-product CH_4 cannot be rotationally excited according to energy constraint arguments. As the rotational excitation of the detected NO molecule increases, the overall trend of the most probable j'_{CH4} value decreases for j'_{NO} values from 7.5 to 18.5, but it remains nearly constant in the j'_{NO} range from 8.5 to 13.5. This trend suggests that a higher Δj_{NO} for the scattered NO correlates with a lower Δj_{CH4} of coproduct CH_4, corresponding to a product−pair anticorrelation of rotational excitation in this bimolecular scattering. In other words, the warmer j'_{NO} , the colder j'_{CH4}.

In Figure 46a, the black and red dashed lines represent the maximum accessible rotational levels of CH_4 deduced by assuming that all the collision and initial internal energies are transferred into rotational energies of both scattered products. The maximum j'_{CH4} values shown by the dashed lines are consistently larger than the most probable j'_{CH4} values deduced for the same j'_{NO} values from the experiments. Therefore, this product−pair anticorrelation of rotational excitation is not driven by energy constraints. Figure 46b proposes a classical explanation for the observed trend of anticorrelation of rotational excitation of the NO and CH_4 products. Equal and opposite forces act on the atoms when two molecules approach most closely (see the lower panel of Figure 46), independent of whether the forces are attractive or repulsive. For collisions with large impact parameter, CH_4 molecules experience a large torque because the centre-of-mass of the molecule is on the C atom, resulting in excitation of higher CH_4 rotational levels. The partner NO is forward-scattered and experiences lower rotational excitation than collisions at lower impact parameters which sample more of the repulsive potential. However, for these collisions with small impact parameters, smaller torques on the CH_4 molecules lead to low or no rotational excitation, whereas the partner NO is backward-scattered and rotationally excited by the repulsive interaction. In other words, collisions at the central C atom do not induce rotational excitation of CH_4, whereas collisions at a peripheral H atom do. These arguments apparently conflict with reports of positively correlated product rotational excitations in diatomic−diatomic molecule inelastic collisions.[107, 210-212] However, the opposing correlations may arise from differences in the

physical shapes of methane (a spherical top) and linear molecules. Further theoretical work is required to provide a more quantitative understanding of the rotationally inelastic scattering dynamics of NO with CH_4, and in particular, this rotational anticorrelation in the product pairs. Theoretical simulations are currently impeded by the lack of a global PES for the NO + CH_4 system and the complexity of the diatomic + polyatomic molecule scattering dynamics.

5.4. Conclusions

This chapter reports the observation of rotational and L-type rainbows in the rotationally inelastic scattering of NO with CH_4 at a collision energy of 700 ± 80 cm^{-1} . Although a detailed comparison with scattering calculations on a global potential energy surface is not yet possible, classical models provide valuable insights for this inelastic scattering of the two molecular species. The measured NO quantum-state-specific DCSs will provide a stringent test for the quality of future potential energy surfaces and for any approximations of reduced dimensionality applied to quantum scattering calculations for the NO + CH_4 system. The high Δj_{NO} scattered products appear to be correlated with low Δj_{CH4} co-product CH_4 molecules, which indicates a product−pair anticorrelation of rotational excitation in this bimolecular scattering.

6. Progress Towards VMI of Crossed Beam Reactive Scattering of Methane with Cyanogen Radicals

Contributions:

This work was performed using the same crossed molecular beam apparatus as for the NO + CH_4 scattering studies, with additional adaptations to introduce photolysis at one of the pulsed nozzles. These adaptations were based on the designs of Dr Ondřej Tkáč and Dr Stuart Greaves (implemented in a different VMI apparatus), with further design, construction and testing performed by the author of this thesis with Dr Patrick A. Robertson and Dr Xu-Dong Wang. These three researchers also jointly carried out preliminary data collection and analysis. Further developments were then primarily the work of the author of this thesis, with assistance from Dr Patrick A. Robertson. The work was completed under the supervision of Prof Andrew J. Orr-Ewing.

6.1. Introduction

The reactions between hydrogen-containing species and cyanogen radicals (CN) have been extensively studied. As well as being relevant in the interstellar medium,[244] these reactions are of interest in fuel combustion, where HCN is a precursor to NO, leading to extensive studies of the elevated temperature rate constants.[245-247] Hydrogen abstraction reactions by CN radicals are also of interest as analogues of halogen atom reactions, due to the similar reactivity and electron affinity of CN relative to halogen atoms, but with the added complexity of CN rovibrational energy levels and the loss of spherical symmetry.[248, 249]

The kinetics of the reactions of cyanide with hydrogen[250-252] or hydrocarbons[246, 253-255] have been extensively studied. State-resolved VMI studies have been performed for reactions involving larger hydrocarbons,[248] but such investigations have not previously included methane. The dynamics of the reaction of methane with CN radicals have been computationally simulated in previous work from the Bristol group using a global potential energy surface.[249] This reaction differs from those of CN with larger hydrocarbons by having a small potential energy barrier.[254] However, the reaction is attractive to detailed dynamical study because the well-known REMPI schemes for methyl radicals can be used in combination

with VMI to probe the correlated vibrational quantum state populations of both products.[256] In principal, complete quantum state specific information can be experimentally determined for the products.

A key step in the study of these reactions is the reliable production of a molecular beam of CN radicals. Multiple routes of production exist, with prominent examples being the photolysis of cyanogen (NCCN),[246, 247, 253, 255, 257, 258] cyanogen iodide (ICN),[250, 258] cyanogen bromide (BrCN),[248, 257, 258] or cyanogen chlorine (ClCN),[257] or through applying an electric discharge to these species.[259] Photolysis can be performed using either the 4th Harmonic (266 nm) of a Nd:YAG laser, or the 193 nm emission of an ArF excimer laser. These species dissociate by different pathways, resulting in significant differences in the rovibrational distribution of the product CN.[257]

Below 225 nm, the absorption spectrum of cyanogen consists of structured vibronic peaks,[260, 261] consisting of excitation from the ground $^1\Sigma_g^+$ state to the excited $^1\Sigma_u^-$ and $^1\Delta_u$ states, both of which may contribute to the 193 nm photolysis.[262-264] This photoexcitation produces a ratio of vibrationally excited cyanogen radicals, relative to vibrationally ground state CN, of 0.35, with minimal CN produced for v''=2 and above. The resultant CN rotational distribution is observed to mirror that of the parent cyanogen, with each radical receiving half the rotational energy of the parent.[264]

Cyanogen Halide absorption in the same region consists of broad bands, with the species undergoing photolysis by either an A-band or α-band pathway via a Rydberg continuum. The heavier halides have these bands systematically shifted to longer wavelength, with the peak of the A-band occurring at 177.6, 201.6 and 251.3 nm in ClCN, BrCN and ICN, respectively. To shorter wavelengths, the α-band begins at around 170, 180 and 210 nm in the three species respectively.[261, 265]

ClCN cannot be photolyzed at 266 nm, instead requiring 193 nm photolysis to excite via the A-band. The dissociation produces predominantly vibrational ground state CN, with progressively less in the v=1 and v=2 vibrational states. An inverted rotational distribution supports the conclusion of the excited state favouring a bent geometry.[266]

BrCN undergoes photolysis via the A-band at both 266 and 193 nm. A key difference between photolysis at each of these two wavelengths is that spin-orbit excited Br (hereafter Br*)

cannot be produced at wavelengths longer than 248 nm, whereas it is observed to be the predominant product below 242 nm. An increased proportion of vibrationally excited CN radicals is also observed at higher wavelengths. It has been suggested that this behaviour mirrors the initial BrCN vibrational levels, and that vibrationally excited BrCN has improved Franck-Condon overlap with the electronically excited state, resulting in more prominent excitation at the long-wavelength end of the absorption band. As with ClCN, an inverted rotational population is consistently observed. [266-268]

ICN can be photolyzed at 266 or 193 nm. At 266 nm, CN is produced almost wholly in the ground vibrational state. Some increased rotational energy is observed, with a more complex distribution than lighter cyanogen halides. However, it has been established that low rotational state ICN produces low rotational state CN. This behaviour, which differs from BrCN and ClCN, is thought to be the result of a smaller bending angle in the excited state minimum, and hence lesser torsion on the molecule. Roughly two-thirds of the product iodine atom is produced in the spin-orbit excited state. [267, 269, 270] Dissociation at 193 nm, in contrast, produces a pure Boltzmann distribution in the CN rotational energy levels, resulting in an assignment of a purely linear excited state. This is along with sole production of spin-orbit ground state Iodide radicals and ground vibrational state cyanide, both of which are likely to be due to energy availability.[271]

CN does not have a known REMPI detection scheme, instead needing either IR spectroscopy,[253] or Laser Induced Fluorescence (LIF) detection in the near-UV[246] to probe its formation. As such, it is common not to detect this species directly in reactive scattering experiments. Instead its production is presumed from the observation of the halogen cofragment, and the rovibrational properties presumed to follow those established in the above prior work for whichever parent species is used.[248, 257]

This chapter presents developments made towards the study of the reaction of cyanide radicals with methane utilising VMI. This work builds on previous experimental work performed by others in the Bristol laboratory.[249] Significant progress was made, although no reactive scattering was observed. As such, this Chapter describes and documents the progress made to support further research.

6.2. Experimental Details

This experiment used the VMI chamber apparatus described previously (Chapter 2). Of note in these experiments was the development of the photolysis capability to generate a radical beam, which consisted of an apparatus attached to one nozzle capable of directing a laser beam across the nozzle face and back out of the chamber. This return path was intended to be used to confirm alignment. Most of the results presented in this chapter were achieved using a pair of right-angled prisms (Thorlabs, UV fused silica) mounted either side of the faceplate and combined with a 40 cm focusing lens mounted outside the chamber. This prism apparatus is based on earlier work performed by Dr Ondřej Tkáč and Dr Stuart Greaves, and reported in Dr Tkáč's PhD Thesis.[100]

Prior to implementation of the design outlined above, experiments were attempted using a pair of right-angled parabolic mirrors (Thorlabs, UV-Enhanced aluminium coating), with a focal length of 15 mm, each offset by 12 mm either side of the nozzle aperture. These mirrors suffered from deposition of a contaminant (potentially the cyanogen precursor), which subsequently burned and damaged the mirrors on exposure to the photolysis laser. As such, the mirrors required frequent cleaning which was disruptive to the progress of the experiment. This problem was solved by replacing them with right-angle quartz prisms.

Cyanide radicals were ultimately produced through the 193 nm photolysis of BrCN, excited via the A-band discussed above. The laser source for photolysis was an Argon – Fluorine excimer laser (Lambda-Physik OPTex). The BrCN sample was loaded into an inline trap in the vacuum line before a pulsed nozzle, and held in place with glass wool plugs. Argon carrier gas (0.6 bar backing pressure) was passed through this sample to deliver it to the high-vacuum chamber via a General Valve nozzle directed perpendicular to the time-of-flight axis. A second nozzle, perpendicular to both the first and the time-of-flight axis, was available to produce the methane molecular beam. However, no data reported here were acquired with this in use.

The 193-nm photolysis of BrCN was concluded to be the optimum technique for CN production after having tested both ICN and BrCN precursors, and having tried photolysis of each at 266 nm. This 266 nm radiation was produced by the 4th harmonic of a Nd:YAG laser (Surelite SLIII-10). Early work at 266 nm was hampered by either ICN's low room temperature

vapour pressure of 1.3 mbar,[272] as contrasting to 160 mbar for BrCN,[273] or BrCN's reduced absorption cross section at 266 nm of around 3 x 10^{-21} cm^2 $molecule^{-1}$,[268] as contrasting to around 3 x 10^{-19} cm^2 $molecule^{-1}$ for ICN.[270] Since, at constant volume and temperature, the number of molecules of gas produced is expected to be proportional to the vapour pressure, the two orders of magnitude difference in each of these quantities is expected to result in similar yields of photolysis products, which proved too low for further use. At 193 nm, both species have absorption cross sections around 3 x 10^{-19} cm^2 $molecule^{-1}$,[265, 268, 270] so the higher vapour pressure of BrCN makes it the preferred species to use.

Due to the absence of LIF detection capability in the VMI apparatus, cyanogen radical production had to be inferred from detection of the halogen cofragment, following REMPI ionisation. Br^+ was detected at 260.61 nm (via the 2-photon $^2P_{3/2} - 5p^4D_{3/2}$ transition) and 266.633 nm (via the 2-photon $^2P_{3/2} - 5p^4P_{3/2}$ transition),[104] with earlier work on ICN using I-atom REMPI at 265.91 nm (2+1 REMPI via the $^2P_{1/2} - (^3P_2)7p[1]_{1/2}$ transition).[105] The REMPI wavelength was created by frequency doubling in a BBO crystal the output of a tunable pulsed dye laser (Sirah model PRSC-G-24, using Coumarin 540A dye) pumped by the third harmonic of a Nd:YAG laser (Quanta Ray GCR 200) operating at 10 Hz. The laser source was loosely focused into the chamber by a 50 cm lens.

Methyl radicals were planned to be detected with (2+1) REMPI at 286.26 nm, via the Q branch of the $4p_z^2\ A_2'' \leftarrow \tilde{X}^2A_2''$ transition.[106] This wavelength was produced by the same dye laser system as above, however utilising Rhodamine 6G dye and the second harmonic of the Nd:YAG laser.

Methyl Iodide photolysis was also tested. This species was introduced by application to the glass wool plugs in the inline trap, with methyl product detected by the same scheme as above. This work was intended to allow characterisation of the photolysis-side molecular beam under the same laser system arrangement used for probing methyl radicals. Methyl Iodide absorbs at wavelengths around 192.3 nm, accessible via the emission from an ArF excimer laser; this excitation is assigned as the Q-branch of the v_2^1 excitation within the $A_1 \rightarrow E$ Rydberg state electronic transition.[274, 275]

a)

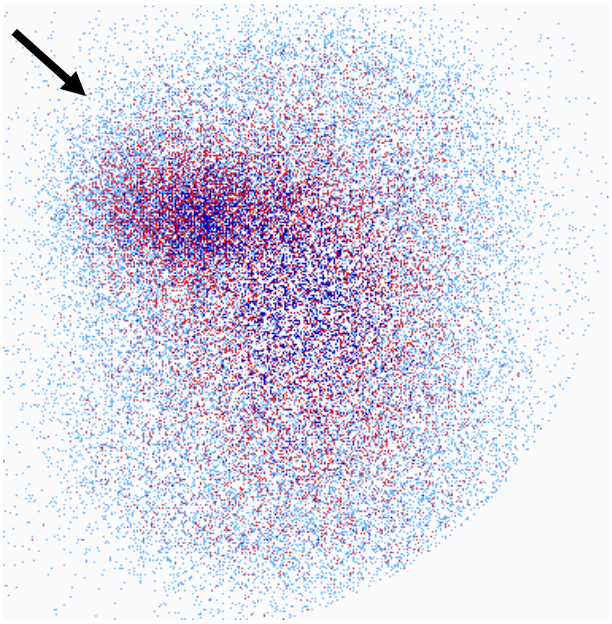

b)

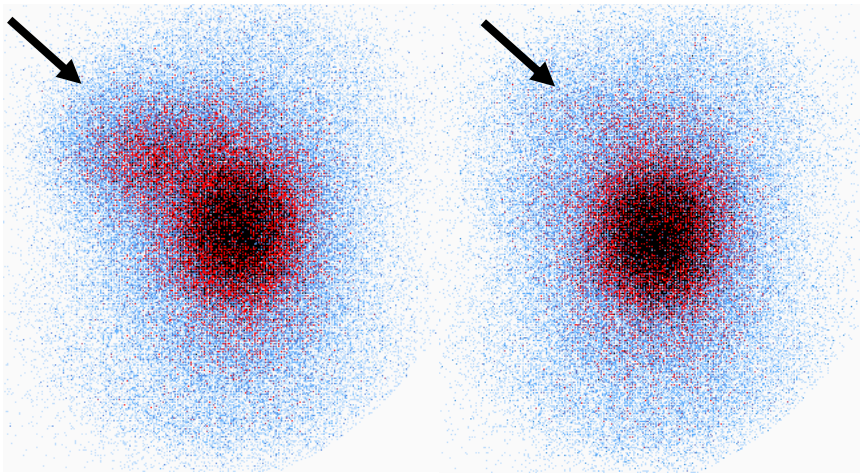

Figure 47: Raw VMI Images of Iodine atoms from ICN, detected at 265.91 nm. (a) is after shot-to-shot subtraction of images acquired with 266 nm photolysis laser on (b, left) and off (b, right). The probe laser is polarised vertically in the plane of the image. The cut off in the lower-right of (a) is the edge of the phosphor screen. The Iodine velocity vector is shown by the black arrows.

6.1. Results and Discussion

The first successful production of cyanogen radicals, evidenced by halogen cofragment signal increasing when using the photolysis laser, occurred with the 266 nm photolysis of ICN, and utilised the parabolic mirror apparatus. Example images are shown in Figure 47. The signal produced involving the photolysis laser is observed as a secondary peak, at a reduced radial distance than the more intense signal produced by the probe laser alone.

a)

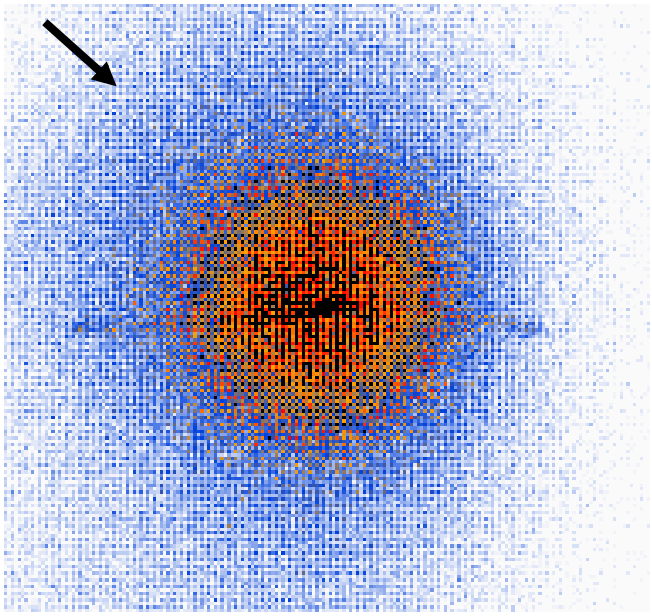

b)

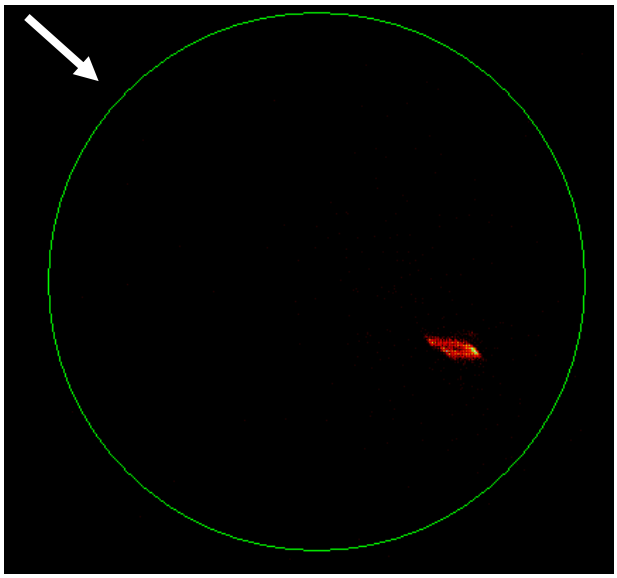

Figure 48: Raw VMI images of Br atoms from 193 nm photolysis of BrCN. (a) image taken with 193 nm photolysis and 266.633 nm REMPI probe. (b) preliminary image taken with 266 nm photolysis and 260.61 nm probe. The green circle is an artefact of the detection software. In both cases the probe is polarised vertically in the plane of the image. The molecular beam axis is shown by the arrow in each picture.

Photolysis of BrCN in the nozzle expansion produced VMI images as shown in Figure 48. Panel (a) of this figure shows results using 193 nm photolysis and 266.63 nm REMPI detection of Bromine (this REMPI wavelength was used at this point to reduce 1-colour signal compared to excitation at wavelengths around 260 nm). Although this REMPI detection scheme measures ground-state bromine atoms, which are predicted to be a more minor product at this photolysis wavelength, high ion counts were observed. These counts often exceeded 100 ions per laser shot, so little effort was made to find Br* signal. The 1-colour (probe UV light

only) and 2-colour (photolysis and probe wavelengths) signals overlapped, in contrast to the separate groupings observed from ICN above. The bar visible through the image is of unclear origin. It was suspected to be caused by a degree of spatial mapping, but could not be improved by adjustment of the ion optic voltages.

Figure 48b shows earlier, preliminary work using 266 nm photolysis and 260.61 nm REMPI probe. Much lower signal levels were observed, as expected from the reduced absorption cross section of BrCN at 266 nm. As such, the much smaller velocity spread of the signal suggests that Figure 48a may be being blurred by space-charge effects resulting from REMPI detection of a much higher Br-atom density.

The signal produced by both the photolysis and probe lasers relies on three timing metrics- the opening of the pulsed valve nozzle producing the molecular beam, the timing of the photolysis laser to coincide with the release of a gas pulse from the nozzle, and the timing of the probe laser to coincide with the halogen product having reached the VMI optics region. The timing characteristics of these three steps were carefully characterised for the case of BrCN photolysis. Since the firing of the probe laser was used to define the zero of time in time-of-flight and VMI measurements, this involved moving either the time of opening of the pulsed valve which generates the molecular beam, the photolysis laser timing, or both synchronously, and tracking Br atom signal levels. With a pulsed molecular beam duration with width of 160 μs (which was confirmed by changing the valve opening timing, with constant timings for both lasers), and working from maximum signal, the width of the bromine atoms produced by photolysis was observed to be around 14-15 μs. This was demonstrated by either moving the photolysis laser, with constant valve and probe timings, or moving the photolysis laser and valve timings together, with constant probe timings. In each case, the timings could be moved 7-7.5 μs before signal was lost.

The increase in signal intensity relative to that produced by only the probe laser was also recorded as a function of photolysis laser energy. This was found to be described by a quadratic function, of the form:

$$Intensity = A \cdot Energy + B \cdot (Energy)^2$$

In this case, the coefficient 'A', relating to the proportion of signal coming from a one photon photolysis process, was found to be around 8 times larger than 'B', which would relate to two

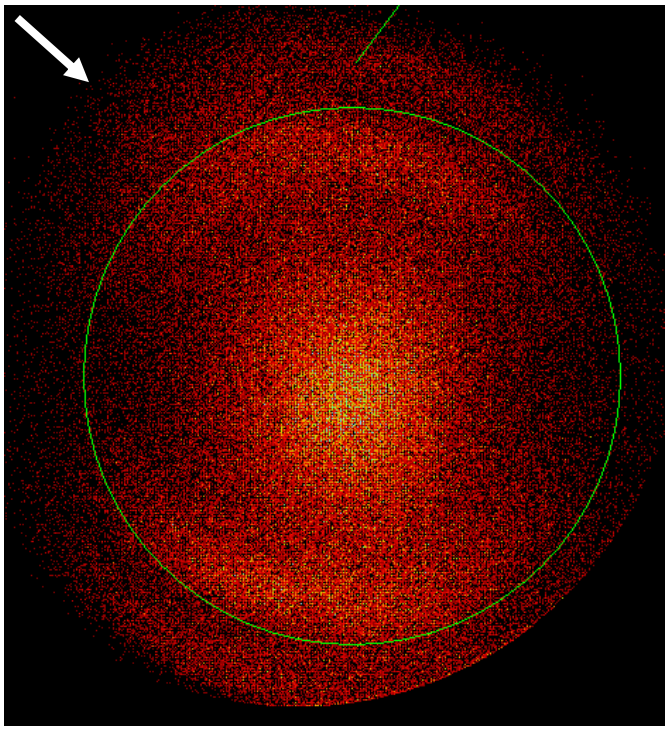

Figure 49: 1-colour methyl signal from methyl iodide, detected at 286.26 nm. The probe laser is polarised vertically in the plane of the image. The green markers are artefacts of the detection software. The molecular beam axis is shown by the white arrow.

photon processes. This signal dependence on photolysis laser pulse energy confirms mostly one-photon photolysis via the A-band.

The final experiment performed was the detection of methyl fragments from methyl iodide to confirm that the apparatus was correctly set up for methyl radical REMPI detection. This was a necessary precursor to attempts to image the methyl radicals from the bimolecular CN + CH_4 reaction. Methyl radical signals were successfully produced by the 286.26 nm probe laser alone, as shown in the preliminary image depicted in Figure 49. This image is comparable to previous studies of CH_3I photoexcitations, which report a weakly anisotropic central feature assigned to dissociative ionisation of the parent molecule, and anisotropic outer rings with preferential parallel recoil assigned to photodissociation of the methyl iodide via the A-band.[276, 277] No 2-colour signal was found before the conclusion of the experimental studies, precipitated by laboratory closure because of the 2020 Covid-19 pandemic.

6.2. Conclusion

This chapter reports progress towards VMI studies of the reaction between methane and cyanogen. Although no reactive scattering was observed, the experimental studies performed

established a reliable source of cyanide radicals from the photolysis of cyanogen bromide. The absence of a REMPI scheme for CN radical detection is a hindrance to further progress, but REMPI detection of the bromine atom co-fragment of BrCN photolysis provides an alternative method for optimization of the molecular beam of CN radicals needed for the bimolecular reaction studies.

7. Conclusions

This thesis firstly describes further computational studies of the reaction of propene with chlorine atoms. Secondly this thesis reports development of a crossed molecular beam scattering apparatus, and a series of investigations performed at each stage of the development of the apparatus. These investigations began with unimolecular photodissociation experiments of 2,4-dibromofluorobenzene (DBFB), followed by bimolecular collision experiments involving the inelastic scattering of NO with methane. Finally, this bimolecular capability is developed towards the reactive scattering of cyanogen radicals with methane. This chapter sums up the conclusions drawn from each of these investigations, as well as indicating the next steps for each of these topics.

The computational studies presented in this work progressed from an earlier study of the Cl + propene reaction by Hornung *et al.*, which covered the development of an empirical valence bond (EVB) global potential energy surface (PES) to describe the system and investigated the importance of three types of intermediates through quasi-classical trajectory (QCT) studies.[51] The present work describes the impact of collision energy on the characteristics of both the reaction and the products, similarly through QCT simulations on the same global PES.[278] It was firstly found that the rovibrational level population distribution of the HCl products was invariant with respect to collision energy. Encounters initiated at larger impact parameters became reactive at lower collision energies, with a preference for forward-scattering at higher collision energies progressing more isotropic scattering at lower collision energies. This change in preferred scattering angle came alongside an increased proportion of longer-lived trajectories at lower collision energies (30% of trajectories last longer than 1ps at 7 kJ mol^{-1}, compared with 14% at 14 kJ mol^{-1} and 7% at 28 kJ mol^{-1}). This increase in trajectory time explains the observed, more isotropic, scattering distribution through rotational averaging.

The long-lived trajectories were analysed based on the proportion of time spent in selected regions of the PES. These regions included those associated with approach of the chlorine and departure of hydrogen chloride, and identification of times where the chlorine becomes distant (beyond the attractive regions of the potential) during the trajectory, alongside three more identified by Hornung *et al*.'s work. These three regions corresponded to 1- or

2-chloropropyl radicals, and where the chlorine was interacting with the larger potential well around the π system on the double bond. This interaction with the π system is a feature associated with roaming trajectories, however not all passages through this region will be roaming. As such the proportion of time spent in this π region is a proper superset of the time spent in a roaming trajectory.

The proportion of time spent in each one of these regions did not change significantly between collision energies. The 1-chloropropyl radical was shown to be responsible for a substantial majority of the time spent in long-lived trajectories (78 - 80%), with the 2-chloropropyl radical accounting for 2.5 - 7%. The time spent in the π potential well was around 10% of the total time, and the chlorine was temporarily distant for around 3 - 4.5% of the time.

Further characterisation of the time spent in the region where roaming may occur found that much of this time consisted of short-lived periods between longer times spent in the 1-chloropropyl potential well. As such, this time would be better described as a high vibrational mode of the C-Cl bond in the chloropropyl radical than as roaming. After setting a lower limit for the roaming time at 75 fs, the fraction of time spent in assignments that could be roaming dropped to only 2.5% at 14 kJ mol^{-1}. Hence roaming is not expected to be a significant pathway in the reaction of chlorine atoms with propene. However, further studies could investigate the intervals where the chlorine atom remains in the π region for over 75 fs, to identify if roaming trajectories do occur in the system.

The significance of this study of the reaction of chlorine atoms with propene has been discussed in papers by Suits and co-workers, both in the context of experimental work on the reaction of chlorine atoms with isobutene,[279] and in a review paper on roaming.[122] In the latter, an argument is made that roaming could occur within 75 fs based on this being observed with H atom roaming in formaldehyde. However, this argument can be rejected based on considering the increased mass and size of Cl atoms compared to hydrogen atoms, along with the lower energies involved in the present work.

Alongside the computational studies, experimental work was performed to develop and improve on an apparatus most recently characterised by Dr Pandit in his PhD thesis.[95] This

work developed and characterised an added crossed molecular beam functionality via a new source chamber, with the goal to ultimately study reactive scattering.

Initial work was performed on unimolecular processes to ensure correct performance of the apparatus, before moving on to more complex bimolecular collision systems. This unimolecular work included the first novel study performed using this new source chamber, a characterisation of the UV photodissociation of DBFB to bromine and a bromofluorobenzyl radical. This photodissociation was studied in the 285 – 260 nm absorption band, which is based on an electronic absorption at 281.88 nm. The results extend previous studies characterizing the UV and IR spectroscopy of DBFB by Tripathi and Pandey.[93, 94] A Photofragment Excitation (PHOFEX) spectrum was recorded, alongside VMI images of the resultant bromine atoms. In both cases the bromine atoms were detected via a (2+1) Resonance Enhanced Multi-Photon Ionisation (REMPI) scheme.

The PHOFEX spectrum built on the list of resonances published by Tripathi and Pandey, by demonstrating which regions of the absorption band involve vibrational excitation that promotes the dissociation of a bromine atom. VMI studies observed anisotropic production of bromine atoms, with total kinetic energy release (TKER) substantially below the maximum amount of energy available. The degree of anisotropy, characterized by the β parameter, varied across the wavelengths studied with values from β = 1.3 to 0.5. This variation in β correlated well with the locations of bands in the PHOFEX spectrum, with resonant peaks generally having larger β values, which is indicative of competing dissociation pathways. These pathways consist of one having a high, positive β value (corresponding to prompt dissociation in directions preferentially parallel to the excitation transition dipole moment), and another with more isotropic or negative β values.

These experimental studies of DBFB were complemented by TD-DFT calculations of the vertical excitation energies into the low-lying singlet electronic states, along with optimised S_1 geometries. These studies confirmed that the only low-lying state with large oscillator strength is S_1, with ππ* character and A' symmetry. The S_2 state has πσ* character and A'' symmetry, with zero oscillation strength from S_0. The S_1 optimised geometry has the ortho C-Br bond lengthened by around 0.5 Å and displaced from the plane of the benzene ring by around 30°, whilst the C-F and para C-Br bonds are shortened by around 0.1 Å. The $S_0 \rightarrow S_1$

transition dipole moment is close to parallel to the C-Br bond in the S_0 geometry (i.e. in the Franck-Condon region of the S_1 surface) predicting a β value for this transition of around 1.98. When the geometry relaxes to the S_1 minimum prior to C-Br bond breaking, the displacement of the bromine reduces the predicted β to around 1.33. This reduced value matches well with the maximum experimentally observed anisotropy, leading to the conclusion that the pathway with the larger β parameter involves prompt dissociation from the S_1 state after a degree of relaxation towards the minimum geometry.

By comparison with published work on o-bromofluorobenzene,[168, 169, 177, 183, 280] the anisotropic pathway is assigned to initial excitation to S_1 followed by dissociation along a repulsive πσ* or nσ* pathway. The πσ* pathway would be along the S_2 (A'') electronic energy state. Any distortion of the DBFB molecule out of a planar configuration leads to the S_1 and S_2 states becoming coupled, due to a reduction in the symmetry of the molecule. This coupling results in dissociation along a single adiabatic surface, skirting a conical intersection. The nσ* state is high-lying in the Franck-Condon region, and dissociation via this pathway will only occur if the C-Br bond first deviates significantly out of the plane of the benzene ring.[169] This change in geometry both reduces the energy of the nσ* state and allows mixing, such that this pathway proceeds similarly via a conical intersection. Since the out of plane displacement occurs spontaneously on the S_1 surface, it is unnecessary for specific vibrational modes to be populated to encourage dissociation, so the significance of this pathway to the observed β values is expected to be simply based on the strength of each vibronic transition into S_1.

The smaller β parameters are explained by competition with a second pathway, involving intersystem crossing (ISC) into either a dissociative triplet state or into a bound triplet state at an energy above the dissociation threshold. The alternative option of a dissociation pathway of perpendicular character is considered unlikely, since the S_1 state appears to strengthen the para C-Br bond. Population of a triplet state has been observed to occur from either the S_0 (by UV absorption) or S_1 states in o-bromofluorobenzene, i.e. from either an $S_0 \rightarrow T_2$ excitation process or $S_0 \rightarrow S_1 \rightarrow T_1$. Since the reduction in β is most significant at wavelengths off-resonant with vibronic structure in the $S_0 \rightarrow S_1$ absorption band, the alternative pathway is expected to be predominantly via direct $S_0 \rightarrow T_2$ excitation.

The photofragment TKER values being substantially below the energy maximum can be explained through a combination of the vibrational excitation of the aromatic cofragment in the initial vibronic excitation, combined with the dissociation along an out-of-plane C-Br coordinate. This bond-breaking applies a torque around the benzene ring and hence promotes rotational excitation of the cofragment radical.

Spin-orbit excited bromine (Br*) is a minor product compared to spin-orbit ground state (Br). This unusual outcome is explained by reference to Li *et al.*'s work on o-bromofluorobenzene, which describes the spin-orbit coupling of the system raising the energy of the states which produce Br* significantly above those producing Br.

The next stage of research into DBFB photodissociation dynamics would be ultrafast experimental studies, alongside computational investigations of the excited states using a higher level of theory. The ultrafast studies were envisaged at the start of this project as a collaboration with the Max-Born Institute, and would be able to determine the time constants for the dissociation of bromine. With sufficient time resolution, these time constants could reveal the presence and significance of ISC pathways and skirting of conical intersections. Such time constants might also confirm whether there is time for sufficient geometric distortion for the nσ* pathway to become energetically available. If the nσ* state is energetically unavailable in the relevant timeframe, the parallel pathway can be assigned simply to the S_2 (πσ*) route. Higher level computational studies could also be used to confirm the energy levels of the excited states, and computationally confirm the locations of the crossing points of the S_1 state with the πσ* and nσ* states as a function of the C-Br angle from the benzene plane, assisting in the determination of the dominant pathway. The energies of the low-lying triplet states would also be identified, and assignments of the ISC pathways could then be proposed from the character and energy of these triplet states. Spin-orbit coupled calculations would further confirm the cause of the low yield of Br* product.

Following the completion of the unimolecular dissociation studies of DBFB, experimental work progressed to examining bimolecular scattering processes. Calibration work on the inelastic scattering of NO with argon established the ability of the apparatus to study such bimolecular systems. This bimolecular collision work developed into novel work studying the inelastic scattering of NO with methane[10] which characterised the scattering angle and rotational energy distributions of the products, following inelastic collisions at a collision

energy of 700 ± 80 cm^{-1}. The NO molecules were rotationally cooled using an Argon carrier gas to a rotational temperature of 6 ± 2 K, corresponding to 90% of the molecules being in the rotational state of j_{NO} = 0.5. The CH_4 beam was used without carrier gas, corresponding to a rotational temperature of around 9 K and a rotational distribution spanning j_{CH4} = 0-2. REMPI was used to perform state-selective detection of the post-collision NO rotational state (j'_{NO}), and possible final CH_4 rotational energy levels (j'_{CH4}) were inferred from the conservation of energy. Density to flux correction was performed to correct the VMI images before analysis using the Finite slice analysis (FINA) method.[232]

The radial integrations of the resultant VMI images showed that low j'_{NO} levels were populated predominantly by forward scattered collisions, with a broad maximum in the differential cross section that moved to sideways and ultimately backwards scattering as j'_{NO} increased. This change in scattering angle was interpreted based on "rotational rainbow" theory. For the largest j'_{NO} values, the backward-scattering angles were well described by the 2-D hard ellipse model of rotational rainbow scattering, which is calculated based on the collision between a hard sphere and a hard ellipse.[25, 241] This interaction, including the strong repulsive potentials that occur at short distances, fits well with the large amount of rotational excitation of the NO observed under these conditions. The forward-scattering observed for low j'_{NO} fitted the angles predicted by "L-type" rotational rainbow theory, which occurs when the attractive potential between the two species becomes significant.[26] The limited amount of interaction between the two species at these impact parameters fits well with the modest rotational excitation of the NO observed. The intermediate values of j'_{NO} showed rainbow angles between those predicted by the two models, suggesting mixed character between the L-type and hard ellipse type models.

The values of j'_{CH4} are anticorrelated to j'_{NO}. This anticorrelation was suggested to be a consequence of the varying torque on the CH_4 molecule: higher impact parameters resulted in the NO molecule imparting a higher torque on the CH_4 molecule, and hence increasing the rotational excitation, and *vice versa* with smaller impact parameters. The values of j'_{CH4} were consistently below the maximum possible based on the total energy of the system, which reduced the likelihood that the anticorrelation was just due to energy limitations.

This work could readily be developed through computational studies to support the interpretations presented here, and through higher resolution experimental work.

Computational studies could be performed by QCT methods but first require a global PES for the NO-CH_4 system to be calculated and fitted. An initial step towards this could be made by adapting an established NO-rare gas potential based on the mass, diameter and polarizability of CH_4, using trajectory software such as HIBRIDON.[8, 281] Higher resolution experimental studies may be able to identify the individual rings associated with j'_{CH4} states in the VMI images, which were blurred together by experimental factors in the present work.

The last investigation presented in this thesis consists of attempts to study the reactive scattering of cyanogen radicals with methane. These attempts established the ability of the Bristol apparatus to reliably produce cyanogen radicals from the photolysis of Cyanogen Iodide at 193 nm. Prior to suspension of experimental studies for this thesis, no 2-colour (pump photolysis, REMPI probe) detection of Methyl Iodide was observed, nor was any evidence of reactive scattering observed. Future researchers utilising the apparatus may benefit from finding 2-colour signal from MeI photodissociation to assist characterisation of the photolysis nozzle conditions at the methyl detection wavelength, before continuing on to attempt reactive scattering with methane.

References

1. Chen, C. H.; Siska, P. E.; Lee, Y. T., Intermolecular potentials from crossed beam differential elastic scattering measurements VIII. He+Ne, He+Ar, He+Kr, and He+Xe. *J. Chem. Phys.* **1973,** *59* (2), 601.
2. Gao, R. S.; Johnson, L. K.; Nitz, D. E.; Smith, K. A.; Stebbings, R. F., Absolute differential cross sections for small-angle elastic scattering in helium--rare-gas collisions at keV energies. *Phys. Rev. A* **1987,** *36* (7), 3077.
3. Landorf, R. W.; Mueller, C. R., Total collision cross sections of argon with light gases by crossed molecular beams. *Phys. Lett.* **1966,** *19* (8), 658.
4. Rothe, E. W.; Marino, L. L.; Neynaber, R. H.; Rol, P. K.; Trujillo, S. M., Scattering of Thermal Rare Gas Beams by Argon. Influence of the Long-Range Dispersion Forces. *Phys. Rev.* **1962,** *126* (2), 598.
5. Bontuyan, L. S.; Suits, A. G.; Houston, P. L.; Whitaker, B. J., State-Resolved Differential Cross Sections for Crossed-Beam Argon-Nitric Oxide Inelastic Scattering by Direct Ion Imaging. *J. Phys. Chem.* **1993,** *97*, 6342.
6. Eyles, C. J.; Brouard, M.; Yang, C. H.; Kłos, J.; Aoiz, F. J.; Gijsbertsen, A.; Wiskerke, A. E.; Stolte, S., Interference structures in the differential cross-sections for inelastic scattering of NO by Ar. *Nat. Chem.* **2011,** *3*, 597.
7. Lin, A.; Antonova, S.; Tsakotellis, A. P.; McBane, G. C., Λ Doublet Propensities in Ar−NO Rotationally Inelastic Scattering at 220 meV. *J. Phys. Chem. A* **1999,** *103* (9), 1198.
8. Brouard, M.; Chadwick, H.; Eyles, C. J.; Hornung, B.; Nichols, B.; Aoiz, F. J.; Jambrina, P. G.; Stolte, S., Rotational Alignment Effects in NO(X) + Ar Inelastic Collisions: an Experimental Study. *J. Chem. Phys.* **2013,** *138*, 104310.
9. Aoiz, F. J.; Verdasco, J. E.; Herrero, V. J.; Saez Rabanos, V.; Alexander, M. A., Attractive and Repulsive Interactions in the Inelastic Scattering of NO by Ar: a Comparison between Classical Trajectory and Close-Coupling Quantum Mechanical Results. *J. Chem. Phys.* **2003,** *119*, 5860.
10. Wang, X.-D.; Robertson, P. A.; Cascarini, F. J. J.; Quinn, M. S.; McManus, J. W.; Orr-Ewing, A. J., Observation of Rainbows in the Rotationally Inelastic Scattering of NO with CH_4. *J. Phys. Chem. A* **2019,** *123* (36), 7758.
11. Palma, J.; Manthe, U., Non-adiabatic effects in F + CHD_3 reactive scattering. *J. Chem. Phys.* **2017,** *146* (21), 214117.
12. Czako, G.; Bowman, J. M., Quasiclassical trajectory calculations of correlated product distributions for the F + CHD_3(v_1 = 0, 1) reactions using an ab initio potential energy surface. *J. Chem. Phys.* **2009,** *131* (24), 244302.
13. Greaves, S. J.; Rose, R. A.; Abou-Chahine, F.; Glowacki, D. R.; Troya, D.; Orr-Ewing, A. J., Quasi-classical trajectory study of the dynamics of the Cl + CH_4 → HCl + CH_3 reaction. *Phys. Chem. Chem. Phys.* **2011,** *13* (23), 11438.
14. Yan, S.; Wu, Y.-T.; Zhang, B.; Yue, X.-F.; Liu, K., Do Vibrational Excitations of CHD_3 Preferentially Promote Reactivity Toward the Chlorine Atom? *Science* **2007,** *316* (5832), 1723.
15. Polanyi, J. C., Concepts in reaction dynamics. *Acc. Chem. Res.* **1972,** *5* (5), 161.
16. Polanyi, J. C., Some Concepts in Reaction Dynamics. *Science* **1987,** *236* (4802), 680.
17. Scoles, G., *Atomic and molecular beam methods*. Oxford University Press: New York, 1988.
18. Brouard, M.; Vallance, C., *Tutorials in Molecular Reaction Dynamics*. 2010.
19. Naulin, C.; Costes, M., Crossed-beam study of the Al($^2P_{1/2,3/2}$)+O_2($X^3\Sigma^-_g$)→AlO($X^2\Sigma^+$)+O(^3P_J) reaction at low and very low kinetic energies. *Chem. Phys. Lett.* **1999,** *310* (3), 231.
20. Willis, P. A.; Stauffer, H. U.; Hinrichs, R. Z.; Davis, H. F., Rotatable source crossed molecular beams apparatus with pulsed ultraviolet/vacuum ultraviolet photoionization detection. *Rev. Sci. Instrum.* **1999,** *70* (6), 2606.

21. Wei, Q.; Lyuksyutov, I.; Herschbach, D., Merged-beams for slow molecular collision experiments. *J. Chem. Phys.* **2012,** *137* (5), 054202.
22. Macdonald, R. G.; Liu, K., State-to-state integral cross sections for the inelastic scattering of CH(X $^2\Pi$)+He: Rotational rainbow and orbital alignment. *J. Chem. Phys.* **1989,** *91* (2), 821.
23. Levine, R. D., *Molecular Reaction Dynamics*. Cambridge University Press: 2009.
24. Eyles, C. J.; Brouard, M.; Chadwick, H.; Aoiz, F. J.; Klos, J.; Gijsbertsen, A.; Zhang, X.; Stolte, S., The Effect of Parity Conservation on the Spin-Orbit Conserving and Spin-Orbit Changing Differential Cross Sections for the Inelastic Scattering of NO(X) by Ar. *Phys. Chem. Chem. Phys.* **2012,** *14*, 5420.
25. Bosanac, S.; Buck, U., Rotational Rainbow Scattering from an Off-Center Rigid Shell-Model. *Chem. Phys. Lett.* **1981,** *81*, 315.
26. Onvlee, J.; Vogels, S. N.; van der Avoird, A. D.; Groenenboom, G. C.; van de Meerakker, S. Y. T., Resolving Rainbows with Superimposed Diffraction Oscillations in NO plus Rare Gas Scattering: Experiment and Theory. *New J. Phys.* **2015,** *17*, 055019.
27. Jensen, F., *Introduction to Computational Chemistry*. John Wiley & Sons, Incorporated: New York, 2007.
28. Echenique, P.; Alonso, J. L., A mathematical and computational review of Hartree–Fock SCF methods in quantum chemistry. *Mol. Phys.* **2007,** *105* (23-24), 3057.
29. Frisch, M. J.; Head-Gordon, M.; Pople, J. A., A direct MP2 gradient method. *Chem. Phys. Lett.* **1990,** *166* (3), 275.
30. Møller, C.; Plesset, M. S., Note on an Approximation Treatment for Many-Electron Systems. *Phys. Rev.* **1934,** *46* (7), 618.
31. Pople, J. A.; Krishnan, R.; Schlegel, H. B.; Binkley, J. S., Electron correlation theories and their application to the study of simple reaction potential surfaces. *Int. J. Quantum Chem* **1978,** *14* (5), 545.
32. Siegbahn, P. E. M.; Almlöf, J.; Heiberg, A.; Roos, B. O., The complete active space SCF (CASSCF) method in a Newton–Raphson formulation with application to the HNO molecule. *J. Chem. Phys.* **1981,** *74* (4), 2384.
33. Kohn, W.; Sham, L. J., Self-Consistent Equations Including Exchange and Correlation Effects. *Phys. Rev.* **1965,** *140* (4A), A1133.
34. Hohenberg, P.; Kohn, W., Inhomogeneous Electron Gas. *Phys. Rev.* **1964,** *136* (3B), B864.
35. Becke, A. D., Density-functional thermochemistry. III. The role of exact exchange. *J. Chem. Phys.* **1993,** *98* (7), 5648.
36. Adamo, C.; Jacquemin, D., The calculations of excited-state properties with Time-Dependent Density Functional Theory. *Chem. Soc. Rev.* **2013,** *42* (3), 845.
37. Laurent, A. D.; Jacquemin, D., TD-DFT benchmarks: A review. *Int. J. Quantum Chem* **2013,** *113* (17), 2019.
38. Slater, J. C., Atomic Shielding Constants. *Phys. Rev.* **1930,** *36* (1), 57.
39. Hehre, W. J.; Stewart, R. F.; Pople, J. A., Self-Consistent Molecular-Orbital Methods. I. Use of Gaussian Expansions of Slater-Type Atomic Orbitals. *J. Chem. Phys.* **1969,** *51* (6), 2657.
40. Marx, D.; Hutter, J., *Ab Initio Molecular Dynamics: Basic Theory and Advanced Methods*. Cambridge University Press: 2009.
41. Braams, B. J.; Bowman, J. M., Permutationally invariant potential energy surfaces in high dimensionality. *Int. Rev. Phys. Chem.* **2009,** *28* (4), 577.
42. Bowman, J. M.; Czakó, G.; Fu, B., High-dimensional ab initio potential energy surfaces for reaction dynamics calculations. *Phys. Chem. Chem. Phys.* **2011,** *13* (18), 8094.
43. Raff, L. M., Theoretical investigations of the reaction dynamics of polyatomic systems: Chemistry of the hot atom (T* + CH_4) and (T* + CD_4) systems. *J. Chem. Phys.* **1974,** *60* (6), 2220.
44. Schatz, G. C., The analytical representation of electronic potential-energy surfaces. *Rev. Mod. Phys.* **1989,** *61* (3), 669.

45. Collins, M. A., Molecular potential-energy surfaces for chemical reaction dynamics. *Theor. Chem. Acc.* **2002,** *108* (6), 313.
46. Hollebeek, T.; Ho, T.-S.; Rabitz, H., Constructing Multidimensional Molecular Potential Energy Surfaces From *Ab Initio* Data *Annu. Rev. Phys. Chem.* **1999,** *50* (1), 537.
47. Dawes, R.; Passalacqua, A.; Wagner, A. F.; Sewell, T. D.; Minkoff, M.; Thompson, D. L., Interpolating moving least-squares methods for fitting potential energy surfaces: Using classical trajectories to explore configuration space. *J. Chem. Phys.* **2009,** *130* (14), 144107.
48. Ischtwan, J.; Collins, M. A., Molecular potential energy surfaces by interpolation. *J. Chem. Phys.* **1994,** *100* (11), 8080.
49. Cooper, A. M.; Hallmen, P. P.; Kästner, J., Potential energy surface interpolation with neural networks for instanton rate calculations. *J. Chem. Phys.* **2018,** *148* (9), 094106.
50. Warshel, A.; Weiss, R. M., An Empirical Valence Bond Approach for Comparing Reactions in Solutions and in Enzymes. *JACS* **1980,** *102* (20), 6218.
51. Hornung, B.; Preston, T. J.; Pandit, S.; Harvey, J. N.; Orr-Ewing, A. J., Computational Study of Competition between Direct Abstraction and Addition-Elimination in the Reaction of Cl Atoms with Propene. *J. Phys. Chem. A* **2015,** *119* (36), 9452.
52. Hornung, B.; Harvey, J. N.; Preston, T. J.; Dunning, G. T.; Orr-Ewing, A. J., Empirical Valence Bond Theory Studies of the CH_4 + Cl --> CH_3 + HCl Reaction. *J. Phys. Chem. A* **2015,** *119* (37), 9590.
53. Miller, W., *Dynamics of Molecular Collisions: Part B*. Springer US: 2013.
54. Bonnet, L.; Rayez, J. C., Quasiclassical trajectory method for molecular scattering processes: necessity of a weighted binning approach. *Chem. Phys. Lett.* **1997,** *277* (1), 183.
55. Bonnet, L.; Espinosa-García, J., The method of Gaussian weighted trajectories. V. On the 1GB procedure for polyatomic processes. *J. Chem. Phys.* **2010,** *133* (16), 164108.
56. Sierra, J. D.; Bonnet, L.; González, M., Quasi-Classical Trajectory–Gaussian Binning Study of the OH + D_2 → HOD(v_1',v_2',v_3') + D Angle–Velocity and Vibrational Distributions at a Collision Energy of 0.28 eV. *J. Phys. Chem. A* **2011,** *115* (26), 7413.
57. Schatz, G. C., A quasiclassical trajectory study of reagent vibrational excitation effects in the OH+H_2→H_2O+H reaction. *J. Chem. Phys.* **1981,** *74* (2), 1133.
58. Aoiz, F. J.; Herrero, V. J.; Rábanos, V. S., Effects of translational, rotational, and vibrational energy on the dynamics of the D+H_2 exchange reaction. A classical trajectory study. *J. Chem. Phys.* **1991,** *94* (12), 7991.
59. Panda, A. N.; Althorpe, S. C., Quantum wave packet study of the H+HBr→H_2+Br reaction. *Chem. Phys. Lett.* **2007,** *439* (1), 50.
60. Medvedev, D. M.; Gray, S. K.; Goldfield, E. M.; Lakin, M. J.; Troya, D.; Schatz, G. C., Quantum wave packet and quasiclassical trajectory studies of OH+CO: Influence of the reactant channel well on thermal rate constants. *J. Chem. Phys.* **2004,** *120* (3), 1231.
61. Althorpe, S. C., Time-dependent plane wave packet formulation of quantum scattering with application to H+D_2→HD+D. *J. Chem. Phys.* **2002,** *117* (10), 4623.
62. Atkins, P. W.; Friedman, R. S., *Molecular Quantum Mechanics*. OUP Oxford: 2011.
63. Regan, P. M.; Langford, S. R.; Orr-Ewing, A. J.; Ashfold, M. N. R., The ultraviolet photodissociation dynamics of hydrogen bromide. *J. Chem. Phys.* **1999,** *110* (1), 281.
64. Nikitin, E. E.; Zare, R. N., Correlation diagrams for Hund's coupling cases in diatomic molecules with high rotational angular momentum. *Mol. Phys.* **1994,** *82* (1), 85.
65. Hollas, J. M., *Modern spectroscopy*. 3rd ed. ed.; J. Wiley: Chichester, 1996.
66. Worth, G. A.; Cederbaum, L. S., BEYOND BORN-OPPENHEIMER: Molecular Dynamics Through a Conical Intersection. *Annu. Rev. Phys. Chem.* **2004,** *55* (1), 127.
67. Yarkony, D. R., Diabolical conical intersections. *Rev. Mod. Phys.* **1996,** *68* (4), 985.
68. Matsika, S.; Krause, P., Nonadiabatic Events and Conical Intersections. *Annu. Rev. Phys. Chem.* **2011,** *62* (1), 621.
69. Lasorne, B.; Worth, G. A.; Robb, M. A., Excited-state dynamics. *WIREs Computational Molecular Science* **2011,** *1* (3), 460.

70. Casavecchia, P., Chemical reaction dynamics with molecular beams. *Rep. Prog. Phys.* **2000,** *63* (3), 355.
71. Jankunas, J.; Osterwalder, A., Cold and Controlled Molecular Beams: Production and Applications. *Annu. Rev. Phys. Chem.* **2015,** *66* (1), 241.
72. Gijsbertsen, A.; Linnartz, H.; Rus, G.; Wiskerke, A. E.; Stolte, S.; Chandler, D. W.; Kłos, J., Differential cross sections for collisions of hexapole state-selected NO with He. *J. Chem. Phys.* **2005,** *123* (22), 224305.
73. van de Meerakker, S. Y. T.; Bethlem, H. L.; Meijer, G., Taming molecular beams. *Nature Physics* **2008,** *4* (8), 595.
74. Chandler, D. W.; Houston, P. L., Two-dimensional imaging of state-selected photodissociation products detected by multiphoton ionization. *J. Chem. Phys.* **1987,** *87* (2), 1445.
75. Eppink, A. T. J. B.; Parker, D. H., Velocity map imaging of ions and electrons using electrostatic lenses: Application in photoelectron and photofragment ion imaging of molecular oxygen. *Rev. Sci. Instrum.* **1997,** *68* (9), 3477.
76. Gebhardt, C. R.; Rakitzis, T. P.; Samartzis, P. C.; Ladopoulos, V.; Kitsopoulos, T. N., Slice imaging: A new approach to ion imaging and velocity mapping. *Rev. Sci. Instrum.* **2001,** *72* (10), 3848.
77. Lin, J. J.; Zhou, J.; Shiu, W.; Liu, K., Application of time-sliced ion velocity imaging to crossed molecular beam experiments. *Rev. Sci. Instrum.* **2003,** *74* (4), 2495.
78. Ashfold, M. N.; Nahler, N. H.; Orr-Ewing, A. J.; Vieuxmaire, O. P.; Toomes, R. L.; Kitsopoulos, T. N.; Garcia, I. A.; Chestakov, D. A.; Wu, S. M.; Parker, D. H., Imaging the dynamics of gas phase reactions. *Phys. Chem. Chem. Phys.* **2006,** *8* (1), 26.
79. Townsend, D.; Minitti, M. P.; Suits, A. G., Direct current slice imaging. *Rev. Sci. Instrum.* **2003,** *74* (4), 2530.
80. Garcia, G. A.; Nahon, L.; Powis, I., Two-dimensional charged particle image inversion using a polar basis function expansion. *Rev. Sci. Instrum.* **2004,** *75* (11), 4989.
81. Roberts, G. M.; Nixon, J. L.; Lecointre, J.; Wrede, E.; Verlet, J. R., Toward real-time charged-particle image reconstruction using polar onion-peeling. *Rev. Sci. Instrum.* **2009,** *80* (5), 053104.
82. Heck, A. J. R.; Chandler, D. W., Imaging Techniques for the Study of Chemical Reaction Dynamics. *Annu. Rev. Phys. Chem.* **1995,** *46* (1), 335.
83. Nomerotski, A.; Brouard, M.; Campbell, E.; Clark, A.; Crooks, J.; Fopma, J.; John, J. J.; Johnsen, A. J.; Slater, C.; Turchetta, R.; Vallance, C.; Wilman, E.; Yuen, W. H., Pixel Imaging Mass Spectrometry with fast and intelligent Pixel detectors. *J. Instrum.* **2010,** *5* (07), C07007.
84. John, J. J.; Brouard, M.; Clark, A.; Crooks, J.; Halford, E.; Hill, L.; Lee, J. W. L.; Nomerotski, A.; Pisarczyk, R.; Sedgwick, I.; Slater, C. S.; Turchetta, R.; Vallance, C.; Wilman, E.; Winter, B.; Yuen, W. H., PImMS, a fast event-triggered monolithic pixel detector with storage of multiple timestamps. *J. Instrum.* **2012,** *7* (08), C08001.
85. Slater, C. S.; Blake, S.; Brouard, M.; Lauer, A.; Vallance, C.; Bohun, C. S.; Christensen, L.; Nielsen, J. H.; Johansson, M. P.; Stapelfeldt, H., Coulomb-explosion imaging using a pixel-imaging mass-spectrometry camera. *Phys. Rev. A* **2015,** *91* (5), 053424.
86. Amini, K.; Blake, S.; Brouard, M.; Burt, M. B.; Halford, E.; Lauer, A.; Slater, C. S.; Lee, J. W.; Vallance, C., Three-dimensional imaging of carbonyl sulfide and ethyl iodide photodissociation using the pixel imaging mass spectrometry camera. *Rev. Sci. Instrum.* **2015,** *86* (10), 103113.
87. Ingle, R. A.; Hansen, C. S.; Elsdon, E.; Bain, M.; King, S. J.; Lee, J. W. L.; Brouard, M.; Vallance, C.; Turchetta, R.; Ashfold, M. N. R., Ultraviolet photochemistry of 2-bromothiophene explored using universal ionization detection and multi-mass velocity-map imaging with a PImMS2 sensor. *J. Chem. Phys.* **2017,** *147* (1), 013914.
88. Slater, C. S.; Blake, S.; Brouard, M.; Lauer, A.; Vallance, C.; John, J. J.; Turchetta, R.; Nomerotski, A.; Christensen, L.; Nielsen, J. H.; Johansson, M. P.; Stapelfeldt, H., Covariance imaging experiments using a pixel-imaging mass-spectrometry camera. *Phys. Rev. A* **2014,** *89* (1), 011401.
89. Ashfold, M.; Howe, J., Multiphoton spectroscopy of molecular species. *Annu. Rev. Phys. Chem.* **1994,** *45* (1), 57.

90. Tkac, O.; Saha, A. K.; Onvlee, J.; Yang, C. H.; Sarma, G.; Bishwakarma, C. K.; van de Meerakker, S. Y.; van der Avoird, A.; Parker, D. H.; Orr-Ewing, A. J., State-to-state resolved differential cross sections for rotationally inelastic scattering of ND_3 with He. *Phys. Chem. Chem. Phys.* **2014,** *16* (2), 477.
91. Zare, R. N.; Herschbach, D. R., Doppler line shape of atomic fluorescence excited by molecular photodissociation. *Proc. IEEE.* **1963,** *51*, 173.
92. Jonah, C., Effect of Rotation and Thermal Velocity on the Anisotropy in Photodissociation Spectroscopy. *J. Chem. Phys.* **1971,** *55* (4), 1915.
93. Tripathi, G. N. R.; Pandey, V. M., Near Ultraviolet Absorption Spectre of 3,4-Dichloro- and 2,4-Dibromofluorobenzene Molecules in Vapour State. *J. Chim. Phys.* **1976,** *72*.
94. Tripathi, G. N. R.; Pandey, V. M., Vibrational Assignments of IR-Spectra of 3,4-Dichlorofluorobenzene and 2,4-Dibromofluorobenzene and 2,5-Dichlorobromobenzene and 3,4-Dichlorobromobenzene Molecules. *Indian Journal of Pure and Applied Physics* **1977,** *15* (6), 432.
95. Pandit, S. Velocity Map Imaging Studies of Competing Dynamics in the Gas Phase. University of Bristol, 2017.
96. Herschbach, D. R.; Kwei, G. H.; Norris, J. A., Reactive Scattering in Crossed Molecular Beams. K Atoms with CH_3I and C_2H_5I. *J. Chem. Phys.* **1961,** *34* (5), 1842.
97. Lee, Y. T.; McDonald, J. D.; LeBreton, P. R.; Herschbach, D. R., Molecular Beam Reactive Scattering Apparatus with Electron Bombardment Detector. *Rev. Sci. Instrum.* **1969,** *40* (11), 1402.
98. NobelPrize.org, The dynamics of chemical reactions – a fascinating new field of research. Nobel Media AB 2020: https://www.nobelprize.org/prizes/chemistry/1986/press-release/, 1986.
99. Ansón, A.; Kuznicki, S. M.; Kuznicki, T.; Dunn, B. C.; Eyring, E. M.; Hunter, D. B., Separation of Argon and Oxygen by Adsorption on a Titanosilicate Molecular Sieve. *Sep. Sci. Technol.* **2009,** *44* (7), 1604.
100. Tkáč, O. Inelastic Scattering of Symmetric Top Molecules. University of Bristol, 2013.
101. Geusic, J. E.; Marcos, H. M.; Van Uitert, L. G., Laser Oscillations In Nd-Doped Yttrium Aluminum, Yttrium Gallium And Gadolinium Garnets. *Appl. Phys. Lett.* **1964,** *4* (10), 182.
102. Duarte, F. J., 5 - Dye Lasers. In *Tunable Lasers Handbook*, Duarte, F. J., Ed. Academic Press: San Diego, 1995; pp 167.
103. Sze, R. C.; Harris, D. G., 3 - Tunable Excimer Lasers. In *Tunable Lasers Handbook*, Duarte, F. J., Ed. Academic Press: San Diego, 1995; pp 33.
104. Arepalli, S.; Presser, N.; Robie, D.; Gordon, R. J., The detection of bromine atoms by resonant multiphoton ionization. *Chem. Phys. Lett.* **1985,** *117* (1), 64.
105. Sansonetti, J. E.; Martin, W. C., Handbook of Basic Atomic Spectroscopic Data. *J. Phys. Chem. Ref. Data* **2005,** *34* (4), 1559.
106. Black, J. F.; Powis, I., Rotational structure and predissociation dynamics of the methyl $4p_z(v=0)$ Rydberg state investigated by resonance enhanced multiphoton ionization spectroscopy. *J. Chem. Phys.* **1988,** *89* (7), 3986.
107. Brouard, M.; Gordon, S. D. S.; Nichols, B.; Squires, E.; Walpole, V.; Aoiz, F. J.; Stolte, S., Angular Distributions for the Inelastic Scattering of $NO(X^2\Pi)$ with $O_2(X^3\Sigma_g^-)$. *J. Chem. Phys.* **2017,** *146*, 204304.
108. Parker, D. H.; Eppink, A. T. J. B., Photoelectron and photofragment velocity map imaging of state-selected molecular oxygen dissociation/ionization dynamics. *J. Chem. Phys.* **1997,** *107* (7), 2357.
109. *Origin*, OriginLab Corporation: Northampton, MA, USA.
110. Hase, W. L.; Duchovic, R. J.; Hu, X.; Komornicki, A.; Lim, K. F.; Lu, D.-h.; Peslherbe, G. H.; Swamy, K.; Vande Linde, S. R.; Varandas, A.; Wang, H.; Wolf, R. J. *VENUS96*, 1996.
111. Hirschfelder, J.; Eyring, H.; Topley, B., Reactions Involving Hydrogen Molecules and Atoms. *J. Chem. Phys.* **1936,** *4* (3), 170.
112. Wall, F. T.; Hiller, L. A.; Mazur, J., Statistical Computation of Reaction Probabilities. *J. Chem. Phys.* **1958,** *29* (2), 255.

113. Karplus, M.; Porter, R. N.; Sharma, R. D., Exchange Reactions with Activation Energy. I. Simple Barrier Potential for (H, H_2). *J. Chem. Phys.* **1965,** *43* (9), 3259.
114. Varandas, A. J. C., Excitation function for H+O_2 reaction: A study of zero-point energy effects and rotational distributions in trajectory calculations. *J. Chem. Phys.* **1993,** *99* (2), 1076.
115. Krishnan, R.; Binkley, J. S.; Seeger, R.; Pople, J. A., Self-consistent molecular orbital methods. XX. A basis set for correlated wave functions. *J. Chem. Phys.* **1980,** *72* (1), 650.
116. Knowles, P. J.; Andrews, J. S.; Amos, R. D.; Handy, N. C.; Pople, J. A., Restricted Møller—Plesset theory for open-shell molecules. *Chem. Phys. Lett.* **1991,** *186* (2), 130.
117. Knizia, G.; Adler, T. B.; Werner, H.-J., Simplified CCSD(T)-F12 methods: Theory and benchmarks. *J. Chem. Phys.* **2009,** *130* (5), 054104.
118. Peterson, K. A.; Adler, T. B.; Werner, H.-J., Systematically convergent basis sets for explicitly correlated wavefunctions: The atoms H, He, B–Ne, and Al–Ar. *J. Chem. Phys.* **2008,** *128* (8), 084102.
119. Werner, H.-J.; Knowles, P. J.; Knizia, G.; Manby, F. R.; Schütz, M., Molpro: a general-purpose quantum chemistry program package. *WIREs Computational Molecular Science* **2012,** *2* (2), 242.
120. Vetterling, W. T.; Press, W. H., *Numerical Recipes in FORTRAN: The Art of Scientific Computing*. Cambridge University Press: 1992.
121. Bunker, D. L., Classical Trajectory Methods, *Methods in Computational Physics: Advances in Research and Applications*, Alder, B.; Fernbach, S.; Rotenberg, M., Eds. Elsevier: 1971; Vol. 10, 287.
122. Suits, A. G., Roaming Reactions and Dynamics in the van der Waals Region. *Annu. Rev. Phys. Chem.* **2020,** *71* (1), 77.
123. Walavalkar, M.; Sharma, A.; Alwe, H. D.; Pushpa, K. K.; Dhanya, S.; Naik, P. D.; Bajaj, P. N., Cl atom initiated oxidation of 1-alkenes under atmospheric conditions. *Atmos. Environ.* **2013,** *67*, 93.
124. Singh, H. B.; Gregory, G. L.; Anderson, B.; Browell, E.; Sachse, G. W.; Davis, D. D.; Crawford, J.; Bradshaw, J. D.; Talbot, R.; Blake, D. R.; Thornton, D.; Newell, R.; Merrill, J., Low ozone in the marine boundary layer of the tropical Pacific Ocean: Photochemical loss, chlorine atoms, and entrainment. *J. Geophys. Res. Atmos.* **1996,** *101* (D1), 1907.
125. Spicer, C. W.; Chapman, E. G.; Finlayson-Pitts, B. J.; Plastridge, R. A.; Hubbe, J. M.; Fast, J. D.; Berkowitz, C. M., Unexpectedly high concentrations of molecular chlorine in coastal air. *Nature* **1998,** *394* (6691), 353.
126. Tanaka, P. L.; Oldfield, S.; Neece, J. D.; Mullins, C. B.; Allen, D. T., Anthropogenic Sources of Chlorine and Ozone Formation in Urban Atmospheres. *Environ. Sci. Technol.* **2000,** *34* (21), 4470.
127. Thornton, J. A.; Kercher, J. P.; Riedel, T. P.; Wagner, N. L.; Cozic, J.; Holloway, J. S.; Dube, W. P.; Wolfe, G. M.; Quinn, P. K.; Middlebrook, A. M.; Alexander, B.; Brown, S. S., A large atomic chlorine source inferred from mid-continental reactive nitrogen chemistry. *Nature* **2010,** *464* (7286), 271.
128. Arneth, A.; Schurgers, G.; Lathiere, J.; Duhl, T.; Beerling, D. J.; Hewitt, C. N.; Martin, M.; Guenther, A., Global terrestrial isoprene emission models: sensitivity to variability in climate and vegetation. *Atmos. Chem. Phys.* **2011,** *11* (15), 8037.
129. Murray, C.; Orr-Ewing, A. J., The dynamics of chlorine-atom reactions with polyatomic organic molecules. *Int. Rev. Phys. Chem.* **2004,** *23* (3), 43.
130. Pilgrim, J. S.; McIlroy, A.; Taatjes, C. A., Kinetics of Cl Atom Reactions with Methane, Ethane, and Propane from 292 to 800 K. *J. Phys. Chem. A* **1997,** *101* (10), 1873.
131. Bottoni, A.; Poggi, G., An ab initio study of hydrogen abstraction by fluorine, chlorine and bromine atoms from ethane and propane. *J. Mol. Struc. Theochem* **1995,** *337* (2), 161.
132. Estillore, A. D.; Visger-Kiefer, L. M.; Ghani, T. A.; Suits, A. G., Dynamics of H and D abstraction in the reaction of Cl atom with butane-1,1,1,4,4,4-d_6. *Phys. Chem. Chem. Phys.* **2011,** *13* (18), 8433.
133. Pandit, S.; Hornung, B.; Dunning, G. T.; Preston, T. J.; Brazener, K.; Orr-Ewing, A. J., Primary vs. secondary H-atom abstraction in the Cl-atom reaction with n-pentane. *Phys. Chem. Chem. Phys.* **2017,** *19* (2), 1614.

134. Pilgrim, J. S.; Taatjes, C. A., Infrared Absorption Probing of the Cl + C_3H_6 Reaction: Rate Coefficients for HCl Production between 290 and 800 K. *J. Phys. Chem. A* **1997,** *101* (32), 5776-5782.
135. Coquet, S.; Ariya, P. A., Kinetics of the gas-phase reactions of Cl atom with selected C2-C5 unsaturated hydrocarbons at 283 <T < 323 K. *Int. J. Chem. Kinet.* **2000,** *32* (8), 478.
136. Kaiser, E. W.; Wallington, T. J., Temperature (290–400K) and pressure (5–900Torr) dependence of the kinetics of the reactions of chlorine atoms with propene and 1-butene. *Chem. Phys. Lett.* **2011,** *501* (4-6), 187.
137. Preston, T. J.; Dunning, G. T.; Orr-Ewing, A. J.; Vazquez, S. A., Direct and indirect hydrogen abstraction in Cl + alkene reactions. *J. Phys. Chem. A* **2014,** *118* (30), 5595.
138. Lee, F. S. C.; Rowland, F. S., Thermal Chlorine-38 Reactions with Propene. *J. Phys. Chem.* **1977,** *81* (13), 1222.
139. Kaiser, E. W.; Wallington, T. J., Pressure Dependence of the Reaction Cl + C_3H_6. *J. Phys. Chem.* **1996,** *100* (23), 9788.
140. Bowman, J. M., Skirting the transition state, a new paradigm in reaction rate theory. *Proc. Natl. Acad. Sci. USA* **2006,** *103* (44), 16061.
141. Suits, A. G., Roaming atoms and radicals: a new mechanism in molecular dissociation. *Acc. Chem. Res.* **2008,** *41* (7), 873.
142. Quinn, M. S.; Andrews, D. U.; Nauta, K.; Jordan, M. J. T.; Kable, S. H., The energy dependence of CO(v,J) produced from H_2CO via the transition state, roaming, and triple fragmentation channels. *J. Chem. Phys.* **2017,** *147* (1), 013935.
143. Heazlewood, B. R.; Jordan, M. J.; Kable, S. H.; Selby, T. M.; Osborn, D. L.; Shepler, B. C.; Braams, B. J.; Bowman, J. M., Roaming is the dominant mechanism for molecular products in acetaldehyde photodissociation. *Proc. Natl. Acad. Sci. USA* **2008,** *105* (35), 12719.
144. Sivaramakrishnan, R.; Michael, J. V.; Klippenstein, S. J., Direct observation of roaming radicals in the thermal decomposition of acetaldehyde. *J. Phys. Chem. A* **2010,** *114* (2), 755.
145. Shepler, B. C.; Braams, B. J.; Bowman, J. M., Quasiclassical trajectory calculations of acetaldehyde dissociation on a global potential energy surface indicate significant non-transition state dynamics. *J. Phys. Chem. A* **2007,** *111* (34), 8282.
146. Rubio-Lago, L.; Amaral, G. A.; Arregui, A.; Izquierdo, J. G.; Wang, F.; Zaouris, D.; Kitsopoulos, T. N.; Banares, L., Slice imaging of the photodissociation of acetaldehyde at 248 nm. Evidence of a roaming mechanism. *Phys. Chem. Chem. Phys.* **2007,** *9* (46), 6123.
147. Joalland, B.; Shi, Y.; Kamasah, A.; Suits, A. G.; Mebel, A. M., Roaming dynamics in radical addition-elimination reactions. *Nat Commun* **2014,** *5*, 4064.
148. Efron, B.; Tibshirani, R. J., *An Introduction to the Bootstrap*. CRC Press: 1994.
149. Houston, P. L.; Conte, R.; Bowman, J. M., Roaming Under the Microscope: Trajectory Study of Formaldehyde Dissociation. *J. Phys. Chem. A* **2016,** *120* (27), 5103.
150. Cofer-Shabica, D. V.; Stratt, R. M., What is special about how roaming chemical reactions traverse their potential surfaces? Differences in geodesic paths between roaming and non-roaming events. *J. Chem. Phys.* **2017,** *146* (21), 214303.
151. Abou-Chahine, F.; Greaves, S. J.; Dunning, G. T.; Orr-Ewing, A. J.; Greetham, G. M.; Clark, I. P.; Towrie, M., Vibrationally resolved dynamics of the reaction of Cl atoms with 2,3-dimethylbut-2-ene in chlorinated solvents. *Chem Sci* **2013,** *4* (1), 226.
152. Estillore, A. D.; Visger, L. M.; Suits, A. G., Crossed-beam dc slice imaging of chlorine atom reactions with pentane isomers. *J. Chem. Phys.* **2010,** *132* (16), 164313.
153. Huang, C.; Li, W.; Suits, A. G., Rotationally resolved reactive scattering: imaging detailed Cl+C_2H_6 reaction dynamics. *J. Chem. Phys.* **2006,** *125* (13), 133107.
154. Bondi, A., van der Waals Volumes and Radii. *The Journal of Physical Chemistry* **1964,** *68* (3), 441.
155. Lahankar, S. A.; Chambreau, S. D.; Townsend, D.; Suits, F.; Farnum, J.; Zhang, X.; Bowman, J. M.; Suits, A. G., The roaming atom pathway in formaldehyde decomposition. *J. Chem. Phys.* **2006,** *125* (4), 44303.

156. See the "Photochemistry of Alkyl Halides" series by Paul Kropp
157. Han, K.-L.; He, G.-Z., Photochemistry of aryl halides: Photodissociation dynamics. *Journal of Photochemistry and Photobiology C: Photochemistry Reviews* **2007,** *8* (2), 55.
158. Sage, A. G.; Oliver, T. A. A.; Murdock, D.; Crow, M. B.; Ritchie, G. A. D.; Harvey, J. N.; Ashfold, M. N. R., nσ* and πσ* excited states in aryl halide photochemistry: a comprehensive study of the UV photodissociation dynamics of iodobenzene. *Phys. Chem. Chem. Phys.* **2011,** *13* (18), 8075.
159. Ashfold, M. N. R.; King, G. A.; Murdock, D.; Nix, M. G. D.; Oliver, T. A. A.; Sage, A. G., πσ* excited states in molecular photochemistry. *Phys. Chem. Chem. Phys.* **2010,** *12* (6), 1218.
160. Lee, S.-H.; Jung, Y.-J.; Jung, K.-H., Photodissociation dynamics of CH_2BrCl at 234 nm. *Chem. Phys.* **2000,** *260* (1), 143.
161. Butler, J. H.; Battle, M.; Bender, M. L.; Montzka, S. A.; Clarke, A. D.; Saltzman, E. S.; Sucher, C. M.; Severinghaus, J. P.; Elkins, J. W., A record of atmospheric halocarbons during the twentieth century from polar firn air. *Nature* **1999,** *399* (6738), 749.
162. Atlas, E.; Sullivan, K.; Giam, C. S., Widespread occurrence of polyhalogenated aromatic ethers in the marine atmosphere. *Atmospheric Environment (1967)* **1986,** *20* (6), 1217.
163. Sun, J.-L.; Zeng, H.; Ni, H.-G., Halogenated polycyclic aromatic hydrocarbons in the environment. *Chemosphere* **2013,** *90* (6), 1751.
164. Jung, Y.-J.; Park, M. S.; Kim, Y. S.; Jung, K.-H.; Volpp, H.-R., Photodissociation of $CBrCl_3$ at 234 and 265 nm: Evidence of the curve crossing. *The Journal of Chemical Physics* **1999,** *111* (9), 4005.
165. Pence, W. H.; Baughcum, S. L.; Leone, S. R., Laser UV photofragmentation of halogenated molecules. Selective bond dissociation and wavelength-specific quantum yields for excited iodine ($^2P_{1/2}$) and bromine ($^2P_{1/2}$) atoms. *J. Phys. Chem.* **1981,** *85*, 3844.
166. Freedman, A.; Yang, S. C.; Kawasaki, M.; Bersohn, R., Photodissociation of aryl and aryl-alkyl halides at 193 nm: fragment translational energy distributions *J. Chem. Phys.* **1980,** *72*, 1028.
167. Borg, O. A.; Liu, Y.-J.; Persson, P.; Lunell, S.; Karlsson, D.; Kadi, M.; Davidsson, J., Photochemistry of Bromofluorobenzenes. *The Journal of Physical Chemistry A* **2006,** *110* (22), 7045.
168. Karlsson, D.; Anders Borg, O.; Lunell, S.; Davidsson, J.; Karlsson, H. O., Experimental and theoretical study of the photodissociation of bromo-3-fluorobenzene. *The Journal of Chemical Physics* **2008,** *128* (3), 034307.
169. Anders Borg, O., A singlet mechanism for photodissociation of bromofluorobenzenes. *Chem. Phys. Lett.* **2007,** *436* (1), 57.
170. Zhang, X.-P.; Wei, Z.-R.; Tang, Y.; Chao, T.-J.; Zhang, B.; Lin, K.-C., Halogen Effect on the Photodissociation Mechanism for Gas-Phase Bromobenzene and Iodobenzene. *ChemPhysChem* **2008,** *9* (8), 1130.
171. Kavita, K.; Das, P. K., Photodissociation of C_6H_5I, C_6F_5I, and related iodides in the ultraviolet. *The Journal of Chemical Physics* **2002,** *117* (5), 2038.
172. Numata, Y.; Watahiki, M.; Toriyama, H.; Suzuka, I., Photophysics of chlorofluorobenzenes: enhancement of sensitized phosphorescence due to cluster formation. *J. Photochem. Photobiol. A: Chem.* **1994,** *80* (1), 39.
173. Zhu, R. S.; Zhang, H.; Wang, G. J.; Gu, X. B.; Han, K. L.; He, G. Z.; Lou, N. Q., Photodissociation of o-dichlorobenzene at 266 nm *Chem. Phys.* **1999,** *248*, 285.
174. Kadi, M.; Davidsson, J., The photodissociation dynamics of dibromobenzenes and tribromobenzene in the gas phase studied with femtosecond pump-probe spectroscopy *Chem. Phys. Lett.* **2003,** *378*, 172.
175. Cheng, P. Y.; Zhong, D.; Zewail, A. H., Kinetic-energy, femtosecond resolved reaction dynamics. Modes of dissociation (in iodobenzene) from time-velocity correlations. *Chem. Phys. Lett.* **1995,** *237* (5), 399.
176. Kadi, M.; Davidsson, J., The photodissociation dynamics of dibromobenzenes and tribromobenzene in the gas phase studied with femtosecond pump–probe spectroscopy. *Chem. Phys. Lett.* **2003,** *378* (1), 172.

177. Gu, X. B.; Wang, G. J.; Huang, J. H.; Han, K. L.; He, G. Z.; Lou, N. Q., Photofragment Translational Spectroscopy of 1-Bromo-3-fluorobenzene and 1-Bromo-4-fluorobenzene at 266 nm. *J. Phys. Chem. A* **2001,** *105*, 354.
178. Tang, Y.; Lee, W.-B.; Zhang, B.; Lin, K.-C., Photodissociation Dynamics of Bromofluorobenzenes Using Velocity Imaging Technique. *The Journal of Physical Chemistry A* **2008,** *112* (7), 1421.
179. Ichimura, T.; Mori, Y.; Shinohara, H.; Nishi, N., Photodissociation channels for pentafluorochlorobenzene excited at 193 nm in molecular beams. *Chemical Physics Letters* **1986,** *125* (3), 263.
180. Ajitha, D.; Fedorov, D. G.; Finley, J. P.; Hirao, K., Photodissociation of alkyl and aryl iodides and effect of fluorination: Analysis of proposed mechanisms and vertical excitations by spin–orbit ab initio study. *The Journal of Chemical Physics* **2002,** *117* (15), 7068.
181. Foresman, J. B.; Head-Gordon, M.; Pople, J. A.; Frisch, M. J., Toward a systematic molecular orbital theory for excited states. *The Journal of Physical Chemistry* **1992,** *96* (1), 135.
182. Ditchfield, R.; Hehre, W. J.; Pople, J. A., Self-Consistent Molecular-Orbital Methods. IX. An Extended Gaussian-Type Basis for Molecular-Orbital Studies of Organic Molecules. *The Journal of Chemical Physics* **1971,** *54* (2), 724.
183. Li, W.-Z.; Chen, S.-F.; Liu, Y.-J., Relativistic multireference calculation of photodissociation of o-, m-, and p-bromofluorobenzene. *The Journal of Chemical Physics* **2011,** *134* (11), 114303.
184. Andersson, K.; Malmqvist, P. A.; Roos, B. O.; Sadlej, A. J.; Wolinski, K., Second-order perturbation theory with a CASSCF reference function. *The Journal of Physical Chemistry* **1990,** *94* (14), 5483.
185. Pierloot, K.; Dumez, B.; Widmark, P.-O.; Roos, B. O., Density matrix averaged atomic natural orbital (ANO) basis sets for correlated molecular wave functions. *Theor. Chim. Acta* **1995,** *90* (2), 87.
186. Barandiarán, Z.; Seijo, L., The abinitio model potential method. Cowan–Griffin relativistic core potentials and valence basis sets from Li (Z = 3) to La (Z = 57). *Can. J. Chem.* **1992,** *70* (2), 409.
187. Roos, B. O.; Malmqvist, P.-Å., Relativistic quantum chemistry: the multiconfigurational approach. *Phys. Chem. Chem. Phys.* **2004,** *6* (11), 2919.
188. Roos, B. O.; Lindh, R.; Malmqvist, P.-Å.; Veryazov, V.; Widmark, P.-O., Main Group Atoms and Dimers Studied with a New Relativistic ANO Basis Set. *The Journal of Physical Chemistry A* **2004,** *108* (15), 2851.
189. Quinn, M. S. The Photodissociation of Small Aldehydes: A Refined Understanding of Prototypical Dynamical Systems. University of New South Wales, 2016.
190. Frisch, M. J.; Trucks, G. W.; Schlegel, H. B.; Scuseria, G. E.; Robb, M. A.; Cheeseman, J. R.; Scalmani, G.; Barone, V.; Petersson, G. A.; Nakatsuji, H.; Li, X.; Caricato, M.; Marenich, A. V.; Bloino, J.; Janesko, B. G.; Gomperts, R.; Mennucci, B.; Hratchian, H. P.; Ortiz, J. V.; Izmaylov, A. F.; Sonnenberg, J. L.; Williams; Ding, F.; Lipparini, F.; Egidi, F.; Goings, J.; Peng, B.; Petrone, A.; Henderson, T.; Ranasinghe, D.; Zakrzewski, V. G.; Gao, J.; Rega, N.; Zheng, G.; Liang, W.; Hada, M.; Ehara, M.; Toyota, K.; Fukuda, R.; Hasegawa, J.; Ishida, M.; Nakajima, T.; Honda, Y.; Kitao, O.; Nakai, H.; Vreven, T.; Throssell, K.; Montgomery Jr., J. A.; Peralta, J. E.; Ogliaro, F.; Bearpark, M. J.; Heyd, J. J.; Brothers, E. N.; Kudin, K. N.; Staroverov, V. N.; Keith, T. A.; Kobayashi, R.; Normand, J.; Raghavachari, K.; Rendell, A. P.; Burant, J. C.; Iyengar, S. S.; Tomasi, J.; Cossi, M.; Millam, J. M.; Klene, M.; Adamo, C.; Cammi, R.; Ochterski, J. W.; Martin, R. L.; Morokuma, K.; Farkas, O.; Foresman, J. B.; Fox, D. J. *Gaussian 09 Rev. D.01*, Wallingford, CT, 2016.
191. Yanai, T.; Tew, D. P.; Handy, N. C., A new hybrid exchange–correlation functional using the Coulomb-attenuating method (CAM-B3LYP). *Chem. Phys. Lett.* **2004,** *393* (1), 51.
192. Chai, J.-D.; Head-Gordon, M., Long-range corrected hybrid density functionals with damped atom–atom dispersion corrections. *Phys. Chem. Chem. Phys.* **2008,** *10* (44), 6615.
193. Kendall, R. A.; Dunning, T. H.; Harrison, R. J., Electron affinities of the first-row atoms revisited. Systematic basis sets and wave functions. *The Journal of Chemical Physics* **1992,** *96* (9), 6796.

194. Wilson, R. J.; Mueller, J. A.; Houston, P. L., Speed-Dependent Anisotropy Parameters in the UV Photodissociation of Ozone. *The Journal of Physical Chemistry A* **1997,** *101* (41), 7593.
195. He, C.; Yin, R.; Hu, G.; Zhou, X.; Chen, Y.; Zhao, D.; Jiang, B., Combined experimental and theoretical study on the ultraviolet photodissociation dynamics of 1-bromo-2,6-difluorobenzene in 267 nm–234 nm. *The Journal of Chemical Physics* **2020,** *153* (3), 034305.
196. Roueff, E.; Lique, F., Molecular excitation in the interstellar medium: recent advances in collisional, radiative, and chemical processes. *Chem Rev* **2013,** *113* (12), 8906.
197. Schiffman, A.; Chandler, D. W., Experimental Measurements of State-Resolved, Rotationally Inelastic Energy-Transfer. *Int. Rev. Phys. Chem.* **1995,** *14*, 371.
198. Dagdigian, P. J., Theoretical Investigation of Collisional Energy Transfer in Polyatomic Intermediates. *Int. Rev. Phys. Chem.* **2013,** *32*, 229.
199. Wade, E. A.; Thomas Lorenz, K.; Chandler, D. W.; Barr, J. W.; Barnes, G. L.; Cline, J. I., Ion Imaging Studies of Product Rotational Alignment in Collisions of NO with Ar. *Chem. Phys.* **2004,** *301*, 261.
200. Kohguchi, H.; Suzuki, T.; Alexander, M. H., Fully State-Resolved Differential Cross Sections for the Inelastic Scattering of the Open-Shell NO Molecule by Ar. *Science* **2001,** *294*, 832.
201. Lorenz, K. T.; Chandler, D. W.; Barr, J. W.; Chen, W.; Barnes, G. L.; Cline, J. I., Direct Measurement of the Preferred Sense of NO Rotation after Collision with Argon. *Science* **2001,** *293*, 2063.
202. Sarma, G.; Marinakis, S.; ter Meulen, J. J.; Parker, D. H.; McKendrick, K. G., Inelastic scattering of hydroxyl radicals with helium and argon by velocity-map imaging. *Nat Chem* **2012,** *4* (12), 985.
203. Chadwick, H.; Nichols, B.; Gordon, S. D.; Hornung, B.; Squires, E.; Brouard, M.; Klos, J.; Alexander, M. H.; Aoiz, F. J.; Stolte, S., Inelastic Scattering of NO by Kr: Rotational Polarization over a Rainbow. *J. Phys. Chem. Lett.* **2014,** *5*, 3296.
204. Vogels, S. N.; Onvlee, J.; Chefdeville, S.; van der Avoird, A.; Groenenboom, G. C.; van de Meerakker, S. Y., Imaging resonances in low-energy NO-He inelastic collisions. *Science* **2015,** *350* (6262), 787.
205. Tkac, O.; Ma, Q.; Stei, M.; Orr-Ewing, A. J.; Dagdigian, P. J., Rotationally inelastic scattering of methyl radicals with Ar and N_2. *J. Chem. Phys.* **2015,** *142* (1), 014306.
206. Tkáč, O.; Saha, A. K.; Loreau, J.; Ma, Q.; Dagdigian, P. J.; Parker, D. H.; van der Avoird, A.; Orr-Ewing, A. J., Rotationally Inelastic Scattering of ND_3 with H_2 as a Probe of the Intermolecular Potential Energy Surface. *Mol. Phys.* **2015,** *113*, 3925.
207. Gao, Z.; Loreau, J.; van der Avoird, A.; van de Meerakker, S. Y. T., Direct observation of product-pair correlations in rotationally inelastic collisions of ND_3 with D_2. *Phys. Chem. Chem. Phys.* **2019,** *21* (26), 14033.
208. Vogels, S. N.; Karman, T.; Klos, J.; Besemer, M.; Onvlee, J.; van der Avoird, A.; Groenenboom, G. C.; van de Meerakker, S. Y. T., Scattering Resonances in Bimolecular Collisions Between NO Radicals and H_2 Challenge the Theoretical Gold Standard. *Nat. Chem.* **2018,** *10*, 435.
209. Gao, Z.; Vogels, S. N.; Besemer, M.; Karman, T.; Groenenboom, G. C.; van der Avoird, A.; van de Meerakker, S. Y. T., State-to-State Differential Cross Sections for Inelastic Collisions of NO Radicals with para-H_2 and ortho-D_2. *J. Phys. Chem. A* **2017,** *121*, 7446.
210. de Jongh, T.; Karman, T.; Vogels, S. N.; Besemer, M.; Onvlee, J.; Suits, A. G.; Thompson, J. O. F.; Groenenboom, G. C.; van der Avoird, A.; van de Meerakker, S. Y. T., Imaging Diffraction Oscillations for Inelastic Collisions of NO Radicals with He and D_2. *J. Chem. Phys.* **2017,** *147*, 013918.
211. Gao, Z.; Karman, T.; Vogels, S. N.; Besemer, M.; van der Avoird, A.; Groenenboom, G. C.; van de Meerakker, S. Y. T., Observation of correlated excitations in bimolecular collisions. *Nat Chem* **2018,** *10* (4), 469.
212. Gao, Z.; Karman, T.; Tang, G.; van der Avoird, A.; Groenenboom, G. C.; van de Meerakker, S. Y. T., Correlated Energy Transfer in Rotationally and Spin-Orbit Inelastic Collisions of NO($X^2\Pi_{1/2}$, j = 1/2f) with O2($X^3\Sigma_g^-$). *Phys. Chem. Chem. Phys.* **2018,** *20*, 12444.

213. Karman, T.; Besemer, M.; van der Avoird, A.; Groenenboom, G. C., Diabatic States, Nonadiabatic Coupling, and the Counterpoise Procedure for Weakly Interacting Open-Shell Molecules. *J. Chem. Phys.* **2018,** *148*, 094105.
214. Buck, U.; Huisken, F.; Schleusener, J.; Schaefer, J., State Resolved Rotational Excitation in HD+D_2 Collisions. I. Angular Dependence of 0→1 Transitions. *J. Chem. Phys.* **1981,** *74*, 535.
215. Buck, U.; Huisken, F.; Schleusener, J., Diffraction Oscillations in Rotationally Inelastic Differential Cross-Sections - HD+D_2. *J. Chem. Phys.* **1978,** *68*, 5654.
216. Bacon, J. A.; Giese, C. F.; Gentry, W. R., State-to-State Differential Cross Sections for Rotationally Inelastic Collisions of NO($^2\Pi_{1/2}$, j⩽2.5) with CO($^1\Sigma^+$) and O_2($^3\Sigma_g^-$) at a kinetic energy of 442 cm^{-1}. *J. Chem. Phys.* **1998,** *108*, 3127.
217. Vonk, M. T.; Bacon, J. A.; Giese, C. F.; Gentry, W. R., Differential Cross Sections for Rotationally Inelastic Collisions of NO($^2\Pi_{1/2}$, j'⩽2.5) with NO($^2\Pi_{1/2}$, j'⩽2.5) at a kinetic energy of 442 cm^{-1}. *J. Chem. Phys.* **1997,** *106*, 1353.
218. Wade, E. A.; Lorenz, K. T.; Springfield, J. L.; Chandler, D. W., Collisions of HCl with Rare Gas and Molecular Colliders. *J. Phys. Chem. A* **2003,** *107*, 4976.
219. Tkac, O.; Orr-Ewing, A. J.; Dagdigian, P. J.; Alexander, M. H.; Onvlee, J.; van der Avoird, A., Collision dynamics of symmetric top molecules: a comparison of the rotationally inelastic scattering of CD_3 and ND_3 with He. *J. Chem. Phys.* **2014,** *140* (13), 134308.
220. Tkáč, O.; Sage, A. G.; Greaves, S. J.; Orr-Ewing, A. J.; Dagdigian, P. J.; Ma, Q. L.; Alexander, M. H., Rotationally Inelastic Scattering of CD_3 and CH_3 with He: Comparison of Velocity Map-Imaging Data with Quantum Scattering Calculations. *Chem Sci* **2013,** *4*, 4199.
221. Schepper, W.; Ross, U.; Beck, D., Anisotropy of the Repulsive Intermolecular Potential from Rotationally Inelastic Scattering. *Z. Phys. A: At. Nucl.* **1979,** *290*, 131.
222. Sarma, G.; Saha, A. K.; Bishwakarma, C. K.; Scheidsbach, R.; Yang, C. H.; Parker, D.; Wiesenfeld, L.; Buck, U.; Mavridis, L.; Marinakis, S., Collision energy dependence of state-to-state differential cross sections for rotationally inelastic scattering of H_2O by He. *Phys. Chem. Chem. Phys.* **2017,** *19* (6), 4678.
223. Levine, R. D.; Bernstein, R. B., *Molecular Reaction Dynamics and Chemical Reactivity*. 1987.
224. Yang, M.; Watts, R. O., The Anisotropic Potential Energy Surfaces of H_2, N_2, and Ar with C_2H_2 from Total Differential Scattering Experiments. *J. Chem. Phys.* **1994,** *100*, 3582.
225. Pan, H.; Liu, K., Observation of a Reactive Rainbow in F + CH_3D --> CH_2D(v = 0) + HF(v = 3)? *J. Phys. Chem. A* **2016,** *120* (34), 6712.
226. Bowman, J. M., Rotational Rainbows in Inelastic Atom-Molecule Differential Cross-Sections. *Chem. Phys. Lett.* **1979,** *62*, 309.
227. Schinke, R.; Korsch, H. J.; Poppe, D., Rainbows in rotationally inelastic scattering: A comparative study of different model potential surfaces and dynamical approximations. *J. Chem. Phys.* **1982,** *77* (12), 6005.
228. Aoiz, F. J.; Verdasco, J. E.; Brouard, M.; Klos, J.; Marinakis, S.; Stolte, S., Inelastic Scattering of He atoms and NO($X^2\Pi$) molecules: the Role of Parity on the Differential Cross Section. *J. Phys. Chem. A* **2009,** *113*, 14636.
229. Gijsbertsen, A.; Linnartz, H.; Stolte, S., Parity-dependent rotational rainbows in D_2-NO and He-NO differential collision cross sections. *J. Chem. Phys.* **2006,** *125* (13), 133112.
230. Klos, J.; Aoiz, F. J.; Menendez, M.; Brouard, M.; Chadwick, H.; Eyles, C. J., Ab initio studies of the interaction potential for the Xe-NO($X^2\Pi$) van der Waals complex: bound states and fully quantum and quasi-classical scattering. *J. Chem. Phys.* **2012,** *137* (1), 014312.
231. Western, C. M., PGOPHER: A program for simulating rotational, vibrational and electronic spectra. *J. Quant. Spectrosc. Radiat. Transfer* **2017,** *186*, 221.
232. Thompson, J. O. F.; Amarasinghe, C.; Foley, C. D.; Suits, A. G., Finite slice analysis (FINA)-A general reconstruction method for velocity mapped and time-sliced ion imaging. *J. Chem. Phys.* **2017,** *147* (1), 013913.

233. Buck, U.; Kohlhase, A.; Secrest, D.; Phillips, T.; Scoles, G.; Grein, F., Rotationally Inelastic-Scattering and Potential Calculations for Ne + CH_4. *Mol. Phys.* **1985,** *55*, 1233.
234. Wang, F. Y.; Liu, K. P., Imaging the Effects of Bend-Excitation in the F + $CD_4(v_b=0,1) \rightarrow DF(v) + CD_3(v_2=1,2)$ Reactions. *J. Phys. Chem. A* **2013,** *117*, 8536.
235. Shimanouchi, T., *Tables of Molecular Vibrational Frequencies Consolidated Volume I*. National Bureau of Standards: 1972.
236. Huber, K. P.; Herzberg, G. H., Constants of Diatomic Molecules. In *NIST Chemistry WebBook, NIST Standard Reference Database Number 69*, Linstrom, P. J.; Mallard, W. G., Eds. National Institute of Standards and Technology.
237. Yonekura, N.; Gebauer, C.; Kohguchi, H.; Suzuki, T., A crossed molecular beam apparatus using high-resolution ion imaging. *Rev. Sci. Instrum.* **1999,** *70* (8), 3265.
238. Komissarov, A. V.; Minitti, M. P.; Suits, A. G.; Hall, G. E., Correlated product distributions from ketene dissociation measured by dc sliced ion imaging. *J. Chem. Phys.* **2006,** *124* (1), 14303.
239. Brouard, M.; Chadwick, H.; Eyles, C. J.; Hornung, B.; Nichols, B.; Scott, J. M.; Aoiz, F. J.; Klos, J.; Stolte, S.; Zhang, X., the Fully Quantum State-Resolved Inelastic Scattering of NO(X) plus Ne: Experiment and Theory. *Mol. Phys.* **2013,** *111*, 1759.
240. Westley, M. S.; Lorenz, K. T.; Chandler, D. W.; Houston, P. L., Differential Cross Sections for Rotationally Inelastic Scattering of NO from He and D_2. *J. Chem. Phys.* **2001,** *114*, 2669.
241. Bosanac, S., Two-dimensional model of rotationally inelastic collisions. *Phys. Rev. A* **1980,** *22* (6), 2617-2622.
242. Crespo-Otero, R.; Suardiaz, R.; Montero, L. A.; de la Vega, J. M., Potential energy surfaces and Jahn-Teller effect on CH_4...NO complexes. *J. Chem. Phys.* **2007,** *127* (10), 104305.
243. Herzberg, G., *Electronic Spectra and Electronic Structure of Polyatomic Molecules*. 1966; Vol. 3.
244. Fukuzawa, K.; Osamura, Y.; Schaefer Iii, H. F., Are Neutral-Neutral Reactions Effective for the Carbon-Chain Growth of Cyanopolyynes and Polyacetylenes in Interstellar Space? *The Astrophysical Journal* **1998,** *505* (1), 278.
245. Baulch, D. L.; Duxbury, J.; Grant, S. J.; Montague, D. C., Evaluated Kinetic Data For High Temperature Reactions; Volume 4, Homogeneous Gas Phase Reactions Of Halogen And Cyanide Containing Species. *J. Phys. Chem. Ref. Data, Suppl.* **1981,** *10*, 721.
246. Balla, R. J.; Casleton, K. H.; Adams, J. S.; Pasternack, L., Absolute rate constants for the reaction of cyanogen with methane, ethane, and propane from 292 to 1500 K using high-temperature photochemistry and diode laser absorption. *J. Phys. Chem.* **1991,** *95* (22), 8694.
247. Atakan, B.; Wolfrum, J., Kinetic studies of the reactions of CN radicals with alkanes in the temperature range between 294 and 1260 K. *Chemical Physics Letters* **1991,** *186* (6), 547.
248. Huang, C.; Li, W.; Estillore, A. D.; Suits, A. G., Dynamics of CN+alkane reactions by crossed-beam dc slice imaging. *The Journal of Chemical Physics* **2008,** *129* (7), 074301.
249. Preston, T. J.; Hornung, B.; Pandit, S.; Harvey, J. N.; Orr-Ewing, A. J., Dynamical Effects and Product Distributions in Simulated CN + Methane Reactions. *J. Phys. Chem. A* **2016,** *120* (27), 4672.
250. Sun, Q.; Yang, D. L.; Wang, N. S.; Bowman, J. M.; Lin, M. C., Experimental and reduced dimensionality quantum rate coefficients for $H_2(D_2)$+CN→H(D)CN+H(D). *The Journal of Chemical Physics* **1990,** *93* (7), 4730.
251. Sims, I. R.; Smith, I. W. M., Rate constants for the reactions CN(v=0), CN(v=1)+H_2, D_2→HCN, DCN+H, D between 295 and 768 K, and comparisons with transition state theory calculations. *Chem. Phys. Lett.* **1988,** *149* (5), 565.
252. Szekely, A.; Hanson, R. K.; Bowman, C. T., High-temperature determination of the rate coefficient for the reaction H_2 + CN → H + HCN. *Int. J. Chem. Kinet.* **1983,** *15* (9), 915.
253. Copeland, L. R.; Mohammad, F.; Zahedi, M.; Volman, D. H.; Jackson, W. M., Rate constants for CN reactions with hydrocarbons and the product HCN vibrational populations: Examples of heavy–light–heavy abstraction reactions. *The Journal of Chemical Physics* **1992,** *96* (8), 5817.

254. Sims, I. R.; Queffelec, J.-L.; Travers, D.; Rowe, B. R.; Herbert, L. B.; Karthäuser, J.; Smith, I. W. M., Rate constants for the reactions of CN with hydrocarbons at low and ultra-low temperatures. *Chem. Phys. Lett.* **1993,** *211* (4), 461.
255. Sayah, N.; Li, X.; Caballero, J. F.; Jackson, W. M., Laser induced fluorescence studies of CN reactions with alkanes, alkenes and substituted aliphatic species. *J. Photochem. Photobiol. A: Chem.* **1988,** *45* (2), 177.
256. Pan, H.; Liu, K., Imaging spectroscopy of the missing REMPI bands of methyl radicals: Final touches on all vibrational frequencies of the 3p Rydberg states. *The Journal of Chemical Physics* **2018,** *148* (1), 014303.
257. Bethardy, G. A.; Northrup, F. J.; Macdonald, R. G., The initial vibrational level distribution and relaxation of HCN[$\tilde{X}^1\Sigma^+$ (v_1,0,v_3)] in the CN($X^2\Sigma^+$)+CH_4 →HCN+CH_3 reaction system. *The Journal of Chemical Physics* **1996,** *105* (11), 4533.
258. Yang, D. L.; Yu, T.; Wang, N. S.; Lin, M. C., Temperature dependence of cyanogen radical reactions with selected alkanes: CN reactivities towards primary, secondary and tertiary C・H bonds. *Chem. Phys.* **1992,** *160* (2), 307.
259. Lane, P. D.; Moncrieff, K. E.; Greaves, S. J.; McKendrick, K. G.; Costen, M. L., Inelastic Scattering of CN Radicals at the Gas–Liquid Interface Probed by Frequency-Modulated Absorption Spectroscopy. *The Journal of Physical Chemistry C* **2020,** *124* (30), 16439.
260. Atmosphériques, L. I. d. S. Mid-UV Absorption Coefficients. http://losno.lisa.univ-paris-diderot.fr/services/DiffuseUVdata/
261. Keller-Rudek, H. M., G. K.; Sander, R.; Sörensen, R., The MPI-Mainz UV/VIS Spectral Atlas of Gaseous Molecules of Atmospheric Interest *Earth System Science Data* **2013,** *5*, 365.
262. Wu, M.; Hall, G. E., Vector and scalar correlations in the photodissociation of NCCN. *J. Photochem. Photobiol. A: Chem.* **1994,** *80* (1), 45.
263. Huang, Y.; Barts, S. A.; Halpern, J. B., Heat of formation of the cyanogen radical. *The Journal of Physical Chemistry* **1992,** *96* (1), 425.
264. Halpern, J. B.; Jackson, W. M., Energy partitioning in the dissociation of cyanogen at 193 nm. *The Journal of Physical Chemistry* **1982,** *86* (6), 973.
265. Felps, W. S.; Rupnik, K.; McGlynn, S. P., Electronic spectroscopy of the cyanogen halides. *J. Phys. Chem.* **1991,** *95* (2), 639.
266. Halpern, J. B.; Jackson, W. M., Partitioning of excess energy in the photolysis of cyanogen chloride and cyanogen bromide at 193 nm. *The Journal of Physical Chemistry* **1982,** *86* (18), 3528.
267. Nadler, I.; Reisler, H.; Wittig, C., Energy disposal in the laser photodissociation of ICN and BrCN at 300 K and in a free jet expansion. *Chem. Phys. Lett.* **1984,** *103* (6), 451.
268. Russell, J. A.; McLaren, I. A.; Jackson, W. M.; Halpern, J. B., Photolysis of cyanogen bromide between 193 and 266 nm. *The Journal of Physical Chemistry* **1987,** *91* (12), 3248.
269. Morse, M. D.; Freed, K. F.; Band, Y. B., Rotational distributions from photodissociation. II. Results for ICN+hν→I+CN($X\ ^2\Sigma^+$). *The Journal of Chemical Physics* **1979,** *70* (8), 3620.
270. Hess, W. P.; Leone, S. R., Absolute I* quantum yields for the ICN Ã state by diode laser gain-vs-absorption spectroscopy. *The Journal of Chemical Physics* **1987,** *86* (7), 3773.
271. Lambert, M.; Callen, B.; Dugan, H.; Filseth, S. V.; Morgan, F. J.; Sadowski, C. M., ICN photodissociation at 193 nm; CN($B^2\Sigma$) rotational distributions and fluorescence polarization. *Chem. Phys. Lett.* **1987,** *139* (1), 45.
272. Stull, D. R., Vapor Pressure of Pure Substances. Organic and Inorganic Compounds. *Industrial & Engineering Chemistry* **1947,** *39* (4), 517.
273. Lord, G.; Woolf, A. A., The cyanogen halides. Part III. Their heats of formation and free energies. *Journal of the Chemical Society (Resumed)* **1954,** (0), 2546.
274. Felps, S.; Hochmann, P.; Brint, P.; McGlynn, S. P., Molecular Rydberg transitions: The lowest-energy Rydberg transitions of s-type in CH_3X and CD_3X, X = Cl, Br, and I. *Journal of Molecular Spectroscopy* **1976,** *59* (3), 355.

275. Gilchrist, A.; Hancock, G.; Peverall, R.; Richmond, G.; Ritchie, G. A. D.; Taylor, S., Methyl Iodide Photodissociation at 193 nm: The I($^2P_{1/2}$) Quantum Yield. *The Journal of Physical Chemistry A* **2008,** *112* (20), 4531.
276. Poullain, S. M.; Chicharro, D. V.; Rubio-Lago, L.; García-Vela, A.; Bañares, L., A velocity-map imaging study of methyl non-resonant multiphoton ionization from the photodissociation of CH_3I in the A-band. *Philosophical Transactions of the Royal Society A: Mathematical, Physical and Engineering Sciences* **2017,** *375* (2092), 20160205.
277. Marggi Poullain, S.; Chicharro, D. V.; González-Vázquez, J.; Rubio-Lago, L.; Bañares, L., A velocity map imaging study of the photodissociation of the methyl iodide cation. *Phys. Chem. Chem. Phys.* **2017,** *19* (11), 7886.
278. Cascarini, F. J. J.; Hornung, B.; Quinn, M. S.; Robertson, P. A.; Orr-Ewing, A. J., Collision Energy Dependence of the Competing Mechanisms of Reaction of Chlorine Atoms with Propene. *The Journal of Physical Chemistry A* **2019,** *123* (13), 2679.
279. Li, H.; Suits, A. G., Universal crossed beam imaging studies of polyatomic reaction dynamics. *Phys. Chem. Chem. Phys.* **2020,** *22* (20), 11126.
280. Borg, O. A.; Liu, Y. J.; Persson, P.; Lunell, S.; Karlsson, D.; Kadi, M.; Davidsson, J., Photochemistry of bromofluorobenzenes. *J. Phys. Chem. A* **2006,** *110* (22), 7045.
281. Heid, C. G.; Walpole, V.; Brouard, M.; Jambrina, P. G.; Aoiz, F. J., Side-impact collisions of Ar with NO. *Nature Chemistry* **2019,** *11* (7), 662.